Electron transfer reactivity patterns at chemically modified electrodes: fundamentals and application to the optimization of redox recycling amplification systems

by

Adam Johan Bergren

A dissertation submitted to the graduate faculty

in partial fulfillment of the requirements for the degree of

DOCTOR OF PHILOSOPHY

Major: Analytical Chemistry

Program of Study Committee:
Marc D. Porter, Major Professor
Robert S. Houk
Patricia A. Thiel
L. Keith Woo
Balaji Narasimhan

Iowa State University

Ames, Iowa

2006

ProQuest Information and Learning Company
300 North Zeeb Road
P.O. Box 1346
Ann Arbor, MI 48106-1346

Graduate College
Iowa State University

This is to certify that the doctoral dissertation of

Adam Johan Bergren

has met the dissertation requirements of Iowa State University

Signature was redacted for privacy.

Major Professor

Signature was redacted for privacy.

For the Major Program

DEDICATIONS AND ACKNOWLEDGEMENTS

This dissertation is dedicated to my wife, Suzanne.

I would like to thank and acknowledge many of the people that have made my years at Iowa State productive and enjoyable. First, I would like to acknowledge the support and freedom offered by my major professor, Marc Porter. I would also like to acknowledge members of our research group throughout the years for constructive criticism, encouraging words, helpful conversations and arguments (mostly peaceful), and friendship; especially Grant Edwards, Jeremy Driskell, Dan Gazda, Erik Cox, Robert J. Lipert, Karen Kwarta, Brent Dawson, Deepak Dibya, Lisa Ponton, April Hazen, David Keller, Mike Granger, Jennifer Harnisch-Granger, and Becky Staedtler. I would also like to thank the following collaborators and friends for helpful discussions, assistance with experiments, and the opportunity to learn about a variety of exciting topics and techniques in chemistry: Mike Vasbinder, James Espenson, Shirsudersan Jayaraman, Andrew C. Hillier, Henry S. White, Jeremy Galusha, Brendan Boyd, and Brian King. Finally, I would like to acknowledge the support and encouragement of my family.

I gratefully acknowledge the support of Eastman Chemical Company and a Proctor and Gamble graduate fellowship.

This work was performed at Ames Laboratory under Contract No. W-74050-Eng-82 with the U.S. Department of Energy. The United States government has assigned the DOE Report number IS-T 2223 to this dissertation.

TABLE OF CONTENTS

ABSTRACT

Electroanalytical chemistry is often utilized in chemical analysis and fundamental studies. Important advances have been made in these areas since the advent of chemically modified electrodes: the coating of an electrode with a chemical film in order to impart desirable, and ideally, predictable properties. These procedures enable the exploitation of unique reactivity patterns. This dissertation presents studies that investigate novel reaction mechanisms at self-assembled monolayers on gold. In particular, a unique electrochemical current amplification scheme is detailed that relies on a selective electrode to enable a reactivity pattern that results in regeneration of the analyte (redox recycling). This regenerating reaction can occur up to 250 times for each analyte molecule, leading to a notable enhancement in the observed current. The requirements of electrode selectivity and the resulting amplification and detection limit improvements are described with respect to the heterogeneous and homogeneous electron transfer rates that characterize the system. These studies revealed that the heterogeneous electrolysis of the analyte should ideally be electrochemically reversible, while that that for the regenerating agent should be held to a low level. Moreover, the homogeneous reaction that recycles the analyte should occur at a rapid rate. The physical selectivity mechanism is also detailed with respect to the properties of the electrode and redox probes utilized. It is shown that partitioning of the analyte into/onto the adlayer leads to the extraordinary selectivity of the alkanethiolate monolayer modified electrode. Collectively, these studies enable a thorough understanding of the complex electrode mechanism required for successful redox recycling amplification systems. Finally, in a separate (but related) study, the effect of the alkyl chain length on the heterogeneous electron transfer behavior of solution-based redox probes is reported, where an odd-even oscillation (with respect to the number of methylene units in the alkyl chain) was observed. Characterization of the adlayers by infrared reflection spectroscopy, ellipsometry, and wetting revealed odd-even effects in the orientation of the terminal methyl group and hydrophobic character of the adlayers. Using these structural characterizations as a basis, several possible mechanisms that can account for the odd-even effect in the heterogeneous electron transfer rates of solution-based redox couples are discussed.

CHAPTER 1. GENERAL INTRODUCTION

Dissertation Organization

This dissertation is divided into six chapters. First, included in the general introduction is a review of relevant literature for electrochemical sensor design and self-assembled monolayers. This section also incorporates an overview of the important techniques and concepts central to the studies herein. Following the general introduction are four chapters composed of papers that have been published or are intended to be submitted for publication. The first three papers concentrate on the design and performance of electrochemical sensors which utilize catalytic homogeneous electron transfer amplification (redox recycling). These studies are directly related; however, they are intended to stand alone, with each building on the findings of the previous works in a way that leads to a comprehensive system description and optimization strategies. The fourth and final paper reports on electron transfer mechanisms at alkanethiolates on gold as a function of chain length. This study is focused on the fundamental relationship between the structure of the insulating barrier and its electron transfer behavior. Finally, the last chapter contains general conclusions and future prospects. Literature citations are collected at the end of each chapter.

1. General Overview

Electron transfer is fundamental to many important chemical, physical, and biological processes. For example, these reactions can serve as a sensitive transduction mechanism for chemical analysis or in the characterization of a chemical system. Thus, studies of electron transfer can lead to advances in analytical techniques and provide many critical insights into a host of fundamental processes. In particular, the burgeoning areas of nanotechnology, biotechnology and molecular electronics all rely, in part, on applied and theoretical electroanalytical chemistry for continued progress.

A major breakthrough in the application of electrochemistry to analytical and fundamental problems was the development of controlled chemical modification procedures. The early foundations of chemically modified electrodes (CMEs) were established in the mid-1970s [1-3]. Since these seminal works, a vast array of research focused on the modification of electrode surfaces has been reported [4-11]. Today, CMEs are ubiquitous in electrochemistry and in other areas where such designed features are valuable (e.g., analytical and surface chemistries). The primary reason for such widespread interest in CMEs arises, for example, from increased selectivity, sensitivity, stability, larger usable potential windows, and improved resistance to fouling.

Adapting the IUPAC definition, a chemically modified electrode is a conducting or semi-conducting material that has been coated with a monomolecular, multi-molecular, ionic, or polymeric film (often referred to as the adlayer) which alters the electrochemical, optical, and other properties of the interface [12, 13]. The conductive and semi-conductive substrates are derived from conventional electrode materials, while the adlayers are widely diverse in their origins and properties. This diversity extends the range and scope of electrochemical techniques, and provides a basis for the more widespread application of designed interfaces.

This dissertation investigates the application of CMEs in a redox recycling scheme to enhance the detection capabilities of electroanalytical sensors [14-21]. Current amplification is achieved using a selective electrode that enables a reactivity pattern that recycles an analyte multiple times with respect to heterogeneous electron transfer. However, the resulting improvement in the detection limit is a complex function that is dependent on the heterogeneous and homogeneous electron transfer rates, the adlayer structure, and the characteristics of the redox molecules used. Chapters 2-4 detail performance aspects of a model system, recently introduced by Creager and co-workers [18-20], based on derivatized ferrocenes as an analyte and ferrocyanide as a sacrificial electron donor.

This dissertation also presents studies of structural effects in heterogeneous electron transfer across saturated bridges [22, 23], which yield a range of novel findings in the relationship between the structure and interfacial properties of alkanethiolate monolayers on gold. For example, the first evidence for an odd-even oscillation in the heterogeneous electron transfer rate constant of solution-based redox couples (with respect to the alkyl chain length) is reported, and its underlying causes investigated.

Taken together, the work in this dissertation describes electron transfer reactivity patterns at self-assembled monolayers on gold. The fundamental nature of these studies ultimately enables the optimized application of redox recycling, including the discovery of new and improved systems. Moreover, structure-function relationships in heterogeneous electron transfer are investigated at a detailed level. An overview of the techniques and topics that are critical to the work in this dissertation follows.

2. Electrochemical Signal Amplification

2.1. Current Measurements

Of the many possibilities, electroanalytical current measurements are particularly powerful for analytical sensor design and in the evaluation of physicochemical properties. Analytically, current-based readout produces a linear response over a large dynamic range [24]. This advantage is best summarized by Faraday's law, which states that the electricity produced (or consumed) at an electrode is directly proportional to the quantity of substance involved in the electrolytic reaction [4]. Thus, electrochemical current transduction techniques are easily applied to quantitation of redox-active analytes. The large value of the Faraday (96,485 Coulombs per equivalent*) serves to illustrate the high inherent sensitivity of electroanalytical current measurements.

Faraday's law defines the maximum current that can result from a heterogeneous electron transfer reaction. However, many factors dictate whether this limit can be realized experimentally. For example, the reaction kinetics must be rapid such that each analyte molecule that encounters the electrode undergoes electron exchange. Even in favorable cases (i.e., for diffusion-limited kinetics), the detection limit is determined by the smallest current that can be definitively attributed to the target analyte. If the quantity of material to be determined results in a current that is too small to satisfy the signal to background requirements, it cannot be sensed using a simple heterogeneous reaction.

The background in an electroanalytical current measurement is normally dominated by double layer charging current. Charging current arises from the re-organizational processes that accompany changes in electrode potential. Thus, improvements in sensitivity have been accomplished by using specialized potential programs combined with specific current sampling intervals [4]. The suite of pulse voltammetries all utilize the fact that after potential stabilization, charging current decays much more rapidly than Faradaic current. For example, differential pulse, normal pulse, and square-wave voltammetry all employ different potential perturbations and current sampling techniques in a quest to reduce the relative contribution of the double layer charging current to the overall measured current. Although pulse techniques

---

* An equivalent is the number of electrons resulting from reaction of one mole of a substance that exchanges one electron per molecule with the electrode

can lead to marked improvements in sensitivity and detection limits, they are still fundamentally limited by Faraday's law.

Collectively, these issues illustrate that a general strategy to overcome the Faraday limit is highly desirable in electroanalytical sensor design.

2.2. Redox Recycling Current Amplification

How then, to overcome such a fundamental limit as Faraday's law? Although preconcentration [25] is applied in some cases, not all analytes can be collected onto an electrode. Furthermore, signal processing techniques have long made the background in a current measurement far more important than environmental noise, even when nanoelectrodes are employed (resulting in pico- or femto-ampere current levels) [4]. Thus, recent research has focused on the use of modified electrodes to enable homogeneous redox recycling mechanisms to greatly amplify the current signal, while only producing moderate increases in background current [16-20].

Redox recycling amplification utilizes a sacrificial source (or equivalently, a sink) of electrons to effectively multiply the number of electron transfer events for each analyte through a catalytic reaction mechanism. The appropriate form of a redox molecule is added to the sample solution such that upon a heterogeneous electron transfer event involving the target, an instantaneous homogeneous reaction results in which the original form of the analyte is a product. This regenerating process occurs at a cost of the added sacrificial reagent. However, the cycle can be repeated until all electron sources are exhausted (i.e., the analyte and sacrificial species), resulting in a large enhancement of the experimentally observed anodic current (for an oxidation) when an excess of recycling reagent is used. Thus, low levels of a target analyte can lead to quite large measured currents. Importantly, however, the sacrificial reagent should not undergo rapid heterogeneous electrolysis.

In classical electrochemistry literature, mediation was often employed to facilitate the detection of slow-reacting analytes [26]. These schemes greatly increased the number of target molecules that could be effectively coupled to the electrode at moderate overpotentials. Moreover, bioelectrochemical reactions often occur with the assistance of a mediator (e.g., enzymatic electron transfer in respiratory processes) [5, 27]. The voltammetric response of model homogeneous redox catalysis systems were studied in some detail by Savéant [28-40]. Although redox recycling occurs through the same second-order catalytic reaction mechanism, the mediator becomes the targeted analyte in redox recycling, with the substrate acting to enhance its electrochemical signal; classical treatments of mediation and catalysis focus on analysis of the substrate. Thus, redox recycling can be envisioned as the inverse of mediation, with a new set of guidelines necessary to generalize optimal detection conditions.

Catalysis and mediation schemes, being well-established, provide a strong basis for adaptation to redox recycling. However, it is important to note that a redox couple which undergoes rapid homogeneous electron transfer (as is necessary for effective coupling between the analyte, sacrificial species, and electrode) is also likely to undergo facile heterogeneous electrolysis at an electrode [41]. Although this situation has no bearing in mediation (since the added component is intended to undergo rapid heterogeneous and homogeneous reaction), it can pose serious limitations in redox recycling. That is, the recycling reagent can potentially interfere with detection of the analyte through its own electrolysis. This complication necessitates a selective interface for redox recycling to realize any improvement in the detection limit.

An effective way to achieve selective interfacial electron transfer is to tailor the properties of an electrode surface using chemical modification. A particularly important class of modification methodology relies on the affinity of sulfur-containing molecules for the noble metals. In particular, the convenience and well-characterized behavior of self-assembled alkanethiolate monolayers on gold offer a compelling basis for the facile construction of selective electrodes [7].

The development of an advanced understanding of self-assembled alkanethiolate monolayers on gold ultimately led to the first successful application of redox recycling to improve detection limits by Stephen Creager's research group at Clemson University [18-20, 42]. These works demonstrated that the well-known reactivity pattern of iron(III)hexacyanide and ferrocene derivatives at alkanethiolate modified gold electrodes could be exploited to advance the performance of electrochemical sensors. However, many aspects of this complex system required further investigation in order to generalize the methodology and provide a foundation for extending the concept throughout electroanalytical chemistry. The importance of SAMs to the success of redox recycling warrants a review.

3. Self-Assembled Monolayers as Electrode Modifiers

Modification of a substrate surface by spontaneous adsorption [43], now more commonly referred to as self-assembly, is a highly utilized modification pathway. Self-assembled monolayers (SAMs) are thin films bound to a substrate by the spontaneous formation of a chemical bond [12]. Although the chemisorption event anchors the film, intermolecular forces within the film are important in determining the microstructure of the adlayer. These monomolecular films are often used to impart the desired function to the electrode directly, but can also serve as the foundation for more complex electrode architectures.

In electrochemical studies, SAMs offer the ability to delineate structure-function relationships. That is, the nature of the adlayer can be systematically altered (i.e., ω-functionality, chain length, and packing density) and the resulting characteristics of the electrode measured (e.g., capacitance and electron transfer rates). In this way, SAMs enable an experimenter to control the thickness of a dielectric coating on the molecular level, with the ability to alter the character of the coating in order to affect a predictable change in properties [44-47]. Many other advantages are often realized, including molecular recognition [48, 49], selectivity [16-19, 21, 50-52], and resistance to fouling [53-55].

3.1. Preparation and Structural Description

A schematic illustration of a self-assembled monolayer is shown in Figure 1. The head group chemisorbs onto the substrate and the tail is composed of a spacer chain that has terminal (or ω-) functionality. While the head group is responsible for the largest energetic contribution to self-assembly (the Au-S bond energy is 184 kJ mol^{-1} [56]), the end group

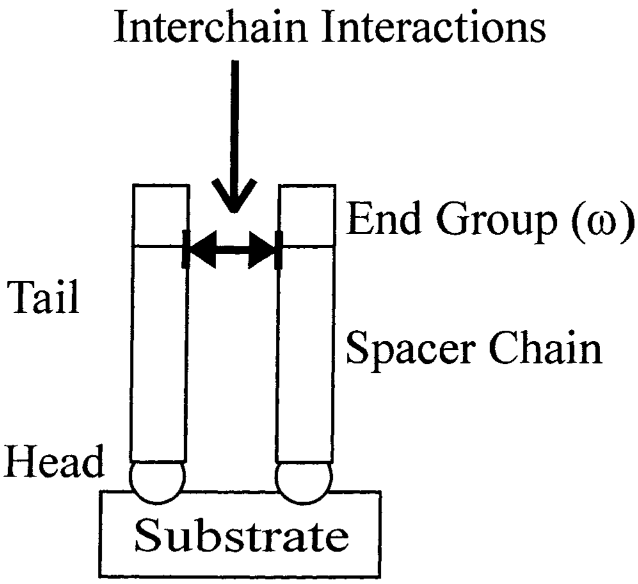

Figure 1. Schematic representation of a self-assembled monolayer.

Table 1. Common examples of modifying layers formed by chemisorption. A more extensive table is found in: J. C. Love, L. A. Estroff, J. K. Kriebel, R. G. Nuzzo, and G. M. Whitesides, Chem. Rev. 105 (2005) 1103.

Molecule	Electrode Material
RSH	Au, Ag, Pt, Cu, Hg
RSSR′	Au
RSR′	Au
R_3P	Zr
RNC	Au, Pt, Cu
RCOOH	Ag, Al_2O_3
$R(OArCH(NH_2)_2)_2$	Au
Silanes	Hydroxlyated surfaces

strongly influences the interfacial properties and the spacer chain can be important in determining film ordering (packing density). Contributions from dispersive, electrostatic, and steric interactions can all be important. Densely packed layers are formed when the entire molecule has a maximum of attractive forces and the end groups have comparable van der Waals radii. Less dense and more disordered adlayers may also form as a consequence of repulsive interactions. However, such disordered adlayers often remain suitable for a wide range of studies.

SAMs are created by exposure of a suitable substrate to adsorbate precursors in the liquid or vapor phase. Liquid solutions are most common for preparing modified electrodes. Usually, a pretreated substrate is immersed into a dilute solution (10^{-4}-10^{-3} M) for a predetermined time (seconds to days) after which the electrode is removed, rinsed copiously with neat solvent, and dried before use. Pretreatment such as mechanical and/or electrochemical polishing, chemical etches, temperature annealing, and other specialized procedures serve to provide clean and reproducible templates.

Many sulfur-containing functional groups chemisorb onto metal electrodes [7, 57-62]. For example, thiols and disulfides spontaneously adsorb on gold. Thiols also chemisorb at

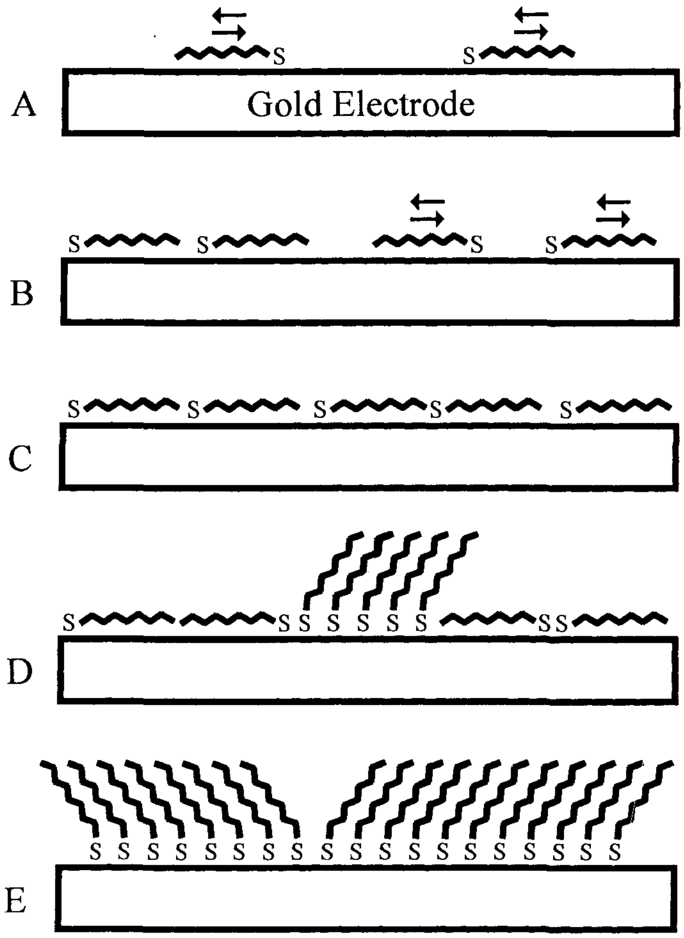

Figure 2. Illustration of the self-assembly mechanism of alkanethiols onto gold. The arrows depict mobile thiol atoms. See text for description. Adapted from: G. E. Poirier and E. D. Pylant, Science 272 (1996) 1145.

silver, copper, platinum, and mercury; however, gold is by far the most commonly used substrate electrode due to its relative inert nature. Several examples of SAMs that have been reported in the literature are listed in Table 1.

3.2. Formation and Structure of Alkanethiolates on Gold

The adsorption of alkanethiols (X-$(CH_2)_n$-SH) onto gold is an ideal system for preparing tailored electrodes. No specialized equipment is needed. Moreover, the chemical identity of the end group (X) and the length of the polymethylene spacer chain (*n*) can be easily varied to fine-tune electrode performance or for systematic studies. As a result, there are many excellent examples of the application of these systems in electroanalytical chemistry [63-65]. However, a description of the adsorption mechanism and resulting structural details of these adlayers is needed to understand and control their performance [56, 66].

The assembly mechanism of alkanethiols onto gold from the liquid [56, 66-75] and vapor phase [76] has been investigated using scanning tunneling microscopy (STM) and other techniques. A generalized mechanism is illustrated in Figure 2. The adsorption process is characterized by four distinct stages [67]. First, mobile thiol atoms at the gold surface act as a two-dimensional lattice gas (Figure 2A). Stage two is comprised of the formation of islands where mobile thiol molecules amass; molecules in these islands are still oriented parallel to the gold surface (Figure 2B). Stage three involves the reorientation of thiols in the islands (Figure 2C-D). Finally, stage four, which proceeds over a longer time scale, is driven by van der Waals interactions between the spacer chain and end groups. These lateral forces act to organize the alkyl chains and heal defects, enabling the coverage and thickness to increase to packing density limits (Figure 2E). The combination of head-group binding and intermolecular forces leads to adlayers characterized by high packing density and molecular ordering (all-trans zigzag conformation of sequences with the alkane chains), and long-term stability in the laboratory ambient.

Although SAMs are capable of forming dense adlayers, many subtle variables [77, 78] can result in important differences in the microscopic film structure. These differences can significantly alter the performance of the electrode. Electrochemical current measurements are highly sensitive to the fine structure of monomolecular films. This responsiveness is, in part, due to the exponential relationship between tunneling efficiency and the distance between electron acceptor and donor states:

$$i = i^0 e^{-\beta d} \tag{1}$$

where i is the measured current for an electron transfer across a dielectric barrier of thickness d, i^0 is the unimpeded current (i.e., $d = 0$), and β is the tunneling coefficient [4]. Double layer capacitance (C_{dl}) measurements are also sensitive to the properties of the coating:

$$C_{\mathrm{dl}} = \frac{\varepsilon\varepsilon_0}{d} \tag{2}$$

where ε is the adlayer dielectric constant, and ε_0 is the permittivity of free space [79].

SAMs are attractive electrode modifiers due to their stability over an extended potential window: –0.8 to +0.8 V vs. Ag/AgCl [79]. However, the pH of the solution can alter these limits. Nevertheless, the adlayer is oxidized at excessively anodic potentials. Furthermore, cathodic potential sweeps can induce the one-electron reductive desorption of the thiolate [80]. Integration of the peak current under this wave yields the charge for monolayer desorption and double layer restructuring; film packing density can be obtained after accounting for double layer charging. Moreover, insights into the structural features and formation mechanism can be deduced from reductive desorption data [79].

Extensive surface characterizations have been applied to alkanethiolates on gold. For instance, X-ray photoelectron spectroscopy (XPS) has been used to identify the electronic state of the adsorbed sulfur atom as a thiolate [58] with a partial charge of -0.2 [70]. STM has also been used extensively to interrogate the resulting adlayer structure. The binding site of the sulfur head-group has been speculated to occur at three-fold hollow sites at Au(111), forming a $(\sqrt{3} \times \sqrt{3})R30°$ adlayer, as shown in Figure 3 [81, 82]. A recent report confirmed a three-fold binding site for sulfide layers on Au(111) [83]. In addition to the $(\sqrt{3} \times \sqrt{3})R30°$

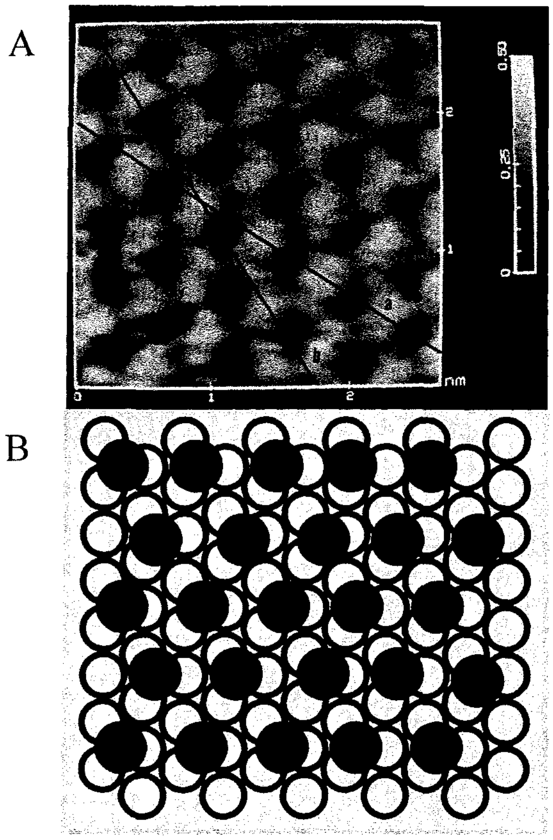

Figure 3. (A) STM image of ethanethiolate on Au(111). (B) ($\sqrt{3}$ x $\sqrt{3}$)*R*30° overlayer structure of a thiolate monolayer. Open circles represent Au atoms, while filled circles represent S atoms. Adapted from: C. A. Widrig, C. A. Alves, and M. D. Porter, J. Am. Chem. Soc. 113 (1991) 2805.

structure, there are numerous studies indicating more complicated registries [64], showing that there are many different possibilities for the over-lattice with respect to the surface crystallinity of the substrate.

3.3. Overall Characteristics

The main limitation of self-assembly is the requirement of a specific functional group. Fortunately, thiols on gold provide an ideal system for electrode modification, allowing facile control of interfacial properties at the molecular level [84]. However, the complex formation processes outlined above result in subtle variation of electrode performance, even when care is taken to maintain constant preparation conditions. To overcome this limitation, it is best to incorporate a quality control procedure that is dictated largely by the targeted application.

3.4. Applications

SAMs are widely used to block access of solution-based molecules [7]. Systematic studies of structural effects in electron transfer have often been carried out by covalently binding electroactive species to the end group [7, 42, 44-47, 85-87], in which precise control over the dielectric barrier thickness is achieved by varying the number of methylene units in the spacer chain. Freely diffusing (non-bonded) redox couples have also been used for this purpose, though care must be taken to eliminate [44-47] or account for [7, 88, 89] defects (pinholes and/or collapsed sites). Additionally, by systematic variation of the chemical moieties within the chain, the depth-sensitivity of surface-sensitive techniques (e.g., wetting) can be determined [90]. More detailed and comprehensive studies can delineate more subtle structure-function relationships in many interfacial properties, including long-range heterogeneous electron transfer [91-93]. For example, the effects of chain configuration [94, 95], terminal functionality [81], hydrogen bonding [96], and other variables [92, 97-99] on the electron tunneling efficiency and other properties have been reported.

The use of SAMs as a facile way to manipulate the chemical functionality of an electrode surface has also been exploited for chemical sensing purposes [63, 66]. For example, the construction of highly selective electrodes has been aided by incorporating cyclodextrins, calixarenes, and other molecules with size and shape specificity within an adsorbate precursor [49, 100]. SAM-modified electrodes are also utilized in biomimetics [66], studies of interfacial phenomenon [57], nanotechnology [57], and molecular electronics [66].

4. Review of Electroanalytical Techniques

A broad array of topics including mass transfer, thermodynamics, kinetics, and materials and surface science are all fundamental to electrochemistry. To describe any electrochemical system completely often requires that concepts central to many of these subjects be used in concert. A result of these interwoven relationships is a powerful suite of electroanalytical tools that can be applied for a variety of purposes. For example, in addition to traditional analytical applications, thermodynamic and kinetic parameters can be measured. These and other characteristics can even be correlated to the surface features of an electrode such that an electroanalytical method can serve as a surface characterization technique. A description of the techniques that are most relevant to the work in this dissertation follows.

4.1. Voltammetry

Few techniques in electroanalytical chemistry are more often utilized or provide more powerful diagnostics than voltammetry. The expansive utility of voltammetric techniques stems from their ability to quickly provide qualitative and quantitative insights into electrochemical mechanisms. For example, the shape of a voltammogram can be indicative of reversible or irreversible electron transfer reactions or implicate a particular electrode mechanism. Moreover, physicochemical constants that are directly related to these processes (e.g., reaction rates and diffusion coefficients) can be extracted using well-established theoretical relationships. Importantly, the shape of a voltammogram is normally used to identify the appropriate treatment for obtaining these parameters.

Cyclic voltammetric data is obtained by sweeping the electrode potential at a constant rate repeatedly between two or more limits. The initial and switching potentials are important parameters that must be chosen according to the form of the redox couple present and the information sought. Thus, the details of the potential program must take into consideration any constraints on the accessible potential window stemming from electrolysis of solvent components or of the electrode surface. Moreover, the derivation of theoretical equations to relate peak potentials (E_p), peak currents (i_p), and other important parameters usually impose some limits on the initial and switching potentials and sweep rate. In any case, the resulting current-potential (i-E) curve is rich in mechanistic information.

Cyclic voltammetry (CV) is a convenient method for measuring heterogeneous electron transfer rate constants (k^0). Two separate issues form the basis of these assessments. First, an applied potential (E_{appl}) is a thermodynamic quantity that is directly related to the Gibbs free-energy ($\Delta G^0 = -nFE_{appl}$). Thus, activated complex theory can be used to relate kinetic parameters to experimentally observed peak potential shifts [101]. Second, Faraday's law, when combined with Fick's laws of diffusion, can be used to directly obtain the flux of molecules at the electrode surface; in this situation, the current is a measure of the number of molecules that have successfully participated in the electron transfer reaction. Thus, by relating the number of successful reactions to the total possible number derived from the flux of the species to the electrode surface, a reaction rate constant can be obtained [4]. As we shall see, a wide range of rate constants can be determined using voltammetry.

A series of simulated (digital simulation is discussed in Section 4.4.) current-potential (i-E) curves are presented in Figure 4 for a range of standard heterogeneous electron transfer rate constant (k^0) values. The range of k^0 values and the experimental parameters were chosen to obtain curves that are characteristic of reversible, quasi-reversible, and irreversible electron transfer reactions.

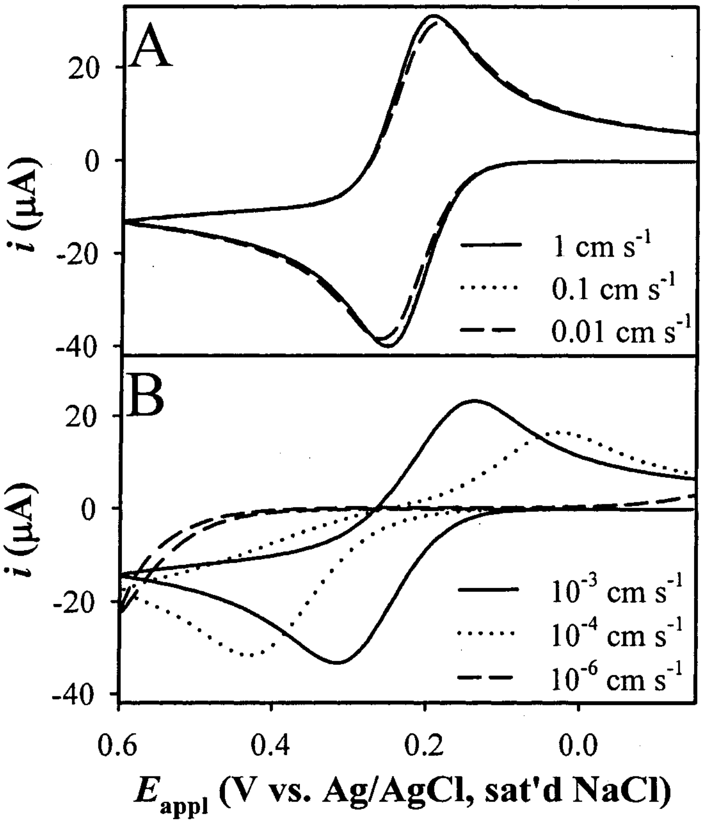

Figure 4. Simulated *i*-*E* curves for a wide range of k^0 values: (A) reversible; (B) quasi-reversible and irreversible. Electrode area: 0.026 cm^2, concentration: 10 mM (R, with an initial anodic scan), diffusion coefficient: 5 x 10^{-6} cm^2 s^{-1}, and sweep rate: 50 mV s^{-1} (contributions from solution resistance and capacitance omitted).

4.1.1 The Reversible Case

First, it is appropriate to define electrochemical reversibility, a concept that stems from the thermodynamic relationships first derived by Nernst (electrochemically reversible reactions are often called Nernstian). For a generic reduction reaction

$$\mathrm{O} + ne^- = \mathrm{R} \tag{3}$$

the Nernst relation is

$$E = E^{0\prime} + \frac{RT}{nF} \ln\left(\frac{C_{\mathrm{O}}}{C_{\mathrm{R}}}\right) \tag{4}$$

where E is the electrode potential, $E^{0\prime}$ is the formal reduction potential of the redox couple, R is the gas constant, T is absolute temperature, n is the electron stoichiometry, and C_i is the concentration of the oxidized (i = O) and reduced (i = R) forms of the redox couple.

The thermodynamic origins of the Nernst equation lead to the "reversible limit," a relative term that denotes facile heterogeneous electron transfer with respect to an experimental time scale. For example, in voltammetry, the potential is constantly changing. Thus, a reversible reaction is one that obeys the Nernst equation despite the potential sweep rate; this condition can only be maintained when the interfacial transformation between O and R is rapid (in both directions) relative to the perturbations of the applied potential. The reversible value of k^0 is therefore determined by a combination of the intrinsic value of k^0, the scan rate, and the diffusional characteristics of O and R (Nernstian reactions often lead to diffusion-limited diagnostics).

As shown in Figure 4A, when k^0 takes values that are close to, or exceed the reversible limit (for 50 mV s^{-1}, this value is ~0.1 cm s^{-1} when D is ~5 x 10^{-6} cm^2 s^{-1}), the curve shape undergoes only small changes as k^0 is varied. Any of these curves implicate a Nernstian electron transfer reaction. Moreover, when this type of curve is observed experimentally, the value of k^0 cannot be determined; instead, a lower limit for its value may be assigned based on the reversible limit with respect to the scan rate employed and the value of D. In some cases the sweep rate can be increased in order to access larger values of k^0 (see below).

Faraday's law states that the magnitude of an electrolytic current is directly proportional to the concentration of the redox couple that gives rise to the current. For a reversible reaction, the instantaneous concentration ratio [O]/[R] at the electrode surface is dictated by the Nernst equation. However, notice in Figure 4A that at certain potentials, there are peaks in the voltammetric current, while the Nernst equation predicts more positive overpotential ($\eta = E_{\mathrm{appl}} - E^{0\prime}$) to result in a decrease of [O]/[R] through the consumption of R; this should, when Faraday's law is applied, give a larger oxidation current. The origin of the peaks in a reversible *i-E* curve can be understood to arise from the limited availability of molecules. In other words, for an oxidation, the anodic voltammetric peak corresponds to a maximum in the number of R molecules impinging the electrode when the applied potential strongly favors oxidation. As the electrode potential is swept to more positive overpotentials, depletion of R sets in, and the current slowly tails to a level eventually matching that of the charging current.

In order to fully account for the overall reversible voltammetric wave shape, the effect of Nernstian equilibrium and the diffusional transport of O and R to and from the electrode surface must both be considered. When either O or R approaches the electrode surface through Brownian motion, the Nernst equation dictates the thermodynamically favored situation; the proper ratio of concentrations will be established based on the electrode potential. Thus, if there are no kinetic limitations, the Nernst condition is satisfied. However, when *E* becomes sufficiently anodic, for example, R will be instantly converted to O upon impinging the electrode until its concentration becomes zero at this plane. However, note that voltammetric peaks appear broad, with a long, drawn-out tail. This effect arises from the continued diffusion of R to the electrode surface, and is the origin of the term "diffusion-limited reaction" to describe a Nernstian process, and "diffusional tail" or "diffusional profile" when describing a reversible voltammogram.

The potential of a reversible voltammetric peak corresponds to a concentration ratio of 0.33 (or 3 for the reverse reaction). This situation corresponds to the balance of mass transfer of O and R. The solutions to Fick's second law of diffusion can be used to obtain the potential at which there is a maximum flux of R to the electrode (for an oxidation). This approach utilizes the Nernst equation to solve for the concentrations of O and R at the electrode surface. The electrode potential value for use in the Nernst equation is given by the sweep rate and starting potential. Thus, Faraday's law dictates that the potential of maximum flux must correspond to the reversible peak in current (i.e., when there is a maximum in delivery of material to the electrode, the current is at a corresponding maximum). The potential at which this peak appears is 30 mV $(n)^{-1}$ positive of $E^{0\prime}$ for an oxidation, and 30 mV $(n)^{-1}$ negative of $E^{0\prime}$ for a reduction. Thus, the peak separation for a Nernstian reaction is 60 mV $(n)^{-1}$, a valuable diagnostic when evaluating heterogeneous kinetics.

The voltammetric peak current (in Amperes) is directly related to the initial bulk concentration of the redox couple (C^b, mol cm^{-3}), as given by Randles-Sevcik equation

$$i_\mathrm{p} = 2.69 \times 10^5 n^{\frac{3}{2}} A D^{\frac{1}{2}} C^\mathrm{b} v^{\frac{1}{2}} \tag{5}$$

where n is the redox stoichiometry, A is the electrode area (cm^2), D is the diffusion coefficient (cm^2 s^{-1}), and v is the sweep rate (V s^{-1}) [102]. The Randles-Sevcik equation was derived by solving Fick's second law of diffusion with appropriate boundary conditions [102].

4.1.2. The Quasi-Reversible Case

A quasi-reversible heterogeneous electron transfer reaction is characterized by apparent kinetic limitations (i.e., the Nernst equation is not explicitly followed), but where both the forward and reverse reactions must be considered (i.e., not totally irreversible). The quasi-reversible designation is somewhat arbitrary in that the observation of a quasi-reversible reaction is dependent on the time scale of the experiment. For example, in voltammetry, the value of k^0 must be small enough that Nernstian equilibrium cannot be established before the potential takes a new value due to the sweep program.

The voltammetric characteristics of a quasi-reversible reaction are shown by two of the i-E curves (solid and dotted) in Figure 4B. Note that the current is diminished and the voltammograms appear spread out relative to the Nernstian shape. Importantly, the peak separation (ΔE_p) is useful for determining rate constants in the quasi-reversible range. Such an analysis is valid when ΔE_p is greater than the Nernstian value of 60 mV $(n)^{-1}$, but less than 212 mV $(n)^{-1}$, where the reaction begins to appear completely irreversible (see below).

A quasi-reversible value of k^0 is, once again, determined by the time scale in which the reaction is observed, and therefore on the voltammetric sweep rate and diffusional characteristics of the redox couple. For example, at a sweep rate of 50 mV s^{-1}, values of k^0 that are between 10^{-4} and 0.1 cm s^{-1} appear quasi-reversible (for a redox couple with a diffusion coefficient of 5×10^{-6} cm^2 s^{-1}). The separation between the anodic and cathodic peak potentials (ΔE_p) can be employed in this regime to determine values of k^0. Nicholson derived this relationship [101] by combining the electrochemical absolute rate equation and Fick's law for the case where the electrode potential is scanned at a constant rate. The electrokinetic factor (ψ) is directly calculated from values of ΔE_p, as given in Table 1 of reference [101]. The analytical equation that relates ψ to k^0 is

$$\psi = \frac{\left(\dfrac{D_O}{D_R}\right)^{\frac{\alpha}{2}} k^0}{\sqrt{\pi f D_O \nu}} \tag{6}$$

where D_i is the diffusion coefficient of the respective form of the couple, α is the transfer coefficient, f is nF/RT (F is the Faraday, R is the gas constant, and T is the absolute temperature), and the other variables have been defined previously. Most often, D_O is measured independently (e.g., using chronoamperometry [103]), and is assumed to be equal to D_R, and α is assumed to be 0.5 (ΔE_p is almost independent of α for values between 0.3 and 0.7 [4]). Thus, the equation simplifies to

$$k^0 = \psi\sqrt{\pi f D_O v} \tag{7}$$

where values of ΔE_p between 61 and 212 mV give values for ψ between 20 and 0.10.

While Nicholson's method indicates that the voltammetric sweep rate can be increased in order to access successively larger values of k^0, care must be taken in the application of Equation (7) to very rapid electrode reactions [104]. The resistance encountered between the working and reference electrodes (i.e., the uncompensated solution resistance, R_u) in a three-electrode cell can lead to a lag in the actual applied potential (E_{appl}) relative to the programmed potential (E_{prog}) at large sweep rates (i.e., $E_{appl} = E_{prog} \pm iR_u$) since current increases in proportion to the square root of scan rate (see Equation 5). Although compensation by specially designed circuitry is possible [105], these ohmic potential losses become increasingly severe as the sweep rate increases, and special care must be taken in electrochemical cell design [106], and in interpretation of data [104]. In practice, k^0 values up to 0.1 cm s^{-1} can be measured using cyclic voltammetry with little difficulty (scan rates of less than 0.5 V s^{-1} are required), and up to 5 cm s^{-1} in cases where special care is taken to minimize solution resistance effects [104].

4.1.3. The Irreversible Case

The dashed curve in Figure 4B shows an example of a totally irreversible response: in this case, there are no peaks, and only anodic current is observed (i.e., there is no contribution from the back reaction). In this regime, the value of the current is directly proportional to the heterogeneous electron transfer rate constant (k, recall that k^0 is the rate constant at the standard reduction potential). Thus, the measurement of k as a function of potential can be carried out in order to measure, for example, activation parameters [44]. The Butler-Volmer equation, sometimes referred to as the electrochemical absolute rate equation, relates current, potential, and k:

$$i = nFAk\left(C_{O}e^{-\alpha f(E-E^{0\prime})} - C_{R}e^{(1-\alpha)f(E-E^{0\prime})}\right) \tag{8}$$

where all variables have been defined previously [4]. By initially including only one form of the redox couple (e.g., O), assuming α is 0.5, and determining the current at $E^{0\prime}$, the absolute rate equation simplifies to a form useful for an irreversible reaction

$$i^{0} = nFAk^{0}C^{\mathrm{b}} \tag{9}$$

where the superscript 0 indicates measurement at $E^{0\prime}$.

In practice, a good test that can be quickly performed to determine if Equation (9) can be applied is variation of the voltammetric scan rate. An irreversible reaction produces a voltammogram that is virtually independent of sweep rate. In this case, the rate of heterogeneous electron transfer is low enough that the concentration of the redox couple does not change significantly from the bulk value at the electrode surface. Thus, the current magnitude gives a direct indication of the probability of electron transfer, and therefore of k^{0}.

Overall, cyclic voltammetry is a powerful technique for characterizing heterogeneous electron transfer kinetics over a wide range of reaction rates [107]. Moreover, this technique can also be applied to the investigation of more complex electrode mechanisms.

4.2. Electrochemical Impedance Spectroscopy

Alternating current (AC) techniques are a powerful way to gain insights into the properties of an electrochemical interface. Especially useful for studies of CMEs is electrochemical impedance spectroscopy (EIS). However, the sometimes non-intuitive mathematical treatments of the data can obscure this elegant methodology.

4.2.1. Experimental Approach

Experimentally, a small amplitude (5-10 mV) alternating voltage perturbation is applied to a working electrode with a constant DC bias, usually set at the formal reduction potential of the probe being studied. This DC potential is applied either by potentiostatic control or by including equal concentrations of both forms of the redox couple. The resulting current waveform at the same frequency as the voltage perturbation is analyzed in order to determine the real and imaginary components of the cell impedance. The input frequency is varied between 0.1 and 10^5 Hz. Normally, Fourier transform techniques or frequency analyzers are used to determine the impedances [108-110].

4.2.2. Data Analysis

The data that are ultimately collected in an EIS experiment are the real and imaginary cell impedances as function of frequency. These parameters are related to the amplitude and phase shift of the current wave form that results from each input voltage wave form, and contain a wealth of information about the electrochemical cell.

The characterization of a modified electrode is carried out with EIS by fitting experimental data to an equivalent circuit. Resistors, capacitors, and other components are arranged in a physically meaningful construct with respect to the system being studied. A best fit is determined by computer-controlled variation of the component values until a global minimum in an error signal is reached. If an acceptable fit is obtained, the parameters are directly representative of the properties of the electrochemical cell. For example, the double layer capacitance (C_{dl}), k^0, and solution resistance (R_{u}) can all be obtained from a single experiment. Importantly, a good equivalent circuit should contain a minimum of circuit elements, and each component should have a physically meaningful interpretation.

4.2.3. Applications of EIS

Although mathematically complex, EIS enables the assessment of relatively large heterogeneous electron transfer rate constants with respect to those accessible using cyclic voltammetry. For example, values for k^0 of up to 1.5 cm s^{-1} are obtained much more readily with EIS [4]. Moreover, since the equivalent circuit fitting procedure yields values for C_{dl}, k^0, and R_u simultaneously, several experimental difficulties in measuring k^0 can be circumvented. For example, the measurement of k^0 from an irreversible voltammogram must take into account the current due to double-layer charging, usually requiring an additional experiment in blank electrolyte solution. For an EIS experiment, the current due to double layer charging and heterogeneous electron transfer events are inherently separated into separate components in the equivalent circuit. Thus, EIS provides a complementary methodology that can ensure accurate values for k^0 are obtained.

A second strength of EIS lies in the ability to model physical processes using equivalent circuitry. In this way, more complex electrode mechanisms, electrodes that exhibit non-uniform behavior across their surface and other novel phenomenon can be studied [89, 111-114]. There are also many other AC techniques [4, 108]. Some of these are a combination of small amplitude AC voltage perturbations and larger DC sweeps (e.g., AC voltammetry), and others utilize harmonics of higher order than the fundamental (e.g., 2nd harmonic generation AC voltammetry).

4.3. Surface Characterization Techniques

Techniques that characterize important aspects of an interface are abundant in electroanalytical chemistry. For example, roughness and crystallinity can cause significant variation of the observed electrochemical response. Systematic correlations of surface features and electrode performance have been described in order to delineate important relationships. A general description of the potential programs, theory, and application of relevant techniques are given in this section.

4.3.1. Roughness and Crystallinity Determinations

Important characteristics of a metal electrode include the overall macroscopic roughness and crystallinity. Scanning probe, electron, and optical microscopies can provide information regarding the microstructure of an electrode; however, in order to obtain representative average roughness factors, these methods are generally impractical. Electrochemical methods allow facile determination of both roughness and crystallinity using cyclic voltammetry. This section details the literature and experimental procedures that enable these assessments.

The roughness of an electrode is characterized by a roughness factor (R_f). This parameter is defined by

$$R_f = \frac{A_r}{A_g} \tag{10}$$

where A_r is the real surface area and A_g is the geometric area. The value of R_f accounts for microscopic undulations and pits in the surface of the electrode.

Crystallinity is a measure of the surface structure of a substance [115]. That is, for a metal such as gold, there are several stable geometric arrangements of the atoms at the surface. The low index faces are the most important of these and can be used to describe a macroscopic gold electrode. Thus, the Au(100), Au(110), and Au(111) microfacets are all present to some extent at the surface of a polycrystalline gold electrode. The work in this dissertation requires a determination of the composition of the crystallinity of different gold electrodes (i.e., the approximate percentages of each low-index plane present at the surface).

4.3.2. Gold Oxide Formation and Stripping

A popular method for determining both R_f, and in some cases crystallinity, is the electrochemical formation and stripping of gold oxide [116, 117]. By sufficiently anodizing a gold electrode in acidic media (e.g., 1 M H_2SO_4), the surface becomes oxidized. Upon bringing the electrode to more negative potentials, the layer of gold oxide is stripped off the surface. Thus, cyclic voltammetry of a gold electrode between 0 and +1.5 V (vs. Ag/AgCl, sat'd NaCl) results in a characteristic *i-E* curve. Moreover, integration of the charge for the oxide stripping peak gives an estimate of A_r. Although these simple experiments provide a rough estimate, in practice it is difficult to obtain highly accurate R_f values since the depth of the oxidized layer depends on the sweep rate and the nature of the substrate (e.g., purity, crystallinity, and roughness). However, approximately 400 μC pass upon removal of 1.0 cm^2 of a single gold oxide layer [117].

Figure 5 shows two examples of gold oxidation-oxide stripping curves for relatively smooth and rough electrodes. First, the solid curve shows an electrode polished on 400-grit (coarse) abrasive. Note that the cathodic wave at ~+0.95 V is much larger than that for the electrode polished with 1200-grit (smooth) abrasive (dashed curve). These responses illustrate the qualitative characterization of roughness using this method (i.e., the electrode polished on the coarser abrasive shows a much larger cathodic stripping wave).

In addition to true surface area estimates, cyclic voltammetry of a gold electrode in acidic media can provide information about crystallinity. Through systematic studies of the low index faces of gold electrodes, Hamelin showed that the appearance of the *i-E* curve in

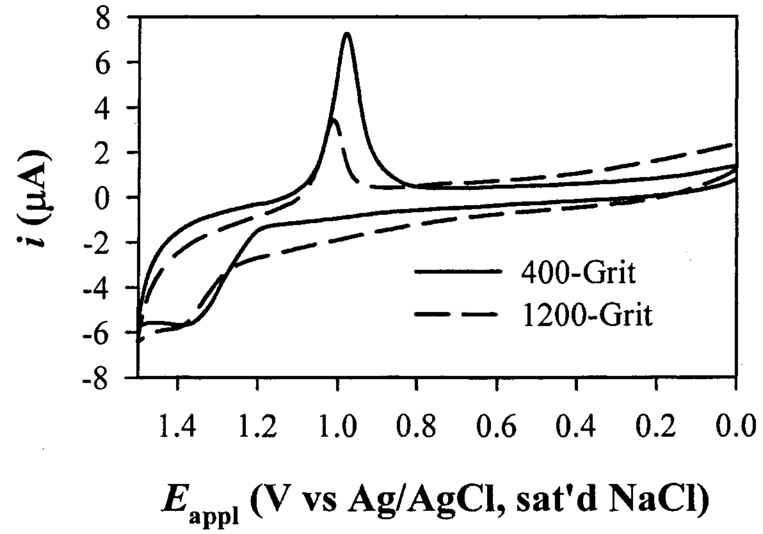

Figure 5. Electrochemical formation and stripping of gold oxide in 1 M H_2SO_4. Geometric electrode area: 0.020 cm^2, sweep rate: 5 mV s^{-1}. The broad anodic wave at ca. +1.3 V corresponds to gold oxide formation, while the sharp cathodic peak at ca. +0.95 V is the stripping of the oxide.

perchloric acid can be correlated to surface structure [118, 119]. Although the fine structure of the voltammogram depends on the details of the experimental procedure (i.e., acid concentration, sweep rate, and potential limits), these studies enable one to obtain an excellent idea of the crystallinity of a gold electrode by comparison.

Gold oxidation and stripping can quickly characterize an electrode. Moreover, the process of removing surface layers of gold atoms is often used as an electrochemical polishing treatment in the final step of electrode preparation (e.g., after mechanical polishing). The information provided by the stripping voltammogram can also be used as a quality control metric, allowing the experimenter to screen the surface character of each electrode after pretreatment procedures have been applied. This method is particularly useful for electrodes which are to be modified [120].

4.3.3. Stripping of Adsorbed Iodine

When more exacting roughness factors are required, the adsorption of an electroactive species with a well-known surface concentration can be employed. For gold, the adsorption of iodine has been developed for roughness factor determinations [121, 122]. The utility of this method stems from the highly characterized over-lattice of iodine on the noble metals. For example, when a gold electrode is soaked in a dilute solution of iodide or iodine, an adlayer of zero-valent iodine results, and has a surface concentration of 1.04 nmol cm^{-2}.

The adsorbed iodine layer, I(ad), can be removed electrochemically by sweeping the electrode potential anodically, resulting in the stripping of adsorbed zero-valent iodine to iodate according to

$$\mathrm{I(ad) + 3H_2O \rightarrow IO^{3-}(aq) + 6H^+(aq) + 5e^-} \qquad (11)$$

Thus, the charge required for this process can be used to determine the real surface area (A_r) of the gold electrode. However, because this reaction occurs concurrently with gold oxide formation, the charge should be background corrected. Fortunately, the oxide stripping peak is easily isolated in the same voltammogram. Moreover, this peak accounts for the exact amount of gold oxide formed on the positive potential scan. Thus, an internal background correction factor is obtained by integrating the charge for gold oxide stripping. Thus, A_r can be determined from

$$A_r = \frac{Q_I}{nF\Gamma_{I,calc}} \qquad (12)$$

where Q_I is the charge for stripping of the adsorbed iodine to iodate (background corrected), n is the electron stoichiometry (in this case, 5), F is the faraday, and $\Gamma_{I,calc}$ is the calculated surface concentration of a layer of adsorbed iodine (noted above).

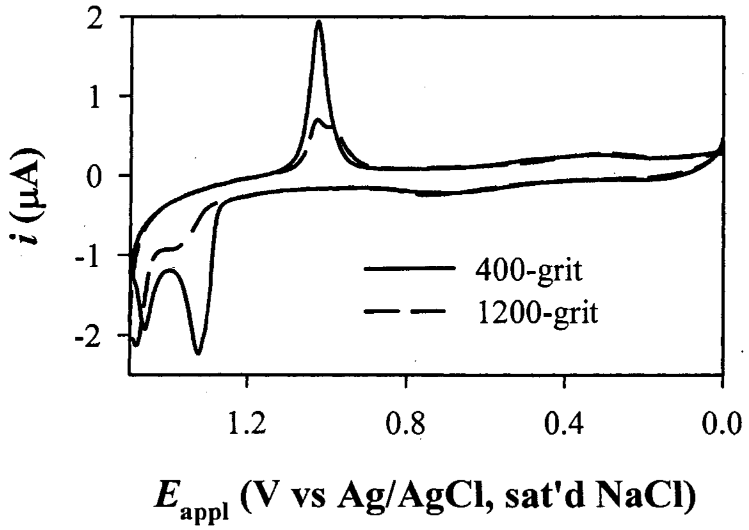

Figure 6. Stripping of adsorbed iodine from a gold electrode in 1 M H_2SO_4. Geometric electrode area: 0.020 cm^2, sweep rate: 5 mV s^{-1}. The additional anodic peak compared to Figure 5 corresponds to the anodic stripping (oxidation) of adsorbed iodine to iodate.

Figure 6 shows two *i-E* curves for gold electrodes polished with 400-grit (rough) and 1200-grit (smooth) abrasives. Note the additional anodic waves present at ~+1.35 V relative to Figure 5; these waves are due to the process in Equation (11). The value of Q_I is obtained by integration of the charge under these waves and subtraction of the charge for gold oxide stripping. For the examples shown in Figure 6, the analysis yields values for R_f of 1.4 and 2.5 for the smooth and rough surfaces, respectively.

4.3.4. Underpotential Deposition and Stripping of Lead

An intriguing and convenient method for crystallinity determination uses the underpotential deposition and stripping of lead [123-128]. The systematic studies by Hamelin [123, 124] provide a compelling basis for characterization of the crystallinity of gold electrodes. By applying the method to a clean gold surface, an excellent assessment of crystallinity is provided. Experimentally, all that is required is cycling of the gold electrode

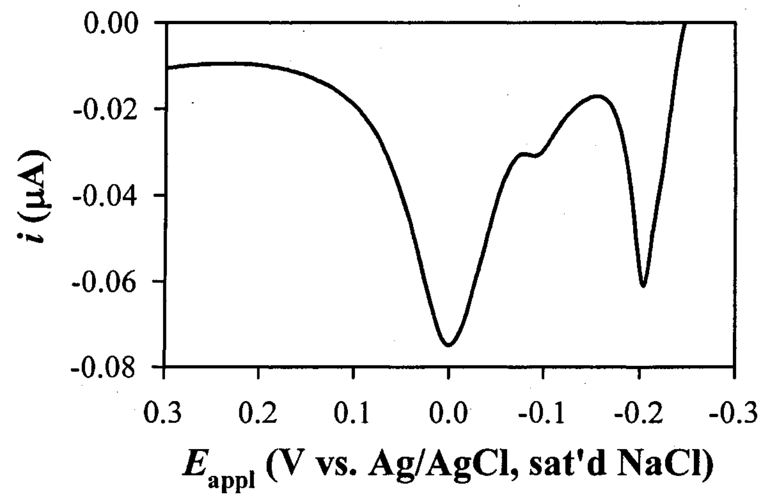

Figure 7. Stripping of underpotentially deposited lead in 1 M $HClO_4$ from a mechanically polished gold disk electrode. Geometric electrode area: 0.020 cm^2, R_f: 1.3, and sweep rate: 20 mV s^{-1}.

in a dilute (~1 mM) solution of lead oxide in 1 M H_2SO_4 at slow scan rates (i.e., 20 mV s^{-1}). Slow sweep rates are critical to maintaining equilibrium adsorption conditions.

Lead deposited on gold is striped off the surface by an anodic sweep of the electrode. The peak potentials of the resulting wave or waves correspond to the crystallographic face upon which the lead was adsorbed. Moreover, there are observable differences in the potential at which lead desorbs from terraces of different size. Thus, underpotential deposition and stripping of lead is a powerful and facile technique that can be used to obtain a macroscopic assessment of gold surface crystallinity.

An example of a stripping curve for underpotentially deposited lead at a polycrystalline gold disk electrode is shown in Figure 7. Several waves are observed, corresponding to the different low-index faces. By integrating the charge for each wave, and comparing it to the total charge for all waves, an approximate surface composition can be obtained. In the example shown, the surface is composed of 80% (110)-(100) terraces (peaks at +0.02 V and -

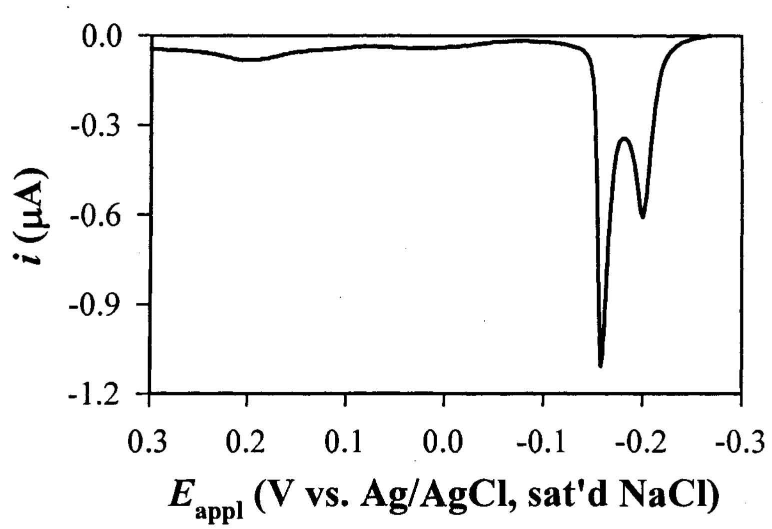

Figure 8. Stripping of underpotentially deposited lead in 1 M $HClO_4$ from an annealed gold on mica electrode. Geometric electrode area: 0.6 cm^2, $R_f = 1.0$, and sweep rate: 20 mV s^{-1}.

0.09 V) and 20% (111) terraces that are < 11 atoms in size (peak at -0.2 V). A wave located at -0.16 V is indicative of (111) terraces larger than 11 atoms (not observed in this case). For comparison, Figure 8 shows a lead stripping voltammogram for an annealed gold on mica electrode. Analysis of this curve shows that the surface is composed ≥ 95% (111) terraces (estimated detection limit), with 54% being larger than 11 atoms across.

4.4. Digital Simulation

Digital simulation enables insights into a wide variety of electrochemical processes [129]. This technique provides enhanced understanding of real systems through the convenience with which fundamental system variables can be altered and the projected response of the system observed. For example, the effect of physicochemical parameters on the shape of a voltammetric curve can be determined. Moreover, simulated data can be compared to experimental results to obtain estimates for rate constants and other quantities. In these ways, digital simulation enables systematic studies of complex electrode mechanisms.

Digital simulation can be particularly powerful in that highly accurate results can be obtained. This level of detail is due to the importance of mass transfer and kinetics in determining experimental results. For example, the profile of a current-potential or current-time plot for an electrochemical reaction depends strongly on the heterogeneous kinetics and the diffusional behavior of the redox couple. Fick's second law of diffusion states that the change in concentration of a molecule with respect to time is directly related to its spatial distribution in solution:

$$\frac{\partial C}{\partial t} = D\frac{\partial^2 C}{\partial x^2} \tag{13}$$

where C is the concentration of the diffusing molecule, t is time, x is distance, and D is the proportionality constant (diffusion coefficient). Fick's law allows the concentration profile of a substance to be described with respect to the surface of the electrode. A time-dependent form can be derived that relates how this profile changes as a reaction proceeds with respect to rate constants. However, the complexity involved in many electrochemical processes makes obtaining closed-form, analytical solutions to this equation difficult or impossible after the appropriate boundary conditions are imposed. Thus, numerical methodology is often employed to approximate the solution, to which digital simulation is ideally suited.

The flux of a particle undergoing Brownian motion through a viscous medium can be determined using a model that avoids solving any differential equations. The volume of solution adjacent to the electrode surface is divided into arbitrary two-dimensional segments (often called boxes) that initially contain a uniform distribution of the electroactive species. Boxes that are adjacent are allowed to exchange molecules in a given time segment. The total flux for each box is calculated for each time segment, setting up the new concentrations in each box. In this way, each time segment serves as one digital step. This numerical process continues for a series of time segments, and can be set-up to provide the concentration profiles of the electroactive species near the surface of an electrode of different geometries, reaction rates, diffusion coefficients, applied potentials, and so on.

Modern computing techniques have allowed the dissemination of digital simulation software packages that enable extensive variety in the electrode mechanisms that can be studied [130]. Thus, digital simulation is an indispensable tool in the study of many electroanalytical problems. This technique is applied extensively in order to systematically characterize redox recycling for current amplification in Chapters 2 and 3 [16, 17].

4.5. Other Techniques

There are many other important electrochemical techniques. Potential step methods, such as chronoamperometry [103, 131-140] and chronocoulometry [141-146] are often useful for: determining diffusion coefficients, and heterogeneous and homogeneous reaction rates; evaluating adsorption, geometric electrode areas, and electron stoichiometry; and characterizing cell time constants. In addition to potential step methods, there are many variations of voltammetric techniques with specialized potential programs (i.e., square wave, differential pulse, staircase, etc.) [4]. Moreover, potentiometry finds extensive application in the quantitative analysis of many species (e.g., H^+ or pH), using selective electrodes [147].

5. Structural Relationships in Heterogeneous Electron Transfer

Electron transfer reactions that occur at an interface are mechanistically dependent on the electronic configuration of the electron acceptor and donor, and the characteristics of any bridging moieties. Systematic studies of electron transfer behavior as a function of electrode architecture provides a basis for the evaluation of theoretical predictions. Moreover, these investigations provide the foundations necessary for achieving logically controlled design of electrochemical sensors. As discussed in Section 3, SAMs provide a facile conduit for this type of analysis. Not surprisingly, then, SAMs have been extensively applied to studies of bridge-mediated electron transfer using both tethered and freely diffusing redox couples.

Electron transfer theory has been the subject of numerous investigations in the last half-century [148]. In fact, Rudolph Marcus was awarded the Nobel Prize in Chemistry in 1992 "for his contributions to the theory of electron transfer reactions in chemical systems [149]." The extensive nature of this field precludes a thorough description; however, those aspects that are related to the studies in this dissertation are briefly outlined. In this case, relevant theory is limited to bridge-mediated electron transfer. Moreover, the effects of changing the structure of the molecular bridge are of particular importance.

We have already seen that increasing the thickness of a dielectric electron transfer barrier decreases the measured current in an exponential fashion (Equation 1). However, this treatment considers the barrier as a continuous medium, which does not take into account specific structural variations. For example, for a barrier consisting of an alkyl chain, the continuum model does not encompass structural factors like chain conformation. For through-bond tunneling, the electron transfer pathway is thought to consist of the combined lowest unoccupied molecular orbital for the bridge. This path is affected by the conformational orientation of the molecule since the overlap of the individual atomic orbitals is determined, in part, by the arrangement of the atoms.

Figure 9 shows an example of two possible pathways that may exist for a bridge mediated heterogeneous electron transfer. In (A), the electron passes straight through a single

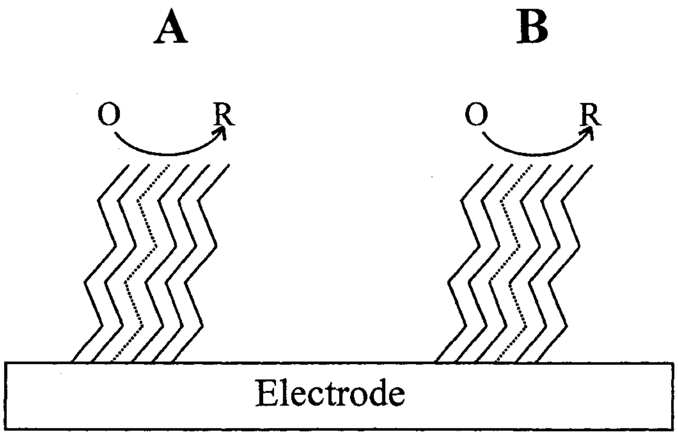

Figure 9. Electron transfer pathways (represented by the dotted line) for a bridge mediated event. (A) Regular event and (B) interchain coupling.

molecule in the barrier, while in (B) multiple molecules are involved. These through-bond pathways provide contrasting mechanisms; that is, interchain coupling (B) could either enhance or diminish the electron transfer rate with respect to the pathway in (A). The result obtained experimentally appears to depend on the structure and orientation of the molecules that make up the bridge. For example, interchain coupling appears to be more important when the molecules are highly tilted, disorganized, or contain functional groups [91, 92, 94, 96]. The multitude of possible phases and sub-structures that have been proposed for alkanethiolate monolayers on gold [56, 76, 82] serves to show that heterogeneous electron transfer across these barriers is a complex mechanistic issue; this is also illustrated by such novel phenomenon as quantum interference.

Quantum interference is an effect that arises as a consequence of the way in which individual atomic orbitals in the bridge overlap. For example, an electron tunneling pathway across a bridge composed of multiple repeating units (for example, an alkanethiolate with several methylene units) can provide significantly different coupling strengths for odd or even chain lengths. Marcus and Hsu [150, 151] derived theoretical relationships that demonstrated an oscillation (with respect to the chain length of a saturated bridge) of the coupling strength between an electrode and a donor tethered to the terminus of an alkanethiolate. Quantum interference was proposed as a possible origin for odd-even oscillations in k^0 reported by two different groups [86, 87] using tethered systems.

Collectively, quantum interference and interchain coupling demonstrate that there are many details of electron transfer that require further investigation. Chapter 5 presents data for the first observation of an odd-even effect in the heterogeneous electron transfer kinetics of solution-based redox couples at alkanethiolates on gold. In attempting to account for these data, these electron transfer theories will be useful; however, it is somewhat difficult to definitively determine the precise origins of this effect since we have also discovered an odd-even variation in thickness that may also cause such oscillations [23, 152].

Bridge mediated electron transfer theory also illustrates how interfacial architectures can be designed to exploit the structure-function relationships in certain applications. For example, fine-tuning selectivity can be achieved through very subtle changes in the electrode preparation conditions. Although the experimenter must invest extra time and care when developing such procedures, the sensitivity of electron transfer behavior to the fine structure of the adlayer further enhances the functions that can be achieved. As more knowledge is gained in both theoretical predictions and experimental methods, the application of chemically modified electrodes to a multitude of problems in electroanalytical chemistry will certainly continue to grow.

6. Non-Electrochemical Techniques

Often, complimentary information about the structure and properties of a modified electrode are obtained using spectroscopic, wetting, and other techniques. This section briefly discusses the theory and application of those techniques that are central to the work herein.

6.1. Infrared Reflection Absorption Spectroscopy

Vibrational spectroscopy has long been used for chemical structure analysis. Infrared spectroscopic studies of alkanes and related systems have revealed much regarding the details of conformation and packing arrangements [153-166]. Research focused on the application of this powerful characterization tool to study adsorbed molecules on metal surfaces was being developed by the late 1950s [167]. The further development of infrared reflection absorption spectroscopy (IRRAS) in the 1980s coincided with early reports on self-assembled monolayers [168-170]. IRRAS involves the measurement of an infrared spectrum of a coating at a reflective material. Interestingly, in addition to information regarding packing arrangements that stems from conventional IR spectroscopy, special selection rules in IRRAS can also enable determinations of film orientation [171].

6.1.1. Theory

The interaction of electromagnetic radiation with a highly reflective metal surface is of great importance to the interpretation of IRRAS spectra. Although infrared light is absorbed by a thin film on the surface of a metal due to the same processes that dictate absorption in conventional infrared spectroscopy (i.e., a change in dipole moment), IRRAS is concerned with the change in reflectivity that results. That is, a decrease in the intensity of reflected light occurs at each frequency corresponding to the vibrational modes of the adsorbed molecule. Importantly, this change in intensity, although modulated by the nature of the dipole derivative (i.e., its infrared cross-section), is proportional to the mean-square electric field ($<E^2>$) at the location of the absorbing unit [172].

The electric field of a light wave incident on a surface gives rise to an oscillation of the dipoles within the material. The irradiation of a highly conductive metal yields an oscillation of free electrons, and therefore the induced electric field oscillation is quite strong (i.e., with respect to a dielectric material that has only molecular dipoles), and such surfaces are highly reflective. When light reflected from a surface combines with the incident light (i.e., light that has not reached the surface yet), the interference pattern yields a standing wave in the electric field above the surface. The amplitude of the standing electric field is approximately twice as large as the incident electric field. Thus, the mean-square electric field ($<E^2>$) is four times the incident electric field at the standing wave maximum. Importantly, the locations of the nodes in this standing wave are dependent on the polarization state of the incident light.

The standing wave that results from the combination of the incident and reflected light is also affected by a phase shift that occurs upon reflection [167]. This effect varies with the angle of incidence and the polarization state of the radiation; for *p*-polarized light, as the angle of incidence draws near a grazing angle, the contribution from the interference of the phase shifted light becomes overwhelming since the phase shift approaches 180°. The standing wave in the electric field for *p*-polarized light is maximized at an 88° angle of incidence [167].

By consideration of the de-coupled Maxwell equation for electromagnetic radiation (only the electric field needs to be considered), the complex refractive index, and the Fresnel coefficients for reflection, the expressions for $<E^2>$ for the various polarization components can be obtained with respect to the incident mean-square electric field ($<E_0^2>$). Importantly, these results confirm that only the component in the direction of the surface normal (E_z) has significant intensity at the metal surface. Thus, for thin films (thickness much less than the wavelength of the incident light), only vibrational modes having a transition dipole that is aligned with this electric field vector will be excited. This effect enables the determination of film orientation [173].

The orientation dependence of the reflectivity for a particular vibrational mode arises from the polarization dependence of the standing electric field node locations. The free electrons of a metal are repelled from, and attracted to, areas where the instantaneous electric field vector is negative, and positive, respectively. Thus, as the incident electric field oscillates, this interaction creates an image charge. Consequently, any electric field oscillations parallel to the surface of a metal are effectively cancelled by the image charge, which is 180° out of phase with respect to incident *s*-polarized light. This effect results in a node in the standing electric field wave for *s*-polarized light at the surface of the metal. Note that this light is still reflected, but beginning at the surface of the metal, has zero amplitude (at a distance of one wavelength from the surface of the metal, its amplitude is at a maximum). On the other hand, an electric field that is aligned, at least partially, with the surface normal will yield an image charge that reinforces the original electric field. For example, the amplitude of the standing mean square electric field wave for *p*-polarized light at a gold surface is nearly four times the value of the incident electric field (following a similar pattern to the case for *s*-polarized light, at a distance of one wavelength from the metal its amplitude is at a minimum).

6.1.2. Application for Orientational Analysis

Due to the effects discussed in the previous section, the experimental set-up for an IRRAS experiment for a thin film on gold involves using only *p*-polarized light. The *s*-polarized light is filtered out before the sample since it will not contain any absorption information, but effectively adds a background signal to the detector. The angle of incidence is typically ~80°. Although higher angles (i.e., 88°) would potentially yield better sensitivity, alignment becomes difficult to maintain between the reference and sample measurements (a reference is required to establish the reflectivity in the absence of the film). Any misalignment between these measurements results in the distortion of band shapes, and the introduction of optical fringing effects, which can obscure the spectra.

For a thiolate monolayer on gold, the anisotropy of the electric field is useful for orientation determinations. The absorption intensity for a given vibrational mode (*A*) is proportional to the square of the product of the dipole moment derivative (*M*) and the electric field (*E*) at the location of the absorbing unit:

$$A \propto \left|M \bullet E\right|^2 \tag{14}$$

Since *p*-polarized light incident at a grazing angle yields an electric field vector that is normal to the surface, the value of *A* is also proportional to the cosine of the angle between the surface normal and the dipole derivative vector (θ):

$$A \propto \left|M \bullet E\right|^2 \propto \cos^2\theta \tag{15}$$

Thus, the expected absorption intensity for a film that has molecules randomly orientated should be three times smaller that that for a layer having all of the molecules oriented such that the dipole derivatives are normal to the surface:

$$\cos^2\theta = \frac{A_{\text{obs}}}{3A_{\text{calc}}} \tag{16}$$

where A_{obs} is the observed absorbance for the oriented thin film, and A_{calc} is that for an isotropic film of equivalent thickness. By correlating all of the absorption intensities of the modes of a particular molecule, values of θ can be obtained for each dipole derivative. By considering these values in light of the vector of the dipole derivative for each mode, the average orientation of the molecules in the thin film can be deduced [169].

6.2. Contact Angle

Wetting is a fundamental process related to many important physical and chemical concepts. For example, adhesion, surface tension, intermolecular forces, and surface potentials are all important in determining the wetting characteristics of a solid [174-176]. Wettability measurements have been used in many areas of surface science, including early reports [90, 177] and more recent works [98] on self-assembled monolayers.

6.2.1. Theory

A stable liquid drop suspended in air has a single interface: the liquid-gas boundary. In this case, the molecules in the respective phases are arranged in an equilibrium state that reflects a balance of the forces at work in the system. The geometry of the interface for free and stable liquid drops is spherical. An understanding of the forces that cause this geometry is required to recognize how bringing a liquid drop into contact with a solid surface (i.e., assessing the contact angle) can serve as a measure of surface free energy.

The collective forces between the molecules of a liquid result in two different effects: surface tension (γ_{lg}) and internal pressure (P_i). Surface tension is a two dimensional analogue of pressure; it can be thought of as free energy per unit area or force per unit length [176], and acts to hold the drop in a cohesive unit (thermodynamically, this cohesive force can be envisioned to arise from the interaction enthalpy). The internal pressure, on the other hand, is generated by the motion of the molecules within the liquid, which establishes a pressure difference across the interface (the thermodynamic parallel is entropy). This force acts to expand or distribute the drop, leading to complete miscibility for compatible phases (e.g., water and ethanol). At equilibrium, P_i is balanced by γ_{lg} such that the volume of the liquid has a minimized surface area; for a given volume with only one interface, the favored geometry is spherical since this shape minimizes the surface area.

The importance of thermodynamics in wettability, alluded to above, can be summarized by the condition for the formation of an interface: the surface free energy must be positive. If the surface free energy is negative (or zero), the interfacial region will continue to expand until the two phases are totally mixed [176]. This thermodynamic foundation forms the basis of systematic studies of interfaces through contact angle measurements.

When bringing a free liquid drop into contact with a solid surface, two additional interfaces result: the solid-gas and solid-liquid boundaries, each with their associated surface tensions (free energies). Balancing each of these surface tensions leads to an equilibrium that defines the way in which the liquid contacts the solid. That is, the area of the drop in contact with the surface (A) will vary in order to balance the relative magnitudes of the surface tensions at each boundary. For a drop with a constant volume, the area of the drop in contact

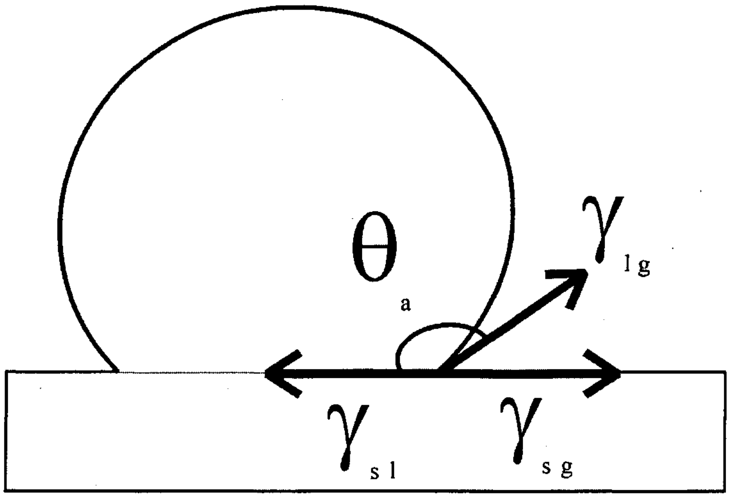

Figure 10. Illustration of the contact angle, with associated surface tension vectors.

with the surface defines a definite contact angle (θ), which is the angle between the solid-liquid and liquid-gas interfaces, as shown in Figure 10.

The values (magnitude and direction) of each surface tension vector are shown in Figure 10 for a model system. To illustrate how the contact area relates to the surface free energy and contact angle, a situation is envisioned in which a small (reversible) change in the contact area (ΔA) is accounted for by a corresponding change in the surface free energy (ΔG_s) and contact angle ($\Delta\theta$):

$$\Delta G_s = \Delta A(\gamma_{sl} - \gamma_{sg}) + \Delta A \gamma_{lg} \cos(\theta - \Delta\theta) \tag{17}$$

where γ is the surface tension for the solid-liquid (sl), solid-gas (sg), and liquid-gas (lg) interfaces. Since the change in free energy with respect to the change in contact area ($\Delta G_s/\Delta A$) must be zero at equilibrium, Equation (17) can be simplified and rearranged:

$$\cos\theta = \frac{\gamma_{sg} - \gamma_{sl}}{\gamma_{lg}} \tag{18}$$

Equation (18) is known as Young's equation. Importantly, the values of γ are not directly measured in a contact angle assessment. Instead, the value of θ represents the balance of the surface tensions. However, it is often assumed that there are no chemical or physical reactions between the solid and liquid [178] and that the values of γ_{sg} and γ_{lg} remain constant. Thus, Young's equation shows that larger values of θ translate to lower surface free energy.

Consideration of Figure 10 and Young's equation shows the relationship between each of the surface tension vectors and the contact angle. That is, each surface tension value can be visualized as a vector with an origin at the liquid-solid interface: the γ_{sg} vector and points along the surface and away from the liquid drop; the γ_{sl} vector is directly opposite γ_{sg} (thus, the length of the adjacent side of the triangle which represents the drop shape is given by the numerator of Equation (18)); and the γ_{lg} vector is oriented along the liquid-gas interface.

6.2.2. Hysteresis

Although contact angle measurements are ideally thermodynamic quantities, experimental observations of hysteresis (nearly always observed) demonstrates an apparent discrepancy in the rigorousness of this model. That is, there are two stable limiting values for θ that can be recorded; which value is obtained depends on whether the drop was brought to rest after advancing or receding across the substrate. This situation presents quite a problem to the application of thermodynamic theories and to the interpretation of data. Although an issue of wide contention, at least three sources of hysteresis have been identified: contamination, roughness, and macromolecular scale surface immobility (i.e., when there is a force required to move the three phase line) [174, 176, 179].

6.2.3. Examples

There are many demonstrated uses for contact angle measurements at thiolate coated gold surfaces. For example, the advancing contact angle of a water drop at the surface of a long chain alkanethiolate monolayer is quite large (ca. 115°). For comparative purposes, the value that is obtained for other hydrophobic surfaces (hexamethylethane and paraffin wax) is ~130° [180], while clean gold is wet (i.e., the contact angle approaches zero) [174]. Thus, assessments of contact angles can provide a quality-control criterion. Moreover, following the contact angle as a function of deposition conditions (e.g., the immersion time of the gold in the thiol solution) enables insights into the formation mechanism [120].

Another particularly useful application of contact angle measurements of SAMs involves the assessments structure-wettability relationships [90, 177, 181, 182]. These studies seek to relate terminal or buried functionality and chemical heterogeneity in order to elucidate depth sensitivities, the structural nature of molecular function, and fundamental aspects of wetting.

Examples of application for such studies is the ability to control adhesion [183] and controlling the shape of liquid lenses through the application of potential control [184].

Finally, contact angle titrations have been carried out in order to determine the reactivity of functional groups on surface. Thus, measurements of the pK_a for carboxylic acid or amine terminated monolayers have been reported [185]. Interestingly, significant differences are observed with respect to pK_a values of similar molecules in solution. These differences, although not fully understood, have been attributed to the restrictions involved in tethering one end of the molecule to a solid support, steric and inductive effects, and interactions between molecules in the adlayer [181].

6.3. Null Ellipsometry

The thickness of a coating can be assessed using ellipsometric measurements [186]. Moreover, high-precision determinations for both uniform and variable composition layers over a large range of thicknesses are accessible using an optical ellipsometer [186]. Thus, ellipsometry has been applied to study monolayers of thiolates on gold from the earliest reports of their preparation and characterization [61].

6.3.1. Theory

Ellipsometric film thickness measurements operate on the principles of polarized light. There are many different configurations and measurement techniques that can be applied to a variety of samples. For thiolate monolayers on gold, the most useful of these techniques is surface (or reflection) null ellipsometry.

Experimentally, a single wavelength (usually 6238 Å) light source is passed through a polarizer and compensator such that elliptically polarized light incident on the sample is reflected as plane-polarized light [187]. After reflection from the sample, the light beam enters the analyzer. The null condition is satisfied with the positions of the analyzer, polarizer, and compensators are such that no light reaches the detector. By noting the positions of all three devices, the *change* in the polarization state of the light can be determined. This change is related to the optical properties of the sample, including the refractive index of the substrate and the thickness and refractive index of any coatings.

The actual quantity obtained from a null ellipsometric measurement is the complex amplitude reflection ratio (ρ), or the ratio of the Fresnel reflection coefficients for *p*- and *s*-polarized light (r_p and r_s, respectively) [186]:

$$\rho = \frac{r_\mathrm{p}}{r_\mathrm{s}} = \tan\Psi e^{i\Delta} \tag{19}$$

where Ψ represents the differential change in the amplitude of the reflected wave (with respect to the incident wave), and Δ the change in phase:

$$\tan\Psi = \frac{|r_\mathrm{p}|}{|r_\mathrm{s}|} \tag{20}$$

$$\Delta = \delta_{r_\mathrm{p}} - \delta_{r_\mathrm{s}} \tag{21}$$

where δ_{r_p} and δ_{r_s} are the phase shifts for reflected light with respect to the incident *p*- and *s*-polarized components, respectively [186]. Thus, a change in the polarization state of the light upon reflection occurs as a consequence of the different changes in amplitude and phase shift of the electric field waves where the electric field vectors oscillate parallel and perpendicular to the plane of incidence. It should be noted that Ψ and Δ are often referred to as the ellipsometric angles. This terminology stems from the fact that Ψ is the angle whose tangent is the ratio of the amplitude attenuation of the electric field (i.e., the *p*-polarized to the *s*-polarized), and Δ is the difference in the phase shifts between the two components [186].

Since the values of Ψ and Δ represent the change in polarization state of the light upon reflection from the surface, the complex refractive index of the sample can be obtained. This transformation relies on Snell's law and the Fresnel complex-amplitude reflection coefficients. The complex refractive index is directly related to the properties of the sample, and is given by

$$N = n + ik \tag{22}$$

where *n* is the index of refraction and *k* is the extinction coefficient (often called the real and imaginary parts of the refractive index, respectively) [186]. By using Snell's law and the Fresnel complex-amplitude reflection coefficients [186], the values of *n* and *k* can be found in terms of ρ and the angle of incidence (Φ_0):

$$N_1 = N_0 \tan\Phi_0 \left[1 - \frac{4\rho}{(1+\rho)^2}\sin^2\Phi_0\right]^{\frac{1}{2}} \tag{23}$$

where N_1 is the complex refractive index of the sample and N_0 is that for the incident medium (usually air) [186]. Note that this analysis is valid for a two phase system (e.g., determination of the complex refractive index of gold in air). Although more complex systems (e.g., a thiolate monolayer on gold) require more terms and a corresponding increase in mathematical complexity, the concepts described here apply in a general sense. In any case, changes in Ψ and Δ can, in principle, be used to measure the refractive index and thickness of a substrate-supported film simultaneously [188]. However, in practice, difficulty arises for thin films such as monolayers, where the thickness to be measured is much less than the wavelength of light employed.

The accuracy with which Δ and Ψ can be determined depends on many things. For example, the sensitivity of these values to small changes in the real refractive index varies as the angle of incidence is changed. For gold, the sensitivity is maximized when the angle of incidence is ~70° [187]. Thus, by far the most common experimental set-up that is used to measure the thickness of thiolate monolayers on gold is a null ellipsometer set with a 70° angle of incidence.

6.3.2. Application to Thiolate Monolayers

To measure the thickness of a modifying layer, optical constants are measured with and without the coating present. A multiple phase model based on the classical electromagnetic theory outlined above is usually applied to process the raw data. For self-assembled alkanethiolate monolayers on gold, a three phase model is typically employed [61]. The underlying gold, adlayer, and air comprise the three phases. For thickness calculations using a single-wavelength instrument, the refractive indexes of the different phases must be input into the model; that for the underlying gold is found using the optical constants measured before adlayer deposition with a two-phase model (gold-air, where the refractive index of air is 1.0). The refractive index of the monolayer must be estimated.

Early reports [61, 180] utilized values of 1.45-1.5 for the adlayer refractive index. The origin of this range was established based on the bulk value for polyethylene. Although a 1-2 Å error is encountered from the uncertainty in the adlayer refractive index, the relative change in thickness for a series of monolayers of increasing chain length can still provide relevant structural data.

Errors commonly encountered in the characterization of thiolate monolayers include those based on spot-to-spot variability in the optical function of the gold substrates; e.g., local roughness and crystallinity variations. Nevertheless, Chapter 5 details a methodology that reduces the experimental error by spot matching the optical functions before and after adlayer deposition; this method enabled a subtle odd-even oscillation in thickness to be experimentally observed for the first time.

7. References

[1] C. M. Elliot and R. W. Murray, Anal. Chem. 48 (1976) 1247.

[2] B. F. Watkins, J. R. Behling, E. Kariv, and L. L. Miller, J. Am. Chem. Soc. 97 (1975) 3549.

[3] R. F. Lane and A. T. Hubbard, J. Phys. Chem. 77 (1973) 1401.

[4] A. J. Bard and L. R. Faulkner, Electrochemical Methods: Fundamentals and Applications, John Wiley & Sons, Inc., New York, 2001.

[5] P. N. Bartlett, P. Tebbutt, and R. G. Whitaker, Prog. Reaction Kinetics 16 (1991) 55.

[6] N. K. Chaki and K. Vijayamohanan, Biosens. Bioelectronics 17 (2002) 1.

[7] H. O. Finklea, "Electrochemistry of Organized Monolayers of Thiols and Related Molecules on Electrodes" in Electroanalytical Chemistry: A Series of Advances, A. J. Bard and I. Rubinstein, eds., Marcel Dekker, Inc., New York, 1996.

[8] H. O. Finklea, "Electroanalytical Methods: Self-Assembled Monolayers on Electrodes" in Encyclopedia of Analytical Chemistry, R. A. Meyers, ed. Vol. 11, John Wiley & Sons, Ltd, Chichester, 2000, p. 10090.

[9] R. W. Murray, "Molecular Design of Electrodes Surfaces" in Techniques of Chemistry, J. William H. Saunders and A. Weissberger, eds., Vol. 22, John Wiley & Sons, Inc., New York, 1992.

[10] R. W. Murray, "Chemically Modified Electrodes" in Electroanalytical Chemistry, A. J. Bard, ed. Vol. 13, Marcel Dekker, Inc., New York, 1984, p. 191.

[11] C. R. Martin and C. A. Foss, Jr., "Chemically Modified Electrodes" in Laboratory Techniques in Electroanalytical Chemistry, P. T. Kissinger and W. R. Heineman, eds., Marcel Dekker, Inc., New York, 1996.

[12] R. A. Durst, A. J. Bäumner, R. W. Murray, R. P. Buck, and C. P. Andrieux, Pure & Appl. Chem. 69 (1997) 1317.

[13] W. Kutner, J. Wang, M. L'Her, and R. P. Buck, Pure & Appl. Chem. 70 (1998) 1301.

[14] L. Coche-Guerente, V. Desprez, J.-P. Diard, and P. Labbe, J. Electroanal. Chem. 470 (1999) 53.

[15] L. Coche-Guerente, V. Desprez, P. Labbe, and J.-P. Diard, J. Electroanal. Chem. 470 (1999) 61.

[16] A. J. Bergren and M. D. Porter, J. Electroanal. Chem. 585 (2005) 172.

[17] A. J. Bergren and M. D. Porter, J. Electroanal. Chem. Submitted (2005).

[18] P. T. Radford and S. E. Creager, Anal. Chim. Acta 449 (2001) 199.

[19] P. T. Radford, M. French, and S. E. Creager, Anal. Chem. 71 (1999) 5101.

[20] S. E. Creager and P. T. Radford, J. Electroanal. Chem. 500 (2001) 21.

[21] A. J. Bergren and M. D. Porter, J. Electroanal. Chem. In Preparation (2006).

[22] A. J. Bergren, G. A. Edwards, E. J. Cox, and M. D. Porter, In Preparation (2006).

[23] A. J. Bergren, G. A. Edwards, E. J. Cox, and M. D. Porter, In Preparation (2006).

[24] P. T. Kissinger and W. R. Heineman, "Laboratory Techniques in Electroanalytical Chemistry", Marcel Dekker, Inc., New York, 1996.

[25] J. Wang, "Electrochemical Preconcentration" in Laboratory Techniques in Electroanalytical Chemistry, P. T. Kissinger and W. R. Heineman, eds., Marcel Dekker, New York, 1996, p. 719.

[26] J. F. Evans, T. Kuwana, M. T. Henne, and G. P. Royer, J. Electroanal. Chem. 80 (1977) 409.

[27] F. W. Scheller, U. Wollenberger, C. Lei, W. Jin, B. Ge, C. Lehmann, F. Lisdat, and V. Fridman, Rev. Molecular Biotechnol. 82 (2002) 411.

[28] C. P. Andrieux, G. Delgado, J. M. Savéant, and K. B. Su, J. Electroanal. Chem. 348 (1993) 141.

[29] C. P. Andrieux and J.-M. Savéant, J. Electroanal. Chem. 205 (1986) 43.

[30] C. P. Andrieux, J. M. Dumas-Bouchiat, and J. M. Savéant, J. Electroanal. Chem. 113 (1980) 1.

[31] C. P. Andrieux, C. Blocman, J. M. Dumas-Bouchiat, F. M'halla, and J. M. Savéant, J. Electroanal. Chem. 113 (1980) 19.

[32] C. P. Andrieux, J. M. Dumas-Bouchiat, and J. M. Savéant, J. Electroanal. Chem. 87 (1978) 39.

[33] C. P. Andrieux, J. M. Dumas-Bouchiat, and J. M. Savéant, J. Electroanal. Chem. 88 (1978) 43.

[34] C. P. Andrieux, J. M. Dumas-Bouchiat, and J. M. Savéant, J. Electroanal. Chem. 87 (1978) 55.

[35] C. P. Andrieux and J. M. Savéant, J. Electroanal. Chem. 93 (1978) 163.

[36] J. M. Savéant and S. K. Binh, J. Electroanal. Chem. 91 (1978) 35.

[37] J. M. Savéant and K. B. Su, J. Electroanal. Chem. 171 (1984) 341.

[38] J. M. Savéant and K. B. Su, J. Electroanal. Chem. 196 (1985) 1.

[39] J. M. Savéant and F. Xu, J. Electroanal. Chem. 208 (1986) 197.

[40] L. Nadjo, J. M. Savéant, and K. B. Su, J. Electroanal. Chem. 196 (1985) 23.

[41] R. A. Marcus, Electrochim. Acta 13 (1968) 995.

[42] J. J. Sumner, K. S. Weber, L. A. Hockett, and S. E. Creager, J. Phys. Chem. B 104 (2000) 7449.

[43] A. T. Hubbard, Chem. Rev. 88 (1988) 633.

[44] A. M. Becka and C. J. Miller, J. Phys. Chem. 96 (1992) 2657.

[45] A. M. Becka and C. J. Miller, J. Phys. Chem. 97 (1993) 6233.

[46] C. Miller and M. Gratzel, J. Phys. Chem. 95 (1991) 5225.

[47] C. Miller, P. Cuendet, and M. Gratzel, J. Phys. Chem. 95 (1991) 877.

[48] M. R. de Jong, J. Huskens, and D. N. Reinhoudt, Chem. Eur. J. 7 (2001) 4164.

[49] M. Weisser, G. Nelles, G. Wenz, and S. Mittler-Neher, Sens. Actuators, B 38-39 (1997) 58.

[50] F. Malem and D. Mandler, Anal. Chem. 65 (1993) 37.

[51] I. Turyan and D. Mandler, Anal. Chem. 66 (1994) 58.

[52] I. Turyan and D. Mandler, Anal. Chem. 69 (1997) 894.

[53] S. Petrash, N. B. Sheller, W. Dando, and M. D. Foster, Langmuir 13 (1997) 1881.

[54] S. Petrash, T. Cregger, B. Zhao, E. Pokidysheva, M. D. Foster, W. J. Brittain, V. Sevastianov, and C. F. Majkrzak, Langmuir 17 (2001) 7645.

[55] D. J. Vanderah, G. Valincius, and C. W. Meuse, Langmuir 18 (2002) 4674.

[56] N. Sandhyarani and T. Pradeep, Int. Rev. Phys. Chem. 22 (2003) 221.

[57] J. C. Love, L. A. Estroff, J. K. Kriebel, R. G. Nuzzo, and G. M. Whitesides, Chem. Rev. 105 (2005) 1103.

[58] C. D. Bain, H. A. Biebuyck, and G. M. Whitesides, Langmuir 5 (1989) 723.

[59] R. G. Nuzzo and D. L. Allara, J. Am. Chem. Soc. 105 (1983) 4481.

[60] R. G. Nuzzo, F. A. Fusco, and D. L. Allara, J. Am. Chem. Soc. 109 (1987) 2358.

[61] M. D. Porter, T. B. Bright, D. L. Allara, and C. E. D. Chidsey, J. Am. Chem. Soc. 109 (1987) 3559.

[62] P. E. Laibinis, G. M. Whitesides, D. L. Allara, Y.-T. Tao, A. N. Parikh, and R. G. Nuzzo, J. Am. Chem. Soc. 113 (1991) 7152.

[63] S. Flink, F. C. J. M. v. Veggel, and D. N. Reinhoudt, Sensors Update 8 (2001) 3.

[64] A. Ulman, Chem. Rev. 96 (1996) 1533.

[65] A. Ulman, An Introduction to Ultrathin Organic Films From Langmuir-Blodgett to Self-Assembly, Academic Press, San Diego, CA, 1991.

[66] F. Schreiber, J. Phys.: Condens. Matter 16 (2004) R881.

[67] N. Camillone III, Langmuir 20 (2004) 1199.

[68] G. Hahner, C. Wöll, M. Buck, and M. Grunze, Langmuir 9 (1993) 1955.

[69] D. Qu and M. Morin, J. Electroanal. Chem. 524-525 (2002) 77.

[70] C.-J. Zhong, R. C. Brush, J. Andregg, and M. D. Porter, Langmuir 15 (1999) 518.

[71] R. Subramanian and V. Lakshminarayanan, Electrochim. Acta 45 (2000) 4501.

[72] M. Cohen-Atiya and D. Mandler, J. Electroanal. Chem. 550-551 (2003) 267.

[73] W. Pan, C. J. Durning, and N. J. Turro, Langmuir 12 (1996) 4469.

[74] D. S. Karpovich and G. J. Blanchard, Langmuir 10 (1994) 3315.

[75] C. D. Bain and G. M. Whitesides, J. Am. Chem. Soc. 111 (1989) 7164.

[76] G. E. Poirier and E. D. Pylant, Science 272 (1996) 1145.

[77] M. Byloos, H. Al-Maznai, and M. Morin, J. Phys. Chem. B 105 (2001) 5900.

[78] J. H. Teuscher, L. J. Yeager, H. Yoo, J. E. Chadwick, and R. L. Garrell, Faraday Discuss. 107 (1997) 399.

[79] C. A. Widrig, C. Chung, and M. D. Porter, J. Electroanal. Chem. 310 (1991) 335.

[80] M. M. Walczak, C. Chung, S. M. Stole, C. A. Widrig, and M. D. Porter, J. Am. Chem. Soc. 113 (1991) 2370.

[81] C. E. D. Chidsey and D. N. Loiacono, Langmuir 6 (1990) 682.

[82] C. A. Widrig, C. A. Alves, and M. D. Porter, J. Am. Chem. Soc. 113 (1991) 2805.

[83] M. D. Lay, K. Varazo, and J. L. Stickney, Langmuir 19 (2003) 8416.

[84] C.-J. Zhong and M. D. Porter, Anal. Chem. 67 (1995) 709A.

[85] S. Terrettaz, A. M. Becka, M. J. Traub, J. C. Fettinger, and C. J. Miller, J. Phys. Chem. 99 (1995) 11216.

[86] J. F. Smalley, S. W. Feldberg, C. E. D. Chidsey, M. R. Linford, M. D. Newton, and Y.-P. Liu, J. Phys. Chem. 99 (1995) 13141.

[87] K. Weber, L. Hockett, and S. Creager, J. Phys. Chem. B 101 (1997) 8286.

[88] E. Sabatani and I. Rubinstein, J. Phys. Chem. 91 (1987) 6663.

[89] H. O. Finklea, D. A. Snider, J. Fedyk, E. Sabatani, Y. Gafni, and I. Rubinstein, Langmuir 9 (1993) 3660.

[90] C. D. Bain and G. M. Whitesides, J. Am. Chem. Soc. 110 (1988) 5897.

[91] H. Yamamoto and D. H. Waldeck, J. Phys. Chem. B 106 (2002) 7469.

[92] A. M. Napper, H. Liu, and D. H. Waldeck, J. Phys. Chem. B 105 (2001) 7699.

[93] P. Cyganik, M. Buck, W. Azzam, and C. Wöll, J. Phys. Chem. B 108 (2004) 4989.

[94] K. Slowinski, R. V. Chamberlain, C. J. Miller, and M. Majda, J. Am. Chem. Soc. 119 (1997) 11910.

[95] M. Galperin, A. Nitzan, S. Sek, and M. Majda, J. Electroanal. Chem. 550-551 (2003) 337.

[96] H. O. Finklea, L. Liu, M. S. Ravenscroft, and S. Punturi, J. Phys. Chem. 100 (1996) 18852.

[97] J. J. Sumner and S. E. Creager, J. Am. Chem. Soc. 122 (2000) 11914.

[98] H.-T. Rong, S. Frey, Y.-J. Yang, M. Zharnikov, M. Buck, M. Wuhn, C. Wöll, and G. Helmchen, Langmuir 17 (2001) 1582.

[99] J. J. Sumner and S. E. Creager, J. Phys. Chem. B 105 (2001) 8739.

[100] F. Davis and C. J. M. Stirling, Langmuir 12 (1996) 5365.

[101] R. S. Nicholson, Anal. Chem. 37 (1965) 1351.

[102] J. E. B. Randles, Trans. Faraday Soc. 44 (1948) 327.

[103] P. J. Lingane, Anal. Chem. 36 (1964) 1723.

[104] A. M. Bond, T. L. E. Henderson, D. R. Mann, W. Thormann, and C. G. Zoski, Anal. Chem. 60 (1988) 1878.

[105] D. K. Roe, "Overcoming Solution Resistance with Stability and Grace in Potentiostatic Circuits" in Laboratory Techniques in Electroanalytical Chemistry, P. T. Kissinger and W. R. Heineman, eds., Marcel Dekker, New York, 1996, p. 195.

[106] F. M. Hawkridge, "Electrochemical Cells" in Laboratory Techniques in Electroanalytical Chemistry, P. T. Kissinger and W. R. Heineman, eds., Marcel Dekker, New York, 1996, p. 267.

[107] A. M. Bond, Modern Polarographic Methods in Analytical Chemistry, Marcel Dekker, New York, 1980.

[108] D. D. Macdonald and M. C. H. McKubre, "Impedance Measurements in Electrochemical Systems" in Modern Aspects of Electrochemistry No. 14, J. O. M. Bockris, B. E. Conway, and R. E. White, eds., Plenum Press, New York, 1982.

[109] D. D. Macdonald, Transient Techniques in Electrochemistry, Plenum Press, New York, 1977.

[110] S.-M. Park and J.-S. Yoo, 75 (2003) 455A.

[111] R. P. Janek, W. R. Fawcett, and A. Ulman, J. Phys. Chem. B 101 (1997) 8550.

[112] P. Diao, D. Jang, X. Cui, D. Gu, R. Tong, and B. Zhong, J. Electroanal. Chem. 464 (1999) 61.

[113] T. Komura, T. Yamaguchi, H. Shimatani, and R. Okushio, Electrochim. Acta 49 (2004) 597.

[114] R. Schweiss, C. Werner, and W. Knoll, J. Electroanal. Chem. 540 (2003) 145.

[115] K. W. Kolasinski, Surface Science: Foundations of Catalysis and Nanoscience, John Wiley & Sons, Ltd., Chichester, 2002.

[116] D. Dickertmann, J. W. Schultze, and K. J. Vetter, J. Electroanal. Chem. 55 (1974) 429.

[117] R. Woods, Chemisorption at Electrodes: Hydrogen and Oxygen on Noble Metals and their Alloys, Marcel Dekker, Inc., New York, 1976.

[118] A. Hamelin, J. Electroanal. Chem. 407 (1996) 1.

[119] A. Hamelin, M. J. Weaver, M. J. Sottomayor, F. Silva, and S.-C. Chang, J. Electroanal. Chem. 295 (1990) 291.

[120] G. A. Edwards, A. J. Bergren, E. J. Cox, and M. D. Porter, In Preparation (2006).

[121] M. R. Deakin, T. T. Li, and O. R. Melroy, J. Electroanal. Chem. 243 (1988) 343.

[122] J. F. Rodriguez, T. Mebrahtu, and M. P. Soriaga, J. Electroanal. Chem. 233 (1987) 283.

[123] A. Hamelin, J. Electroanal. Chem. 165 (1984) 167.

[124] A. Hamelin and J. Lipkowski, J. Electroanal. Chem. 171 (1984) 317.

[125] R. Adzic, E. Yeager, and B. D. Cahan, J. Electrochem. Soc. 121 (1974) 474.

[126] K. Engelsmann, W. J. Lorenz, and E. Schmidt, J. Electroanal. Chem. 114 (1980) 1.

[127] O. Melroy, K. Kanazawa, J. G. Gordon, II, and D. Buttry, Langmuir 2 (1986) 697.

[128] J. Perdereau, J. P. Biberian, and G. E. Rhead, J. Phys. F: Metal Phys. 4 (1974) 799.

[129] D. Britz, Digital Simulation in Electrochemistry, Springer-Verlag, New York, 1988.

[130] M. Rudolph, D. P. Reddy, and S. W. Feldberg, Anal. Chem. 66 (1994) 590A.

[131] J. M. Savéant and E. Vianello, Electrochim. Acta 8 (1963) 905.

[132] R. C. Bess, S. E. Cranston, and T. H. Ridgway, Anal. Chem. 48 (1976) 1619.

[133] D. H. Evans and M. J. Kelly, Anal. Chem. 54 (1982) 1727.

[134] J. Galvez, M. L. Alcaraz, and J. Vera, Anal. Chem. 66 (1994) 2935.

[135] H. Ikeuchi and M. Kanakubo, J. Electroanal. Chem. 493 (2000) 93.

[136] R. J. Lawson and J. T. Maloy, Anal. Chem. 46 (1974) 559.

[137] H. Matsuda, T. Gueshi, and K. Tokuda, J. Electroanal. Chem. 89 (1978) 247.

[138] N. Oyama, T. Oshaka, T. Sotomura, and H. Matsuda, Bull. Chem. Soc. Japan 56 (1983) 3065.

[139] S. C. Petrovic and R. H. Hammericksen, Electroanalysis 14 (2002) 599.

[140] J.-S. Yu and Z.-X. Zhang, J. Electroanal. Chem. 439 (1997) 73.

[141] F. C. Anson, Anal. Chem. 36 (1964) 932.

[142] F. C. Anson, Anal. Chem. 38 (1966) 54.

[143] F. C. Anson, J. H. Christie, and R. A. Osteryoung, J. Electroanal. Chem. 13 (1967) 343.

[144] F. C. Anson and D. A. Payne, J. Electroanal. Chem. 13 (1967) 35.

[145] B. Case and F. C. Anson, J. Phys. Chem. 71 (1967) 402.

[146] J. H. Christie, R. A. Osteryoung, and F. C. Anson, J. Electroanal. Chem. 13 (1967) 236.

[147] D. T. Sawyer, A. Sobkowiak, and J. L. Roberts, Jr., Electrochemistry for Chemists, John Wiley & Sons, Inc., New York, 1995.

[148] C. J. Miller, "Heterogeneous Electron Transfer Kinetics at Metallic Electrodes" in Physical Electrochemistry: Principles, Methods, and Applications, I. Rubinstein, ed., Marcel Dekker, Inc., New York, 1995.

[149] The Nobel Foundation, http://nobelprize.org/chemistry/laureates/1992/index.html, 1992

[150] C.-P. Hsu, J. Electroanal. Chem. 438 (1997) 27.

[151] C.-P. Hsu and R. A. Marcus, J. Chem. Phys. 106 (1997) 584.

[152] G. A. Edwards, A. J. Bergren, E. J. Cox, and M. D. Porter, (2006).

[153] A. L. Aljibury, R. G. Snyder, H. L. Strauss, and K. Raghavachari, J. Chem. Phys. 84 (1986) 6872.

[154] H. L. Casal, H. H. Mantsch, D. G. Cameron, and R. G. Snyder, J. Chem. Phys. 77 (1982) 2825.

[155] R. A. MacPhail, R. G. Snyder, and H. L. Strauss, J. Chem. Phys. 77 (1982) 1118.

[156] M. Maroncelli, H. L. Strauss, and R. G. Snyder, J. Chem. Phys. 82 (1985) 2811.

[157] D. H. Reneker, J. Mazur, J. P. Colson, and R. G. Snyder, J. Appl. Phys. 51 (1980) 5080.

[158] R. G. Snyder, J. Molecular Spectrosc. 7 (1961) 116.

[159] R. G. Snyder, J. Chem. Phys. 42 (1965) 1744.

[160] R. G. Snyder, S. L. Hsu, and S. Krimm, Spectrochimica Acta, Part A: Molecular and Biomolecular Spectroscopy 34A (1978) 395.

[161] R. G. Snyder, J. Chem. Phys. 71 (1979) 3229.

[162] R. G. Snyder and J. R. Scherer, J. Chem. Phys. 71 (1979) 3221.

[163] R. G. Snyder, H. L. Strauss, and C. A. Elliger, J. Phys. Chem. 86 (1982) 5145.

[164] R. G. Snyder, A. L. Aljibury, H. L. Strauss, H. L. Casal, K. M. Gough, and W. F. Murphy, J. Chem. Phys. 81 (1984) 5352.

[165] R. G. Snyder, M. Maroncelli, H. L. Strauss, and V. M. Hallmark, J. Phys. Chem. 90 (1986) 5623.

[166] R. G. Snyder, Macromolecules 23 (1990) 2081.

[167] R. G. Greenler, J. Chem. Phys. 44 (1966) 310.

[168] D. L. Allara and J. D. Swalen, J. Phys. Chem. 86 (1982) 2700.

[169] D. L. Allara and R. G. Nuzzo, Langmuir 1 (1985) 52.

[170] D. L. Allara and R. G. Nuzzo, Langmuir 1 (1985) 45.

[171] M. Moskovits, J. Phys. Chem. 77 (1982) 4408.

[172] R. J. Lipert, B. D. Lamp, and M. D. Porter, "Infrared Specular Reflection Spectroscopy: A Versatile Approach to the Characterization of Interfaces" in <u>Modern Techniques in Applied Molecular Spectroscopy</u>, F. Mirabella, ed., Wiley Interscience, New York, 1996.

[173] M. D. Porter, Anal. Chem. 60 (1988) 1143A.

[174] J. Israelachvili, <u>Intermolecular and Surface Forces</u>, Academic Press, New York, 1992.

[175] K. L. Mittal, "Contact Angle, Wettability, and Adhesion", <u>3</u>, VSP BV, Boston, 2003.

[176] A. W. Adamson, Physical Chemistry of Surfaces, John Wiley & Sons, New York, 1982.

[177] C. D. Bain and G. M. Whitesides, J. Am. Chem. Soc. 110 (1988) 3665.

[178] J. Yang, J. Han, K. Isaacson, and D. Y. Kwok, "Effects of Surface Defect, Polycrystallinity and Nanostructure of Self-Assembled Monolayers on Wetting and its Interpretation" in Contact Angle, Wettability and Adhesion, K. L. Mittal, ed. Vol. 3, VSP BV, Boston, 2003, p. 319.

[179] F. M. Fowkes and W. D. Harkins, J. Am. Chem. Soc. 62 (1940) 3377.

[180] C. D. Bain, E. B. Troughton, Y.-T. Tao, J. Evall, G. M. Whitesides, and R. G. Nuzzo, J. Am. Chem. Soc. 111 (1989) 321.

[181] G. M. Whitesides and P. E. Laibinis, Langmuir 6 (1990) 87.

[182] J. Drelich, J. L. Wilbur, J. D. Miller, and G. M. Whitesides, Langmuir 12 (1996) 1913.

[183] M. Mrksich, C. S. Chen, Y. Xia, L. E. Dike, D. E. Ingber, and G. M. Whitesides, Proc. Natl. Acad. Sci. 93 (1996) 10775.

[184] C. B. Gorman, H. A. Biebuyck, and G. M. Whitesides, Langmuir 11 (1995) 2242.

[185] S. E. Creager and J. Clarke, Langmuir 10 (1994) 3675.

[186] R. M. A. Azzam and N. M. Bashara, Ellipsometry and Polarized Light, Elsevier, New York, 1977.

[187] T. E. Jenkins, J. Phys. D: Appl. Phys. 32 (1999) R45.

[188] D. Ducharme, A. Tessier, and S. C. Russev, Langmuir 17 (2001) 7529.

CHAPTER 2. ELECTROCHEMICAL AMPLIFICATION USING SELECTIVE SELF-ASSEMBLED ALKANETHIOLATE MONOLAYERS ON GOLD. A PREDICTIVE MECHANISTIC MODEL

A paper published in *The Journal of Electroanalytical Chemistry* 585 (2005) 172

Adam Johan Bergren and Marc D. Porter

Abstract

Electroanalytical current measurements are often challenged by sensitivity limitations. For applications requiring enhanced sensitivity, an electrochemical signal can be amplified using a homogeneous electron transfer reaction. This report describes the mechanistic details of a redox recycling amplification system based on monomolecular films of alkanethiolates on gold. These interfaces can be prepared to exhibit facile oxidation of functionalized ferrocenes (FcX), while markedly suppressing the electrolysis of ferrocyanide. Thus, ferrocyanide can be used as a sacrificial electron donor to electrogenerated FcX^+, providing a pathway for a notable improvement of the detection limit for FcX. Electrochemical methods are used to demonstrate, evaluate, and quantify the amplification mechanism. The dependence of amplification on the rates of heterogeneous and homogeneous electron transfer is qualitatively delineated by digital simulations of cyclic voltammetric (CV) curves. This work also develops a mathematical model for prediction of the maximum amplification observed via CV that is tested by comparisons to experimental data. These results are then used as a guide in performance assessments, which yield an optimal amplification of 225 and a limit of detection of ~500 nM.

1. Introduction

Self-assembled alkanethiolate monolayers (SAMs) on gold have been extensively applied in fundamental investigations of heterogeneous electron transfer and in the development of selective electrochemical detectors [1-6]. Many studies have shown that heterogeneous electron transfer rates are attenuated at SAM-modified electrodes relative to unmodified electrodes [5-11]. The extent of rate inhibition depends on the properties of the adlayer (e.g., chemical identity of the end group and length and packing density of the alkyl chain) and the redox species. By adjusting these properties, a balance can be struck which results in a preferential heterogeneous electron transfer for one molecule over another. The resulting system can then be used for redox recycling in which the faradaic current for the analyte is amplified using a regenerating homogeneous electron transfer reaction involving a species that is blocked from undergoing heterogeneous electrolysis by the adlayer.

As recently described by Creager and co-workers, Scheme 1 presents an example of a sensing mechanism which employs redox recycling for amplified detection at a selective interface [12-14]. In this strategy, the SAM strongly restricts the heterogeneous electrolysis of ferrocyanide, $Fe(CN)_6^{4-}$, while allowing the facile oxidation of functionalized ferrocenes (FcX) (e.g., hydroxymethylferrocene, HMF, and 1,1′-ferrocenedimethanol, FDM). After heterogeneous oxidation to FcX^+, a one-electron homogeneous electron transfer from $Fe(CN)_6^{4-}$ converts FcX^+ back to FcX. The repetition of this cycle results in a large amplification of the anodic current for FcX. Creager and co-workers elegantly applied this concept to the ultrasensitive (10^{-8} M) amperometric detection of HMF at SAM-modified gold electrodes in flow injection analysis using $Fe(CN)_6^{4-}$ as the sacrificial species [12-14].

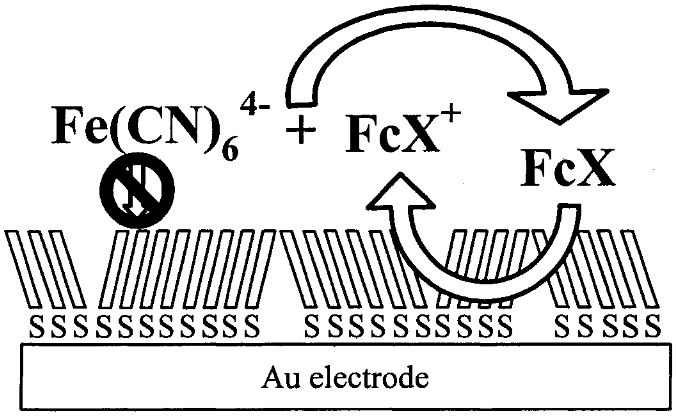

Scheme 1. Schematic representation of the amplification mechanism: electrolysis from $Fe(CN)_6^{4-}$ is blocked, while FcX undergoes rapid oxidation. The oxidized form of the mediator (FcX^+) is reduced by $Fe(CN)_6^{4-}$ back to FcX. This scheme is represented by the E1C′-E_2 electrode mechanism, as outlined in Equations (1-3) in the text (figure adapted from reference [13]).

Redox recycling strategies, such as the one shown in Scheme 1, can be described by a second-order catalytic reaction mechanism that can be envisioned as the inverse of the more frequently used mediation mechanism. Mediation and catalysis schemes are usually applied to facilitate detection of *analyte* molecules which undergo slow heterogeneous electrolysis [15]. The mediator shuttles electrons between the analyte and the electrode, enabling detection of the analyte. In Scheme 1, however, the mediator itself (FcX) *is the analyte*, while the slower couple ($Fe(CN)_6^{4-}$) serves to enhance the oxidation current by recycling FcX^+ to FcX.

We have recently demonstrated that this scheme can be applied using phenyl-modified glassy carbon electrodes [16]. Furthermore, numerous mediation systems are used in bioelectrochemistry [15]. Taken together, the literature underscores the potential merits of this general strategy as a sensitive electroanalytical methodology.

To further explore the range and scope of this detection strategy, we have initiated a series of investigations on the interplay between the rates of heterogeneous and homogeneous electron transfer and the efficiency of the amplification system. In this report, the electrode mechanism is investigated using cyclic voltammetry (CV) and mechanistic digital simulations. $Fe(CN)_6^{4-}$ serves as the sacrificial species, with FDM or HMF as the test analytes, noting that while the majority of the experimental and simulated data reported herein is for FDM, comparable results were obtained for HMF. A mathematical model for the maximum amplification factor in terms of analyte and sacrificial reagent concentrations is derived using established theoretical expressions for the voltammetric anodic peak current ($i_{p,a}$) [17]. The model is then tested by comparisons to experimental findings, and conditions leading to a noted reduction in limits of detection are detailed.

2. Experimental

2.1. Reagents and Chemicals

Distilled water was further purified by deionization with a Millipore Milli-Q water system. Ethanol was purchased from Aaper. Dodecanethiol and ferrocene derivatives were obtained from Aldrich. Sodium chloride, potassium chloride, and isopropanol were supplied by Fisher. Potassium ferrocyanide was acquired from Sigma. All chemicals were used as received.

2.2. Equipment and Methods

Electrochemical measurements were carried out using either an EG&G Princeton Applied Research model 263A potentiostat or a CH Instruments model 600A potentiostat. Freshly prepared electrodes (see below) were used in a three-electrode cell, with a silver/silver chloride, saturated sodium chloride (Ag/AgCl, sat'd NaCl) electrode as a reference (all potentials are reported with respect to this electrode), and a flame-cleaned, coiled platinum wire auxiliary electrode. Solutions were degassed with nitrogen for at least 10 min prior to electrochemical measurements; a blanket of nitrogen was kept over the solution throughout the experiments.

Gold disk electrodes (geometric area: 0.02 cm^2) were purchased from Bioanalytical Systems, Inc. (BAS). These electrodes were polished by hand using a figure-eight pattern on three successively finer grades (1.0, 0.3, and 0.05 μm) of slurried Buehler Micropolish II alumina dispensed on separate Buehler Microcloth pads on a green glass plate. The electrodes were rinsed with deionized water between each grade. Residual alumina was removed by sonication in isopropanol for ~10 min and then deionized water for ~10 min. Electrodes were modified by immersion in 1.0 mM dodecanethiol in ethanol for 20 min, followed by copious rinsing with ethanol and drying in a directed stream of nitrogen.

Dodecanethiolate modified gold electrodes were screened for use in the amplification reaction by cyclic voltammetry in $Fe(CN)_6^{4-}$ and FDM. To ensure that amplified current was due to the homogeneous reaction, only electrodes in CV experiments that gave irreversible waves for $Fe(CN)_6^{4-}$ and showed Nernstian waves for FDM were used. These conditions could be met reproducibly using the procedure outlined above, as indicated by the overlay of current-potential curves for $Fe(CN)_6^{4-}$ to within 10% (sample-to-sample).

2.3. Simulations

Cyclic voltammetric simulations were performed with DigiSim 3.03a software (distributed by BAS). The parameters used in the simulations are given in Table 1 and Figures 3, 4, and 5. Simulated voltammograms that explored the effect of variations in

Table 1. Parameters used in digital simulations.

Reaction	**Parameter**		
Heterogeneous	α	$E^{0\prime}$ (V)	k^0 (cm s^{-1})
$FDM^+ + e^- = FDM$	0.5	+0.265	[a]
$Fe(CN)_6^{3-} + e^- = Fe(CN)_6^{4-}$	0.5	+0.225	2×10^{-7}
Homogeneous			k_a (M^{-1} s^{-1})
$Fe(CN)_6^{4-} + FDM^+ = FDM + Fe(CN)_6^{3-}$			[b]

Parameter	**Value**		***D*** **(cm^2 s^{-1})**
Initial E	-0.15 V[c]	$Fe(CN)_6^{4-}$	6.5×10^{-6}
Vertex	+0.60 V	$Fe(CN)_6^{3-}$	7.6×10^{-6}
Scan Rate	50 mV s^{-1}	FDM	5.4×10^{-6}
C_{dl}	5 μF cm^{-2}	FDM^+	5.4×10^{-6}
A	0.02 cm^2		
R_s	0 Ω		

[a]Set at 0.2 cm s^{-1} in Figure 3, varied in Figure 4; [b]set at 3×10^7 M^{-1} s^{-1} in Figure 4, varied in Figure 3; [c]pre-equilibration enabled (the initial potential is held for 10 s to allow equilibration before initiating the sweep).

electron transfer rates (Figures 3 and 4) employed the simplest possible assumptions: the transfer coefficient (α) for both heterogeneous reactions was set at 0.5; all other variables (i.e., voltage limits, scan rate, capacitance, formal reduction potentials, etc.) were chosen based on experimental parameters or empirically determined values. Simulations used to estimate electron transfer rate constants employed values providing the best fit to experimental data.

3. Results and Discussion

3.1. Electrode Mechanism Description

The overall mechanism in Scheme 1 is characterized by three electron transfer rate constants. It can be generalized as a catalytic second order homogeneous electron transfer step (C′) that follows a heterogeneous electron transfer step (E_1) occurring simultaneously with a second, competing heterogeneous step (E_2). This mechanism is abbreviated E_1C'-E_2 and is described by Equations 1-3:

$$(E_1) \qquad FcX \rightarrow FcX^+ \qquad (k^0{}_1) \qquad (1)$$

$$(C') \qquad Fe(CN)_6{}^{4-} + FcX^+ \rightarrow FcX + Fe(CN)_6{}^{3-} \qquad (k_a) \qquad (2)$$

$$(E_2) \qquad Fe(CN)_6{}^{4-} \rightarrow Fe(CN)_6{}^{3-} \qquad (k^0{}_2) \qquad (3)$$

where $k^0{}_1$ and $k^0{}_2$ are the standard heterogeneous electron transfer rate constants (cm s^{-1}) for E_1 (FcX) and E_2 ($Fe(CN)_6{}^{4-}$), respectively, and k_a is the second order homogeneous electron transfer rate constant (M^{-1} s^{-1}) for C′.

Equations (1) and (2) are coupled through FcX and FcX^+, while Equations (1) and (3) are competitive heterogeneous reactions. The successful application of Scheme 1 requires facile generation of FcX^+, i.e., a large value of $k^0{}_1$. Moreover, effective coupling between E_1 and C′ demands fast electron transfer from $Fe(CN)_6{}^{4-}$ to FcX^+, gauged by a large value for k_a. The efficiency of Scheme 1 in lowering the detection limit for FcX depends on E_2 in two respects. First, the direct electrolysis of $Fe(CN)_6{}^{4-}$ at the electrode raises the background current. Second, it also decreases the amount of $Fe(CN)_6{}^{4-}$ available for regeneration of FcX. Both cases dictate that $k^0{}_2$ be minimized in order to optimally exploit the amplification process in the C′ step.

3.2. The Selective Interface for Amplification

To maximize amplification efficiency, electrodes that exhibit a reversible electron transfer for FDM and irreversible electron transfer for $Fe(CN)_6{}^{4-}$ were used. Figure 1 illustrates the selectivity of the SAM-modified electrode by comparison to an uncoated electrode. The voltammograms have been background subtracted and concentration normalized to facilitate direct comparisons that would otherwise be obscured by the

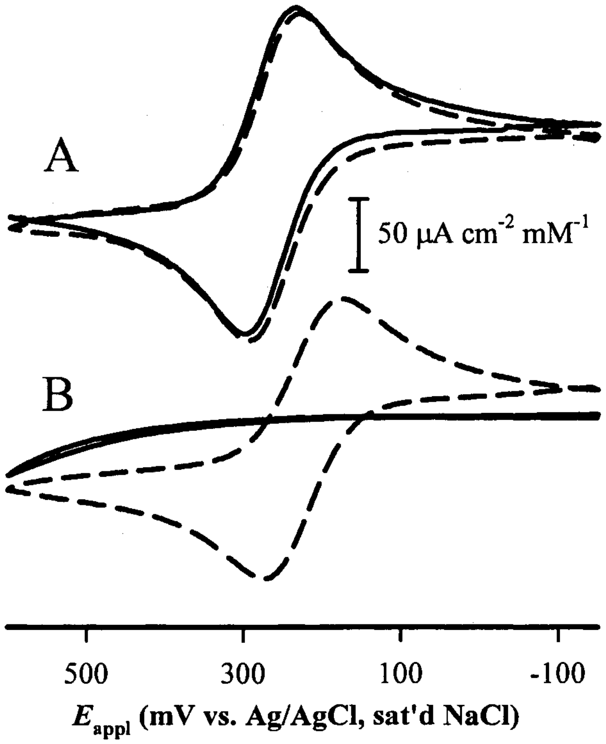

Figure 1. Cyclic voltammograms demonstrating the effect of modifying a gold electrode with dodecanethiolate on the heterogeneous electron-transfer kinetics of (A) 0.2 mM FDM, where ΔE_p is 60 mV for uncoated (- - -) and dodecanethiolate coated (—) Au, and (B) 0.92 mM $Fe(CN)_6^{4-}$, where ΔE_p is 96 mV for uncoated Au (- - -), and i^0 (the current at $E^{0\prime}$) is 1 x 10^{-8} A for dodecanethiolate/Au (—). The CVs are background subtracted and concentration normalized. The geometric electrode area is 0.02 cm^2, the scan rate is 50 mV s^{-1}, and 0.125 M KCl is the supporting electrolyte.

differences in charging current between the uncoated and coated electrodes and the difference in concentrations for FDM and $Fe(CN)_6^{4-}$.

Figure 1A shows that the electrolysis rate of FDM is not measurably affected by electrode modification, as indicated by the overlay of the current-potential (*i-E*) curves at uncoated Au and dodecanethiolate-coated Au. On the other hand, Figure 1B reveals that the rate of $Fe(CN)_6^{4-}$ electrolysis is markedly attenuated, which is demonstrated by the transformation of the shape of the *i-E* curve from one that is diagnostic of a diffusion-limited reaction at uncoated Au to one that exhibits a strong kinetic limitation at the modified electrode. Together, these responses demonstrate the high selectivity that is imparted by the presence of the adlayer, providing the basis for amplification of FDM using $Fe(CN)_6^{4-}$ as a sacrificial reducing agent. Furthermore, an analysis of the *i-E* curves in Figure 1 provides a basis to determine the parameters that characterize the E_1 and E_2 steps, which will serve as input variables for an accurate simulation of the system.

3.2.1. Demonstration of Amplification

Figure 2 shows *i-E* curves that illustrate the amplification of FDM using redox recycling. Note that these voltammograms have not been concentration normalized or background subtracted as in Figure 1. The dotted curve (0.18 mM FDM at dodecanethiolate/Au) shows

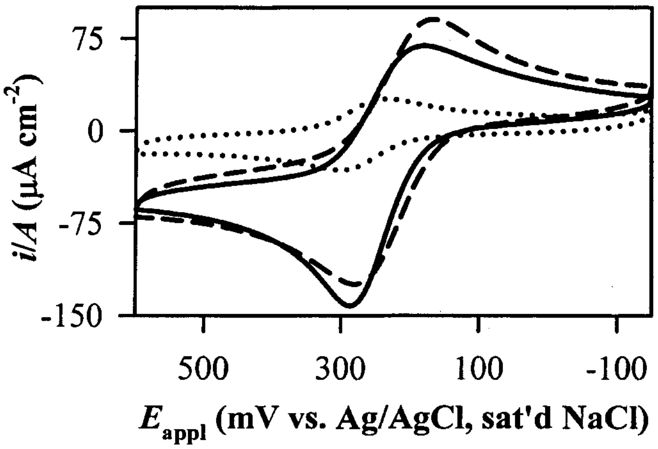

Figure 2. CVs for 0.18 mM FDM (dotted line) and 0.046 mM FDM + 0.88 mM $Fe(CN)_6^{4-}$ (solid line) at a dodecanethiolate modified gold electrode. For comparison, a CV for 0.92 mM $Fe(CN)_6^{4-}$ at uncoated Au is shown (dashed line). See text for details. The electrode area is 0.02 cm^2, the scan rate is 50 mV s^{-1}, and the supporting electrolyte is 0.125 M KCl. Note that the data are not background subtracted or concentration normalized.

the smallest current. The solid curve (0.046 mM FDM with 0.88 mM $Fe(CN)_6^{4-}$) exhibits a much larger current even though the concentration of FDM is almost four times lower.

The total concentration of redox molecules potentially contributing to the current for amplified FDM is 0.93 mM (0.88 mM $Fe(CN)_6^{4-}$ plus 0.046 mM FDM). For comparison, the dashed curve for 0.92 mM $Fe(CN)_6^{4-}$ at uncoated Au is shown. This curve is similar in shape and magnitude to that for amplified FDM (solid curve), demonstrating that the catalytic efficiency of the system is excellent.

3.3. Assessment of Electrochemical Properties

To provide input parameters for digital simulation, several experimental properties of the system are evaluated. The charging current for a dodecanethiolate-modified Au electrode is evaluated at 0.000 V in 0.125 M KCl to provide an estimate for the double layer capacitance (see Table 1). Based on the averages of the anodic and cathodic peak potentials at uncoated gold (dashed lines in Figure 1), the formal reduction potentials for FDM ($E^{0\prime}_1$) and $Fe(CN)_6^{4-}$ ($E^{0\prime}_2$) are +0.265 V and +0.225 V, respectively ($E^{0\prime}$ for HMF is +0.225 V). Values for the diffusion coefficients were estimated using the Randles-Sevcik equation and the cyclic voltammetric peak current [17] at uncoated Au (see Equation (5) below). These values and other important parameters are listed in Table 1. An evaluation of heterogeneous kinetic parameters at dodecanethiolate/Au follows; the E_2 step is evaluated before the E_1 step.

3.3.1. The E_2 Step

The E_2 step is characterized by the irreversible wave shown in Figure 1B (solid curve). The faradaic current at $E^{0\prime}$ (i^0) is related to the standard heterogeneous electron transfer rate constant (k^0) through

$$k^0 = \frac{i^0}{nFAC} \tag{4}$$

where C is the bulk concentration of the redox species, n is the redox stoichiometry, F is the faraday, and A is the electrode area [8]. Equation (4) can be applied when the concentration of the redox couple at the interface has not been significantly reduced from its bulk value, a condition confirmed for $Fe(CN)_6^{4-}$ at dodecanethiolate/Au by the independence of the current with scan rate between 10 and 100 mV s^{-1} [8]. Thus, k^0_2 is evaluated from the current at +0.225 V (0.5 μA cm^{-2}), and gives 5 (±4) x 10^{-6} cm s^{-1}.

The calculated values from the *i-E* curves are higher than those obtained by best-fits of digital simulations, which give ~2 x 10^{-7} cm s^{-1}. This discrepancy arises from the uncertainty involved in the subtraction of the background current to yield the true faradaic current. Thus, to maintain consistency, the value determined from simulations is used when the entire E_1C'-E_2 mechanism is considered. Importantly, all insights derived from these simulations apply for values of k^0_2 less than 10^{-5} cm s^{-1}. An analysis which considers multiple k^0_2 values, which reflect the possible role of structural defects in the adlayer, is underway.

3.3.2. The E_1 Step

The E_1 step, in contrast to the E_2 step, is characteristic of reversible heterogeneous electron transfer. That is, at the highest scan rate employed (100 mV s^{-1}), the peak separation (ΔE_p) remained at 60 mV. The Nicholson equation [18], gives a rate constant of 0.05 cm s^{-1} for ΔE_p values of less than 64 mV for a scan rate of 100 mV s^{-1}. Thus k^0_1 is at least 0.05 cm s^{-1} [19-21].

3.4. Simulation of Amplified CVs

Insights into the contributions of k_a and k^0_1 to the E_1C'-E_2 mechanism were gained by digital simulation (see Table 1) [22]. This strategy draws on earlier reports that examined various EC′ reaction schemes [23-38]. For our simulations, the concentration of $Fe(CN)_6^{4-}$ was maintained at 2 mM. The FDM concentration was 0.2 mM for evaluating of the effect of k_a (Figure 3) and 0.05 mM for assessing variations in k^0_1 (Figure 4).

3.4.1. The Effect of k_a

The effect of the coupling efficiency between E_1 and C′ is illustrated in Figure 3, which presents simulated *i-E* curves for several values of k_a. The value for k^0_1 is maintained at 0.2 cm s^{-1} and that for k^0_2 at 2 x 10^{-7} cm s^{-1}. When k_a is small (solid curve, log k_a = 0), the voltammogram does not show any contribution from the homogeneous reaction. Both heterogeneous processes (E_1 and E_2) occur at overpotentials appropriate for the reaction rate constant and redox molecule concentration. Diffusion limited waves for 0.2 mM FDM appear

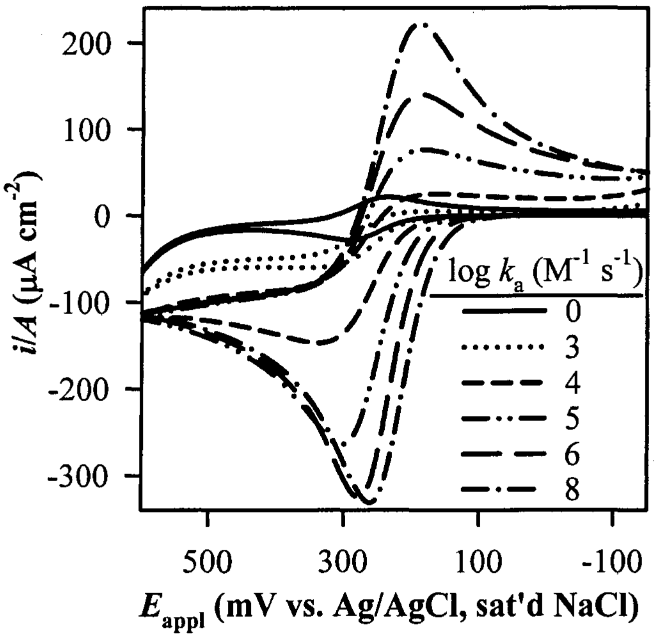

Figure 3. Cyclic voltammetric simulations showing the effect of varying the homogeneous electron transfer rate constant, k_a. The values of k^0_1 (0.2 cm s^{-1}) and k^0_2 (2 x 10^{-7} cm s^{-1}) are held constant. The analytical concentration of FDM is 0.2 mM, and that for $Fe(CN)_6^{4-}$ is 2 mM. All other simulation parameters are given in Table 1.

symmetrically centered about $E^{0\prime}_1$ (+0.265 V). An increase in current at potentials more positive than +500 mV is due to the irreversible electrolysis of 2 mM $Fe(CN)_6^{4-}$.

Increasing k_a by three orders of magnitude results in a change in the *i-E* curve (dotted curve). The current approaches a limiting value before $Fe(CN)_6^{4-}$ oxidation becomes comparatively significant. An increase in the current at potentials greater than +500 mV is still apparent because very little $Fe(CN)_6^{4-}$ was consumed by the amplification reaction.

As k_a is increased further (dashed and dashed-dotted curves), the current increases until a steady state is reached at 10^8 M^{-1} s^{-1} (i.e., larger k_a values do not alter the *i-E* curves). Importantly, the value of k_a required to reach diffusion limited electron transfer with respect to FDM and its coupling with $Fe(CN)_6^{4-}$ is diagnosed by the appearance of a strong peak in the *i-E* curve. Thus, a rough comparison of the *i-E* curve for amplified FDM in Figure 2 (solid curve) with those simulated in Figure 3 indicates that k_a is greater than 10^5 M^{-1} s^{-1}. This value will be refined later.

3.4.2. The Effect of k^0_1

Figure 4 presents simulations in which k_a is large (3 x 10^7 M^{-1} s^{-1}), k^0_2 is small (2 x 10^{-7} cm s^{-1}), and k^0_1 is varied. Values of k^0_1 larger than 2 cm s^{-1} produce *i-E* curves that are identical. As k^0_1 decreases, the anodic peak potential ($E_{p,a}$) begins to shift to more positive values, while the cathodic peak potential ($E_{p,c}$) moves negatively. The increase in ΔE_p arises from a kinetic limitation in the overall mechanism. The limiting value for ΔE_p is 60 mV, as expected for a single heterogeneous electron transfer reaction, and the same expected qualitative trends are observed with respect to the scan rate and k^0_1 [18]. However, the inclusion of a second order homogeneous reaction by the E_1C'-E_2 mechanism requires larger values of k^0_1 to maintain the diffusion limited depletion of both FDM and $Fe(CN)_6^{4-}$. Thus, the peak separation also depends on scan rate, k^0_1, k_a, the concentrations of $Fe(CN)_6^{4-}$ and

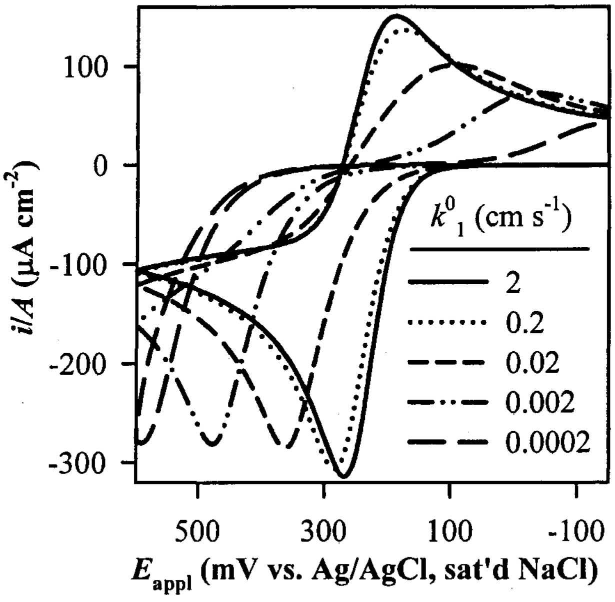

Figure 4. Cyclic voltammetric simulations showing the effect of varying the heterogeneous electron transfer rate constant, k^0_1. The values for k_a (3 x 10^7 M^{-1} s^{-1}) and k^0_2 (2 x 10^{-7} cm s^{-1}) are held constant. The analytical concentration of FDM is 0.05 mM, and that for $Fe(CN)_6^{4-}$ is 2 mM. All other simulation parameters are given in Table 1.

FDM, and $E^{0\prime}_1$ and $E^{0\prime}_2$. A more thorough description of the dependence of the i-E curves on these parameters has been presented for the EC′ mechanism [28]. We find similar qualitative trends for the E_1C'-E_2 mechanism.

Another important feature of the simulations in Figure 4 is the anodic peak current ($i_{p,a}$). Interestingly, $i_{p,a}$ is only marginally affected by a decrease in k^0_1. The origin of this effect can be understood by recognizing that the overpotential required to drive diffusion limited electron transfer becomes larger as k^0_1 decreases. However, if the electrode potential is scanned to a value which converts FDM to FDM$^+$ at a diffusion-limited rate, a large value of k_a leads to the depletion of both FDM and $Fe(CN)_6^{4-}$ at the electrode surface.

3.4.3 Estimation of k_a and k^0_1

Figure 5 shows experimental and simulated *i-E* curves for amplified FDM. Many parameters used in the simulation are fixed by experimental values (see Table 1). The parameters k_a, k^0_1, and the transfer coefficient for E_2 (α_2), were iteratively adjusted until the two curves overlaid (k^0_2 is held constant at 2 x 10^{-7} cm s^{-1}). The best fit values for k_a, k^0_1 and α_2 are 3 x 10^7 M^{-1} s^{-1}, 0.45 cm s^{-1}, and 0.4, respectively. These values are consistent with those reported by others for similar systems [20, 21, 39, 40]. Moreover, the value for k^0_1 is consistent with preliminary determinations using electrochemical impedance spectroscopy in our labs, which will be detailed in a subsequent publication.

Although a range of k^0_1 values can be input into the simulation without changing the shape of the *i-E* curve (see Figure 4), the peak potentials are sensitive to changes in k^0_1

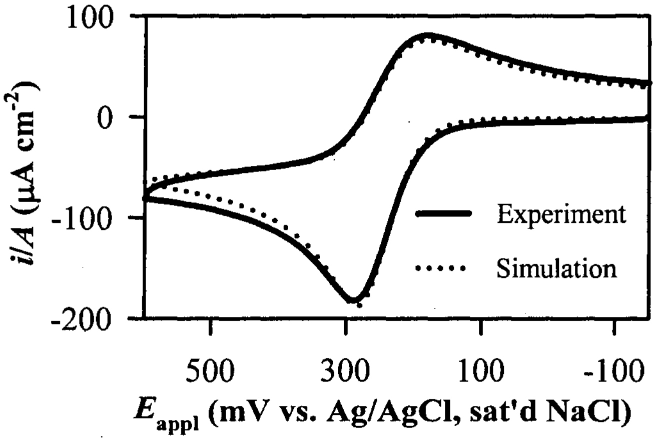

Figure 5. Overlay of experimental and simulated amplification cyclic voltammograms with $k_a = 3 \times 10^7$ M^{-1} s^{-1}, $k^0_1 = 0.45$ cm s^{-1}, and $\alpha_2 = 0.4$. The parameters used to simulate the voltammogram stem from the parameters and conditions used to collect the experimental voltammogram: the concentration of FDM is 0.046 mM, while that for $Fe(CN)_6^{4-}$ is 0.88 mM, the electrode area is 0.02 cm^2 and the scan rate is 50 mV s^{-1} (the supporting electrolyte is 0.125 M KCl). All other simulation parameters are given in Table 1.

between 0.2 and 2 cm s^{-1}. Moreover, the shape of the voltammetric curve is affected by changes in k_a between 10^5 and 10^8 M^{-1} s^{-1} (see Figure 3). The values of $k^0{}_1$ and k_a therefore have an interactive influence on the shape of the curve. The value of $k^0{}_1$ is expected to be sensitive to the fine structure (e.g., defects) of the adlayer. Any contribution of the fine structure proved undetectable due to the rapid rate of the E_1 step. Therefore, simulations like those in Figure 5 were used to estimate the value of k_a by fixing $k^0{}_1$ at 0.45 cm s^{-1}. This analysis, which was applied to fit experiments over a range of conditions (e.g., concentrations of FDM and $Fe(CN)_6{}^{4-}$, scan rate, and several different dodecanethiolate-modified electrodes) gives a k_a value between 5 x 10^6 and 5 x 10^7 M^{-1} s^{-1}. In order to validate and refine this value, theoretical calculations and stopped-flow spectrophotometry were also used to evaluate k_a, and provided confirmation of the values obtained from simulations [41].

3.5. Summary of the E_1C'-E_2 Mechanism

The simulations shown in Figures 3 and 4 illustrate the relative importance of each step in the amplification scheme. If k_a is small, the coupling between E_1 and C′ is low, resulting in poor mediation efficiency. If $k^0{}_1$ is small, a large overpotential is required to create a significant level of FDM^+. However, as long as $k^0{}_1$ is not exceedingly small ($<10^4$ cm s^{-1}), a large anodic peak is observed within an accessible potential window. It should be noted that undesirable levels of background current will flow as a consequence of E_2 if an excessive overpotential is needed. Furthermore, the thiolate coating may be lost through its oxidative desorption at potentials exceeding +0.85 V [42], which would significantly degrade the ability to use redox recycling for amplification.

The qualitative trends observed in our simulations of the E_1C'-E_2 mechanism do not depend strongly on the values of diffusion coefficients (D) of the two couples (e.g., quantities ranging from 10^{-6} to 10^{-5} cm^2 s^{-1} were tested in our simulations). However, D is important when quantitatively matching the simulated and experimental i-E curves. Nevertheless, the values of D used in all simulations were determined experimentally.

Our analysis shows that the values of k^0_1 and k_a are large enough to induce diffusion limited electron transfer for the overall E_1C'-E_2 mechanism at a low overpotential (i.e., within 45 mV) for the E_1 step. Thus, the electron transfer reactions rapidly reach equilibrium. This important result allows the derivation of a predictive model for quantification of the amplification factor using the Randles-Sevcik equation for the anodic cyclic voltammetric peak current.

3.6. Derivation of Amplification Model

The anodic peak current in a CV experiment (i_p) for a reversible one electron oxidation is given by the Randles-Sevcik equation [17]:

$$i_{\mathrm{p,a}} = 2.69 \times 10^5 n^{\frac{3}{2}} A D^{\frac{1}{2}} C \nu^{\frac{1}{2}} \qquad (5)$$

where n is the electron stoichiometry, A is the electrode area, D is the diffusion coefficient, C is the bulk concentration of the redox species, and ν is the scan rate. For the reversible E_1C'-E_2 mechanism, the amplified peak current ($i_{\mathrm{p,amp}}$) can be considered as the sum of the anodic peak currents from both species:

$$i_{\mathrm{p,amp}} = i_{\mathrm{p,1}} + i_{\mathrm{p,2}} \qquad (6)$$

where the subscripts indicate the respective contributions, for example, FDM and $\mathrm{Fe(CN)_6^{4-}}$. An expression for $i_{\mathrm{p,amp}}$ is found by substitution of Equation (5) into Equation (6). This substitution can be simplified by assuming $n_1 = n_2 = n$, and, to a good approximation, $D_1 = D_2 = D$. Thus, the amplified peak current is given by

$$i_{p,a} = 2.69\times10^5 n^{\frac{3}{2}} A D^{\frac{1}{2}} C_T v^{\frac{1}{2}} \quad (7)$$

where $C_T = C_1 + C_2$ (e.g., $C_{FcX} + C_{Fe(CN)_6^{4-}}$).

The maximum amplification factor (AF_{max}) can be defined by the ratio of the amplified peak current to that without amplification, which yields:

$$AF_{max} = \frac{C_T}{C} = \frac{C_{FcX} + C_{Fe(CN)_6^{4-}}}{C_{FcX}} \quad (8)$$

Equation (8) expresses the maximum turnover for any system utilizing a mediation scheme.

A graphical representation of this model is shown in Figure 6, in which the values of AF_{max} are plotted as a function of FDM concentration for three different $Fe(CN)_6^{4-}$ concentrations. The model indicates that as the concentration of FDM decreases (or $Fe(CN)_6^{4-}$ increases), AF_{max} becomes larger. This increase does not imply that the observed peak current exhibits a corresponding augmentation. Instead, the increase in AF_{max} reflects a heightened turnover of FDM^+ back to FDM, as indicated by the decrease in the denominator of Equation (8). For example, the model predicts an infinite amplification factor as the concentration of FDM approaches zero. In reality, as the concentration of FDM decreases

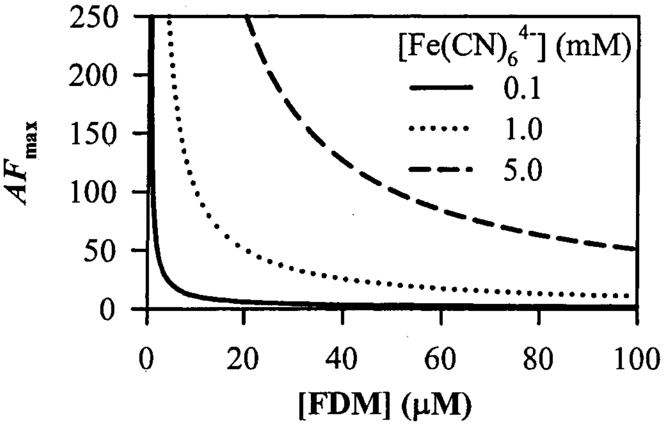

Figure 6. Graphical illustration of AF_{max} versus [FDM] calculated using Equation (8) with the concentration of $Fe(CN)_6^{4-}$ indicated in the legend.

below a critical level, the peak current fails to attain the value predicted by Equation (8).

The limitation of the model arises from loss of 100% mediation efficiency. That is, turnover of FDM^+ must result in the exhaustive consumption of $Fe(CN)_6^{4-}$ in the diffusion layer to obtain AF_{max}. However, by considering the second order rate law for the amplification reaction

$$\frac{-d[\mathrm{FcX}^+]}{dt} = k_a[\mathrm{Fe(CN)_6}^{4-}][\mathrm{FcX}] \qquad (9)$$

where the bracketed terms are the concentrations of indicated species, we can see that the reaction rate cannot be maintained at a sufficient level to exhaustively consume $Fe(CN)_6^{4-}$ if the concentration of FDM falls below a critical value. The lack of a strong peak in the amplified voltammogram is diagnostic of this limitation. For example, strong peaks are exhibited in Figure 7 (see below) when [FDM] is greater than ~10 μM, (solid curve), while the peak is diminished for lower values of [FDM].

3.7. Comparison of Theory and Experiment

The model is tested by measuring $i_{p,a}$ for FDM with and without the presence of ferrocyanide (the average value is 130 (±10) $\mu A\ cm^{-2}\ mM^{-1}$ without ferrocyanide when the sweep rate is 50 $mV \cdot s^{-1}$). The concentrations of $Fe(CN)_6^{4-}$ and FDM employed in these experiments are used to calculate AF_{max}. The experimental amplification factor (AF_{exp}) is defined by:

$$AF_{exp} = \frac{i_{p,a}^*}{i_{p,a}} \qquad (10)$$

where $i_{p,a}$ is the FDM concentration-normalized anodic peak current with only FDM in solution, and $i_{p,a}^*$ is the FDM concentration-normalized amplified anodic peak current (with

$Fe(CN)_6^{4-}$ present). Equation (10) can also be used to calculate a simulated amplification factor (AF_{sim}), where $k^0{}_1$ is maintained at 0.45 cm s^{-1}, and k_a at 3 x 10^7 M^{-1} s^{-1}.

Figure 7A shows amplified experimental *i-E* curves for a series of FDM concentrations ranging between 9.5 μM to 46 μM, with ~0.9 mM $Fe(CN)_6^{4-}$. A plot of the amplification factor versus the concentration of FDM is shown in Figure 7B. When AF_{max} is 50 or less, the values of AF_{exp} and AF_{max} are identical. The values obtained for the simulated amplification

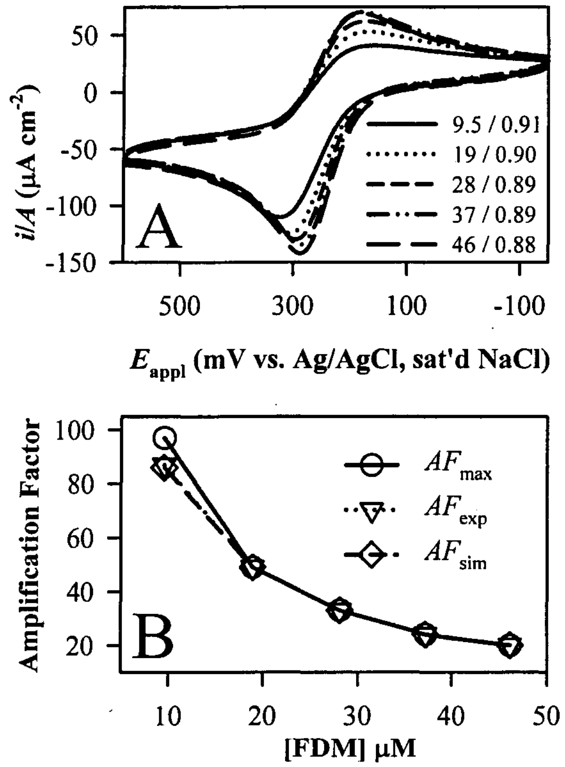

Figure 7. (A) Series of experimental amplification CVs. The concentrations are given as [FDM] in μM / [$Fe(CN)_6^{4-}$] in mM. The scan rate is 50 mV s^{-1}, the electrode area is 0.02 cm^2, and the supporting electrolyte is 0.125 M KCl. (B) Comparison AF_{max}, AF_{exp}, and AF_{sim}. AF_{max} is calculated from Equation (8) using the concentrations of FDM and $Fe(CN)_6^{4-}$ given in Figure 7, while AF_{exp} and AF_{sim} are calculated using Equation (10). Simulation parameters are given in Table 1.

factor (AF_{sim}) also match AF_{exp} and AF_{max} in this regime.

A small negative deviation of AF_{sim} and AF_{exp} from AF_{max} is found for the lowest FDM concentration in Figure 7. Figure 8 shows plots of AF vs. [FDM] to illustrate the general applicability of these methods over a much larger range of AF values, and for a higher concentration of $Fe(CN)_6^{4-}$ (~9 mM). Note that higher amplification factors are achieved when higher levels of $Fe(CN)_6^{4-}$ are used. However, as discussed in Section 3.8, the optimal concentration of $Fe(CN)_6^{4-}$ is determined by a compromise between higher turnover and higher background current levels.

When AF_{max} is large, the negative deviation between AF_{max} and AF_{exp} becomes pronounced. Although the value of AF_{sim} provides a better estimate of AF_{exp}, a negative

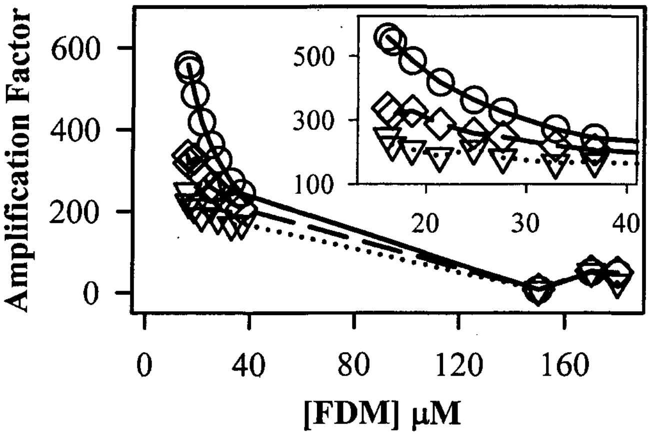

Figure 8. Comparison of AF_{max} (circles, solid line) AF_{exp} (triangles, dotted line) and AF_{sim} (diamonds, dashed line) for a wide range of experiments with $[Fe(CN)_6^{4-}]$ ~9 mM. The deviation of the experimental amplification factor from the maximum is apparent at low FDM concentrations (inset). Simulated amplification factors were calculated by fixing k^0_1 at 0.45 cm s^{-1}, k^0_2 at 2 x 10^{-7} cm s^{-1}, and k_a at 3 x 10^7 M^{-1} s^{-1} and adjusting the concentrations of FDM and $Fe(CN)_6^{4-}$ to the values used in the experiments. Other simulation parameters are given in Table 1.

deviation is also apparent. We suspect that the difference arises from an overestimation of k^0_1 in the simulations. Taken together, Figures 7B and 8 illustrate that a turnover number of ~100 can be reached before the system deviates from the predictions of Equation (8). Furthermore, amplification factors of 200 can be experimentally realized.

3.8. Improvement of the Detection Limit in CV

Without employing redox recycling, the detection limit for FDM by CV at 50 mV s^{-1} is 7 μM at both the bare and modified gold electrode. This limit is defined by the concentration of FDM that yields a faradaic current that is three times larger than the background current. Using the redox recycling mechanism, when $[Fe(CN)_6^{4-}]$ is 9 mM, the detection limit is 500 nM (the detection limit using 0.9 mM $Fe(CN)_6^{4-}$ is about the same). Thus, the detectable quantity of FDM is improved by a factor of fourteen. However, the amplification factor under these conditions is larger than fourteen, indicating a disproportionate relationship between the amplification factor and the enhancement of the detection limit. When [FDM] is ~7 μM, amplification factors between 100 and 225 are realized (see Figures 7 and 8). Nevertheless, the experimentally determined amplified detection limit is ~500 nM, which is much higher than projected based on the amplification factor.

The origin of this disparity lies in the background processes. When $Fe(CN)_6^{4-}$ is absent, the detection of FDM is ultimately limited by the double layer charging current. However, when employing redox recycling, $Fe(CN)_6^{4-}$ is present, resulting in faradaic current from E_2 superimposed on charging current, and gives rise to an increase in the total background current. The improvement in detection limit is therefore given by the amplification factor as modulated by the increase in background current.

4. Conclusions

Electrochemical amplification at selective alkanethiolate modified gold electrodes can be used to increase the number of electrons transferred for each analyte molecule through a sacrificial homogeneous electron transfer reaction. Furthermore, this system can be used to notably improve the detection limit, and our work presented the influence of a range of kinetic factors with respect to the overall amplification mechanism.

The next step in assessing this system involves an analysis of selectivity. This analysis includes a detailed assessment of how variations in $k^0{}_2$, along with the relative concentrations of FDM and $Fe(CN)_6{}^{4-}$ affect sensitivity. Furthermore, variation of the formal reduction potentials of the mediator (FcX) and substrate ($Fe(CN)_6{}^{4-}$) would delineate the role of the thermodynamic driving force for the homogeneous electron transfer, potentially extending the relevance of this work to other intriguing systems. Another important consideration is an analysis of the physical origins of selectivity (i.e., size/shape, hydrophobicity, inherent kinetics, etc.). This work, which will also begin to identify other candidate analyte and sacrificial species, is underway.

5. Acknowledgements

This work was supported, in part, by Eastman Chemical. A. J. B. gratefully acknowledges a Proctor and Gamble Fellowship. Special thanks to Mike Vasbinder and James Espenson for expert assistance with the stopped-flow measurements. Insightful conversations with Grant Edwards, Jeremy Driskell, and Erik J. Cox are also acknowledged. The Ames Laboratory is operated for the US Department of Energy by Iowa State University under Contract no. W-7405-eng-82.

6. References

[1] C.-J. Zhong and M. D. Porter, Anal. Chem. 67 (1995) 709A.

[2] R. W. Murray, "Molecular Design of Electrodes Surfaces" in Techniques of Chemistry, J. William H. Saunders and A. Weissberger, eds., Vol. 22, John Wiley & Sons, Inc., New York, 1992.

[3] A. Ulman, An Introduction to Ultrathin Organic Films From Langmuir-Blodgett to Self-Assembly, Academic Press, San Diego, CA, 1991.

[4] A. Ulman, Chem. Rev. 96 (1996) 1533.

[5] H. O. Finklea, "Electroanalytical Methods: Self-Assembled Monolayers on Electrodes" in Encyclopedia of Analytical Chemistry, R. A. Meyers, ed. Vol. 11, John Wiley & Sons, Ltd, Chichester, 2000, p. 10090.

[6] H. O. Finklea, "Electrochemistry of Organized Monolayers of Thiols and Related Molecules on Electrodes" in Electroanalytical Chemistry: A Series of Advances, A. J. Bard and I. Rubinstein, eds., Marcel Dekker, Inc., New York, 1996.

[7] M. D. Porter, T. B. Bright, D. L. Allara, and C. E. D. Chidsey, J. Am. Chem. Soc. 109 (1987) 3559.

[8] C. Miller and M. Gratzel, J. Phys. Chem. 95 (1991) 5225.

[9] C. Miller, P. Cuendet, and M. Gratzel, J. Phys. Chem. 95 (1991) 877.

[10] A. M. Becka and C. J. Miller, J. Phys. Chem. 96 (1992) 2657.

[11] A. M. Becka and C. J. Miller, J. Phys. Chem. 97 (1993) 6233.

[12] S. E. Creager and P. T. Radford, J. Electroanal. Chem. 500 (2001) 21.

[13] P. T. Radford, M. French, and S. E. Creager, Anal. Chem. 71 (1999) 5101.

[14] P. T. Radford and S. E. Creager, Anal. Chim. Acta 449 (2001) 199.

[15] P. N. Bartlett, P. Tebbutt, and R. G. Whitaker, Prog. Reaction Kinetics 16 (1991) 55.

[16] H.-G. Hong and M. D. Porter, J. Electroanal. Chem. 578 (2005) 113.

[17] A. J. Bard and L. R. Faulkner, Electrochemical Methods: Fundamentals and Applications, John Wiley & Sons, Inc., New York, 2001.

[18] R. S. Nicholson, Anal. Chem. 37 (1965) 1351.

[19] A. M. Bond, T. L. E. Henderson, D. R. Mann, W. Thormann, and C. G. Zoski, Anal. Chem. 60 (1988) 1878.

[20] C. Cannes, F. Kanoufi, and A. J. Bard, J. Electroanal. Chem. 547 (2003) 83.

[21] W. Miao, Z. Ding, and A. J. Bard, J. Phys. Chem. B 106 (2002) 1392.

[22] M. Rudolph, D. P. Reddy, and S. W. Feldberg, Anal. Chem. 66 (1994) 590A.

[23] J. M. Savéant and K. B. Su, J. Electroanal. Chem. 171 (1984) 341.

[24] C. P. Andrieux, J. M. Dumas-Bouchiat, and J. M. Savéant, J. Electroanal. Chem. 87 (1978) 39.

[25] C. P. Andrieux, J. M. Dumas-Bouchiat, and J. M. Savéant, J. Electroanal. Chem. 88 (1978) 43.

[26] C. P. Andrieux, J. M. Dumas-Bouchiat, and J. M. Savéant, J. Electroanal. Chem. 113 (1980) 1.

[27] C. P. Andrieux and J.-M. Savéant, J. Electroanal. Chem. 205 (1986) 43.

[28] D. M. Dimarco, P. A. Forshey, and T. Kuwana, ACS Symposium Series, Chem. Modif. Surf. Catal. Electrocatal., 192, (1982), 71.

[29] C. P. Andrieux and J. M. Savéant, J. Electroanal. Chem. 93 (1978) 163.

[30] C. P. Andrieux, C. Blocman, J. M. Dumas-Bouchiat, F. M'halla, and J. M. Savéant, J. Electroanal. Chem. 113 (1980) 19.

[31] C. P. Andrieux, G. Delgado, J. M. Savéant, and K. B. Su, J. Electroanal. Chem. 348 (1993) 141.

[32] S. U. Pedersen and B. Svensmark, Acta Chemica Scandinavica A A40 (1986) 607.

[33] S. U. Pedersen, Acta Chemica Scandinavica A A41 (1987) 391.

[34] D. H. Evans, J. Phys. Chem. 76 (1972) 1160.

[35] J. F. Rusling and K. Ito, Anal. Chim. Acta 252 (1991) 23.

[36] B. Speiser, Anal. Chim. Acta 243 (1991) 301.

[37] R. S. Nicholson and I. Shain, Anal. Chem. 36 (1964) 706.

[38] J. M. Savéant and K. B. Su, J. Electroanal. Chem. 196 (1985) 1.

[39] J. R. Pladziewicz and J. H. Espenson, J. Am. Chem. Soc. 95 (1973) 56.

[40] S. F. Nelsen, R. F. Ismagilov, K. E. Gentile, M. A. Nagy, H. Q. Tran, Q. Qu, D. T. Halfen, A. L. Odegard, and J. R. Pladziewicz, J. Am. Chem. Soc. 120 (1998) 8230.

[41] See Supplementary Material.

[42] C. A. Widrig, C. Chung, and M. D. Porter, J. Electroanal. Chem. 310 (1991) 335.

7. Supplemental Supporting Information

7.1. Introduction

This material describes the approach used to assess the value of k_a, the homogeneous electron transfer rate constant in the C′ step in the E_1C'-E_2 mechanism used for redox recycling in the amplification strategy. A theoretical assessment based on Marcus theory is used to provide an order-of-magnitude estimate. An experimental determination using stopped flow spectrophotometry was carried out to confirm values determined with cyclic voltammetric simulations.

7.2. Experimental: Stopped-Flow Spectrophotometry

Homogeneous electron-transfer rate constants were measured using an Applied Photophysics DX-17MV stopped-flow spectrophotometer set at a wavelength of 305 nm. 10 μM FDM or HMF was mixed with 20 μM $Fe(CN)_6^{3-}$, and the absorbance at 305 nm followed as a function of time. All solutions were prepared by dilution of 1 mM stocks in 0.125 M KCl. The value of the homogeneous electron transfer rate constants for the reaction between FDM or HMF and $Fe(CN)_6^{3-}$ were determined by fitting the average of eleven trials to the second order rate law [1]. Finally, the homogeneous electron rate constants for the reverse of the measured reactions were determined using the standard procedures detailed in the literature [1]. Electrostatic interactions were not considered in these calculations.

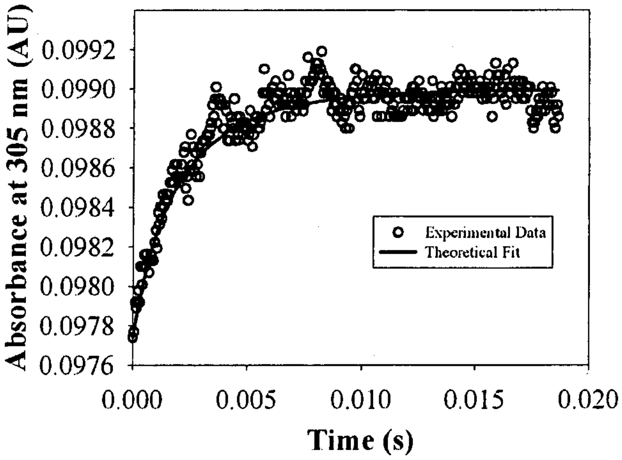

Figure S-1. Experimental determination of k_{12} for FDM and $Fe(CN)_6^{3-}$. The experimental data set is the average of 11 reactions. The value of k_{12} was found to be 3 (±1) x 10^7 M^{-1} s^{-1}. Thus, since K_{eq} is 0.2, k_{-12} (k_a) is 1 (±1) x 10^8 M^{-1} s^{-1}.

7.3. Results and Discussion

7.3.1. Theoretical Calculation of k_a

The values for self-exchange rate constants (k_{se1}) of several ferrocene derivatives are reported to be ~10^7 M^{-1} s^{-1} [2]. The value for $Fe(CN)_6^{4-/3-}$, k_{se2}, is lower, ~10^5 M^{-1} s^{-1} [3]. The homogeneous electron transfer rate constant for the reaction between two redox molecules ($k_{a,m}$) can be calculated from k_{se1} and k_{se2} using the Marcus cross relation

$$k_{a,m} = \left(k_{se1}k_{se2}K_{eq}f\right)^{\frac{1}{2}} \qquad (1\text{-S})$$

where K_{eq} is the equilibrium constant for the cross reaction and f is assumed to be one [4]. The value of K_{eq} is one if the two couples have the same formal reduction potentials (e.g., $Fe(CN)_6^{4-}$ and HMF, where $E^{0\prime}$ is +0.225 V for both). Thus, the theoretically calculated value of $k_{a,m}$ is ~10^6 M^{-1} s^{-1} for the cross reaction between HMF and $Fe(CN)_6^{4-}$.

7.3.2. Stopped-Flow Spectrophotometric Measurement of k_a

The values of k_a were determined for HMF and FDM from the data in Figures S-1 and S-2. The fitted values are 4 (±1) x 10^7 M^{-1} s^{-1} and 1 (±1) x 10^8 M^{-1} s^{-1}, for HMF and FDM, respectively. These results, combined with the results from best fits for the digital simulations in the main body of the paper, place the value of k_a between 5 x 10^6 M^{-1} s^{-1} and 10^8 M^{-1} s^{-1}. The experimentally determined values of k_a are somewhat larger than predicted by theory, and reflects omission of electrostatic interactions in our calculation. The electrostatic work function encountered in the cross reaction of oppositely charged species is predicted to augment the value of k_c [5]. An example of this effect was demonstrated experimentally [6], where values of k_c for the reactions between divalent, anionic functionalized ferrocene derivatives and monovalent, cationic ferrocenium derivatives were found to exceed 10^8 M^{-1} s^{-1}. Thus, considering that the theoretical value of k_a is 10^6 M^{-1} s^{-1} and that it represents the reaction rate between a ferrocenium cation and the highly charged ferrocyanide anion, the experimental values seem quite reasonable.

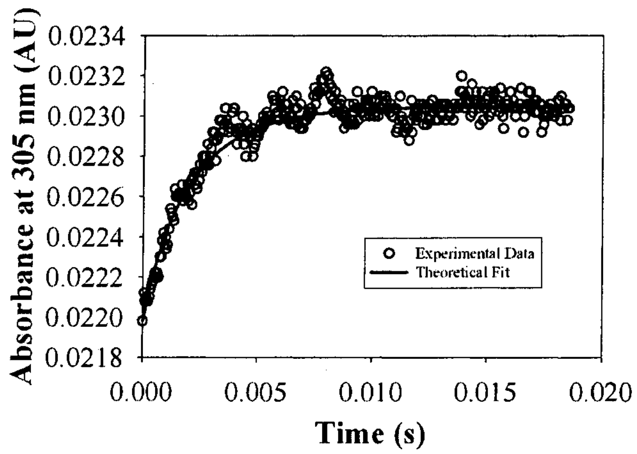

Figure S-2. Experimental determination of k_{12} for HMF and $Fe(CN)_6^{3-}$. The experimental data set is the average of 14 reactions. The value of k_{12} (K_{eq} is one) and k_{-12} was found to be 4 (±1) x 10^7 M^{-1} s^{-1}.

7.4. References

[1] J. H. Espenson, Chemical Kinetics and Reaction Mechanisms, McGraw Hill, New York, 1994.

[2] G. E. McManis, R. M. Nielson, A. Gochev, and M. J. Weaver, J. Am. Chem. Soc. 111 (1989) 5533.

[3] M. Shporer, G. Ron, A. Loewenstein, and G. Navon, Inorg. Chem. 4 (1965) 361.

[4] R. A. Marcus, Electrochim. Acta 13 (1968) 995.

[5] R. A. Marcus, J. Chem. Phys. 24 (1956) 979.

[6] J. R. Pladziewicz and J. H. Espenson, J. Am. Chem. Soc. 95 (1973) 56.

CHAPTER 3. THE CHARACTERISTICS OF SELECTIVE HETEROGENEOUS ELECTRON TRANSFER FOR OPTIMIZATION OF REDOX RECYCLING AMPLIFICATION SYSTEMS

A paper published in *The Journal of Electroanalytical Chemistry* In Press (2006)

Adam Johan Bergren and Marc D. Porter

Abstract

Selective electron transfer reactions provide many opportunities for improving the performance of electrochemical detectors. Self-assembled alkanethiolate monolayers on gold are selective for derivatized ferrocenes (FcX) over ferrocyanide ($Fe(CN)_6^{4-}$). These interfaces enable redox recycling of FcX, a process that regenerates the analyte FcX through a homogeneous electron transfer involving $Fe(CN)_6^{4-}$ as a strongly, but not fully blocked sacrificial electron donor. Although the anodic current for FcX is enhanced using this scheme, the level of background current can also increase due to the low-level electrolysis of $Fe(CN)_6^{4-}$. This work investigates the characteristics of selectivity with respect to heterogeneous electron transfer kinetics and its impact on the limit of detection. To this end, digital simulations are used to construct a kinetic selectivity zone diagram for two redox couples. These zones demonstrate how the differences in the heterogeneous electron transfer rate constants, as expressed by a selectivity ratio, can be exploited to maximize performance. The interplay between various levels of selectivity and amplification is explored, including the effect of the relative concentrations and formal reduction potentials of the two species on the apparent selectivity. A mathematical model is developed to relate the voltammetric sweep rate, applied potential, and concentration and electrolysis rate of the sacrificial species to the

signal to background ratio. These results demonstrate a direct relationship between selectivity and the improvement in the detection limit that can be achieved. Moreover, the two couples should be approximately thermoneutral, the optimal concentration of the sacrificial species is in the low millimolar range, and the applied potential should be as close to the reversible peak potential as possible. In some cases the voltammetric sweep rate can be increased to improve selectivity (and therefore sensitivity). The insights herein provide a basis for further improvements of system performance and enable facile evaluation of prospective amplification systems.

1. Introduction

The performance of electrochemical sensors can be improved by taking advantage of interfacial architectures designed to enhance the rate and/or selectivity of a target heterogeneous electron transfer reaction [1-4]. Analytical measurements based on such strategies benefit from a decrease in the faradaic current from interferences and, in many cases, from a diminution in double layer charging current. These reductions can ultimately improve sensitivity. Moreover, selective electrodes are required for redox recycling schemes, where the signal is amplified using a regenerating homogeneous electron transfer reaction involving a blocked sacrificial species [5-7].

Along these lines, self-assembled alkanethiolate monolayers (SAMs) on gold have been extensively utilized as surface modifiers in the development of selective electrochemical detectors [3, 8-12]. Several studies have shown that heterogeneous electron transfer rates are attenuated at SAM-modified electrodes relative to an unmodified surface [13-19]. Importantly, the extent of rate inhibition can be adjusted by judicious selection of redox couples and modification procedures to yield systems with rapid, preferential heterogeneous electron transfer pathways [5-7]. Alternate strategies for creating selective SAMs have focused on incorporating molecular recognition moieties into the thiol precursor [9-12].

First introduced by Creager and co-workers [5, 6, 20], Scheme 1 presents an example of a redox recycling mechanism for amplified detection at a selective electrode. As shown, derivatized ferrocenes (FcX) undergo rapid oxidation at an alkanethiolate-modified gold electrode that also strongly suppresses the oxidation of $Fe(CN)_6^{4-}$. Electrogenerated FcX^+ is then reduced by $Fe(CN)_6^{4-}$ back to FcX. After homogeneous redox recycling, regenerated FcX can undergo a subsequent heterogeneous oxidation. Repetition of this cycle leads to a marked increase in the anodic current for FcX.

The redox recycling process in Scheme 1 was used to improve detection limits in amperometry [5, 6] and cyclic voltammetry (CV) [7]. We recently showed that an optimal redox recycling system is characterized by a large homogeneous electron transfer rate constant [7]. However, a molecule that undergoes facile homogeneous electron exchange

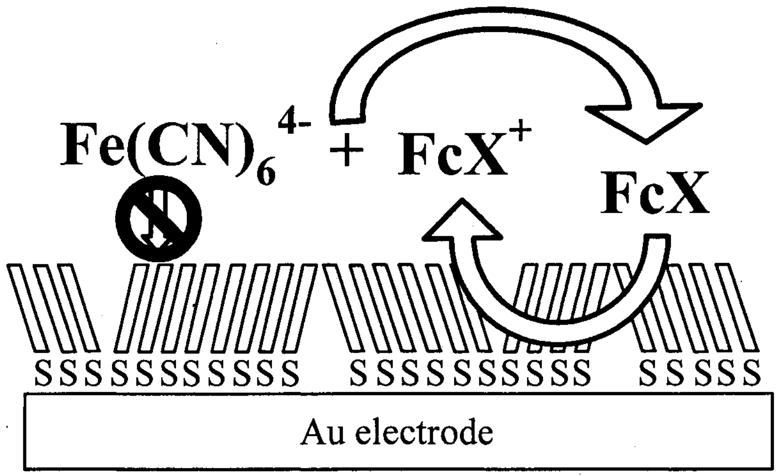

Scheme 1. Schematic representation of redox recycling: oxidation of $Fe(CN)_6^{4-}$ is blocked, while FcX undergoes rapid oxidation. The oxidized form of the mediator (FcX^+) is reduced by $Fe(CN)_6^{4-}$ back to FcX (figure adapted from reference [6]).

(e.g., $Fe(CN)_6^{4-}$ [21, 22]) generally undergoes rapid heterogeneous electrolysis [23]. The addition of the redox-active recycling agent may therefore significantly add to the background current [24-27]. As a consequence, a detailed understanding of the required selectivity with respect to the balance of heterogeneous electron transfer rates of the analyte (e.g., FcX) and sacrificial species (e.g., $Fe(CN)_6^{4-}$) is needed to disentangle the relationship between redox recycling amplification and the resulting improvement in the detection limit.

In a previous report, we examined mechanistic details of the FcX/$Fe(CN)_6^{4-}$ recycling mechanism, focusing primarily on issues central to maximization of amplification in CV experiments. That work also developed a model that predicts the greatest number of recycling events possible in terms of analyte and sacrificial reagent concentrations [7]. Importantly, experimental tests confirmed the modeling predictions. However, the detectable level of FcX was not lowered by a proportional quantity. That is, while each analyte molecule was recycled over 100 times, the detection limit was improved only by a factor of 14. This discrepancy arises from a non-proportional increase in the background current due to the heterogeneous reaction of the sacrificial reagent, and further highlights the need to evaluate the role of selectivity in redox recycling systems.

In this report, varying degrees of selectivity are considered using systematic voltammetric simulations [28]. A kinetic zone diagram [29, 30] for CV with two redox species (no amplification) is constructed. This zone diagram illustrates the relative values of the heterogeneous electron transfer rate constants for two redox molecules that result in various selection regimes. Other factors that have an impact on selectivity and amplification are also investigated, including the relative concentrations of analyte and sacrificial species and their respective formal reduction potentials. The latter effect is further considered with respect to the thermodynamics of the homogeneous recycling reaction.

This work also develops a fundamental understanding of the relationship between selectivity and improved sensitivity for redox recycling schemes. A mathematical model is extended from our previous work to include background current, providing important new insights by calculation of the signal to background ratio as a function of several experimental variables, including the voltammetric sweep rate (ν), applied potential (E_{appl}), and the heterogeneous electron transfer rate constant and concentration of the sacrificial species. Taken together, this work enables facile and comprehensive system optimization. The merits of strategies for further sensitivity improvements are discussed.

2. Experimental Section

2.1. Reagents and Chemicals

Distilled water was further purified by deionization with a Millipore Milli-Q water system. Ethanol was purchased from Aaper. Dodecanethiol and 1,1′-ferrocenedimethanol (FDM) were obtained from Aldrich. Potassium chloride and isopropanol were supplied by Fisher. Potassium ferrocyanide was acquired from Sigma. All chemicals were used as received.

2.2. Electrode Preparation

Gold disk electrodes (geometric area: 0.02 cm^2) were purchased from Bioanalytical Systems, Inc. (BAS). These electrodes were polished by hand using a figure-eight pattern on three successively finer grades (1.0, 0.3, and 0.05 μm) of slurried Buehler Micropolish II alumina that was dispensed on separate Buehler Microcloth pads which were mounted on a green glass plate. The electrodes were rinsed with water between each grade. Residual alumina was removed by sonication in isopropanol for ~10 min and then deionized water for

~10 min. Electrodes were modified by immersion in 1.0 mM dodecanethiol in ethanol for either 20 min or 24 h, followed by copious rinsing with ethanol and drying in a directed stream of nitrogen.

Modified electrodes were screened, following an earlier report [7], in order to verify reversible electron transfer for FDM (i.e., a voltammetric peak separation of ~60 mV) and irreversible electron transfer for $Fe(CN)_6^{4-}$ (i.e., a heterogeneous electron transfer rate constant less than 10^{-5} cm s^{-1}, which is indicated by the lack of voltammetric peaks at potentials less positive than ca. +0.6 V) before amplification experiments were initiated. These metrics ensure the current that is observed when both species are present is due to the mechanism shown in Scheme 1. Using the procedure outlined above, electrodes could be produced in which the reproducibility, as judged by the overlay of current-potential curves for $Fe(CN)_6^{4-}$, was within 10% from electrode-to-electrode.

2.3. Electrochemistry

Electrochemical measurements employed a CH Instruments 600A potentiostat. Freshly prepared working electrodes were used in a three-electrode cell with a silver/silver chloride, saturated sodium chloride reference electrode (Ag/AgCl, sat'd NaCl) and a flame-cleaned, coiled platinum wire auxiliary electrode. Solutions were degassed with high-purity nitrogen for 10 min prior to CV, and a blanket of nitrogen was kept over the solution throughout the experiments.

2.4. Simulations

Current-potential (*i-E*) curves were simulated using DigiSim 3.03a software (distributed by BAS). Global parameters are given in Table 1. The simplest possible assumptions were

Table 1. Parameters used in digital simulations.

Reaction	**Parameter**		
Heterogeneous	α	$E^{0\prime}$ (V)	k^0 (cm s^{-1})
$FcX^+ + e^- = FcX$	0.5	+0.225 [a]	0.2
$Fe(CN)_6^{3-} + e^- = Fe(CN)_6^{4-}$	0.5	+0.225 [a]	2×10^{-8} [b]
Homogeneous		K_{eq}	k_a (M^{-1} s^{-1})
$Fe(CN)_6^{4-} + FcX^+ = FcX + Fe(CN)_6^{3-}$		1 [a,c]	3×10^7 [c]

Parameter	**Value**	**Molecule**	***D*** **(cm^2 s^{-1})**	***C*** **(mM)**
Initial E_{appl}	-0.15 V	$Fe(CN)_6^{4-}$	6.5×10^{-6}	1.0
Vertex E_{appl}	+1.0 V	$Fe(CN)_6^{3-}$	7.6×10^{-6}	0
Scan Rate	50 mV s^{-1}	FcX	5.4×10^{-6}	1.0
C_{dl}	5 μF cm^{-2}	FcX^+	5.4×10^{-6}	0
A	0.02 cm^2			
R_s	0 Ω			

[a] Varied in Figures 5 and 6; [b] S_r was varied by systematically decreasing k^0_2 in Figure 2; [c] when considered.

made: the transfer coefficient (α) for both heterogeneous reactions was set at 0.5; all other variables were chosen based either on experimental settings (i.e., the potential program), empirically determined values (i.e., capacitance, formal reduction potentials, and diffusion coefficients), or were systematically varied (i.e., reaction rate constants, concentrations, etc.) as required for investigation of selectivity and amplification.

3. Results and Discussion

3.1. Selectivity and Background Limitations

The experimental cyclic voltammetric data in Figure 1, as reported previously [6, 7], demonstrate the use of a selective interface for redox amplification. Moreover, these data, obtained at a sweep rate of 50 mV s^{-1}, illustrate the importance of selectivity with respect to background current.

First, a portion of Figure 1A shows *i-E* curves for 0.18 mM FDM at both uncoated Au (solid curve) and dodecanethiolate coated Au (dotted curve) electrodes. The separation of the anodic and cathodic peak-current potentials (ΔE_p) in both curves is ~60 mV, which is indicative of reversible electron transfer for FDM at the uncoated as well as the modified electrode. However, Figure 1B (dashed curve) indicates that the adlayer suppresses the rate for $Fe(CN)_6^{4-}$, noting that a reversible *i-E* curve is obtained for $Fe(CN)_6^{4-}$ at uncoated Au

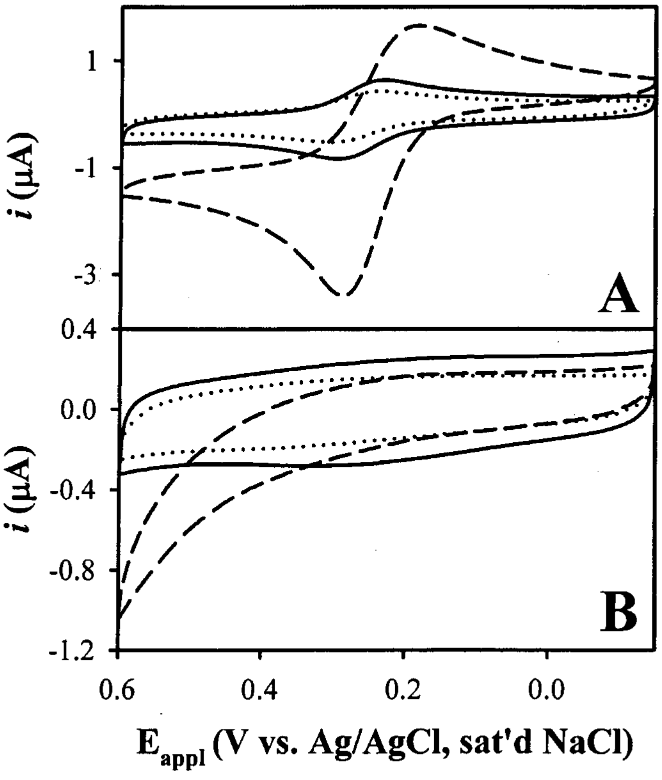

Figure 1. Experimental cyclic voltammetric curves for (A) 0.18 mM FDM at uncoated Au (solid curve) and dodecanethiolate/Au (dotted curve), and 0.046 mM FDM with 0.9 mM $Fe(CN)_6^{4-}$ at dodecanethiolate/Au (dashed curve); and (B) corresponding backgrounds: 0.125 M KCl at uncoated Au (solid curve) and dodecanethiolate/Au (dotted curve), and 0.9 mM $Fe(CN)_6^{4-}$ in 0.125 M KCl at dodecanethiolate/Au (dashed curve). Sweep rate 50 mV s^{-1}, geometric electrode area 0.02 cm^2. The electrode was modified by immersion into an ethanolic solution of dodecanethiol (1.0 mM) for 20 min.

(ΔE_p ~80 mV, data not shown). Taken together, these responses indicate that the dodecanethiolate-coated Au electrode is highly selective for FDM over $Fe(CN)_6^{4-}$.

Figure 1A (dashed curve) also presents a cyclic voltammogram for 0.046 mM FDM with 0.9 mM $Fe(CN)_6^{4-}$ at the same modified electrode. The enhanced current observed for these conditions illustrates amplification of FDM. Importantly, the concentration of FDM is nearly four times smaller for the amplified voltammogram (0.046 mM), which has a much larger anodic peak current relative to that obtained in the absence of $Fe(CN)_6^{4-}$ (0.18 mM FDM, dotted curve). This result typifies the amplification that can be achieved using Scheme 1 [7].

Although these results demonstrate an amplified anodic response, any strategy focused on improvement of the detection limit must also take the level of background current into consideration. Thus, the *i-E* curves of the backgrounds corresponding to each condition in Figure 1A are presented in Figure 1B. Figure 1A shows that the peak current for FDM oxidation appears to decrease upon electrode modification (compare the solid and dotted curves); however, Figure 1B indicates that the background current is reduced by an equal proportion (solid and dotted curves). This comparison illustrates that the magnitudes of the background-corrected peak currents before and after electrode modification are virtually identical, and that the detection capabilities of the two electrodes for FDM are the same.

Figure 1B also shows that while double layer charging is the dominant source of background current in the absence of redox recycling, the low level heterogeneous electrolysis of $Fe(CN)_6^{4-}$ can have a contribution when used to amplify FDM via the homogeneous electron transfer reaction between FDM^+ and $Fe(CN)_6^{4-}$. Furthermore, the faradaic component of the background current increases as the overpotential becomes more positive. These results collectively point to several issues in redox recycling systems that need more extensive examination in order to optimize selectivity and amplification, including the required heterogeneous electron transfer rates for the two reactions and their formal reduction potentials, the concentration of the sacrificial species, and the voltammetric sweep rate.

3.2. Definition of Selectivity in CV

Adapting the IUPAC definition [31], selectivity is defined as the extent to which a target redox species can be detected in the presence of interferences at the same electrochemical interface. For our purposes, the selectivity of a current measurement can be numerically evaluated using the electron transfer selectivity ratio (S_r):

$$S_r = \frac{k_1^0}{k_2^0} \tag{1}$$

where $k^0{}_1$ is the standard heterogeneous electron transfer rate constant for the target couple and $k^0{}_2$ corresponds to that for the sacrificial species, which by nature of the analysis is likely to be the dominant interference.

3.2.1. Simulation of Selectivity

To calculate values of S_r that give rise to differing extents of selectivity, *i-E* curves are simulated for the two heterogeneous oxidation steps in Scheme 1 (E_1 and E_2):

E_1 $$\mathrm{FcX} \rightarrow \mathrm{FcX}^+ + e^- \; (k^0{}_1) \tag{2}$$

E_2 $$\mathrm{Fe(CN)_6}^{4-} \rightarrow \mathrm{Fe(CN)_6}^{3-} + e^- \; (k^0{}_2) \tag{3}$$

This starting point does not include the redox recycling step, which dictates the extent of amplification but not selectivity. We add that while calculations of S_r provide a numerical evaluation of selectivity, $k^0{}_i$ actually corresponds to the concentration normalized rate of heterogeneous electron transfer at the formal reduction potential ($E^{0\prime}$). Thus, the *apparent* selectivity can be influenced by the relative concentrations of the analyte and interfering species, their $E^{0\prime}$ values, as well as many other experimental parameters (e.g., detection mode, sweep rate, and E_{appl}).

3.2.2. Variation of S_r

A representative series of simulated *i-E* curves for a wide range of S_r values are shown in Figure 2. These simulations varied k^0_2 and held k^0_1 at 0.2 cm s^{-1} (other parameters for the simulations are given in Table 1). The value for k^0_1 was chosen to represent the electrochemically reversible reaction that is observed experimentally, noting that numerous

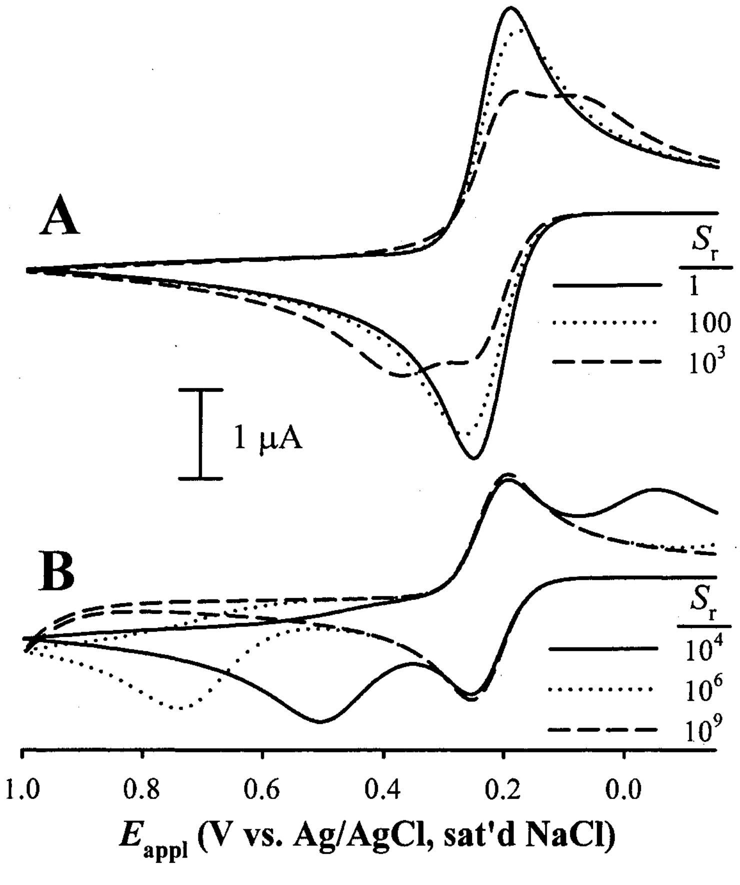

Figure 2. Simulated cyclic voltammetric curves showing how S_r determines the ability to discriminate two similar redox species. These values were generated by changing the value of k^0_2 while maintaining k^0_1 at 0.2 cm s^{-1}. Other parameters are given in Table 1.

simulations were carried out for a wide range of $k^0{}_1$ and $k^0{}_2$ values.

The simulations in Figure 2 show the evolution of the *i-E* curves as S_r increases, yielding several important insights. First, the peak potentials for the E_1 step are maintained at their Nernstian values in each curve. Second, the effective resolution of two separate redox molecules is only possible at large values of S_r. More specifically, when a single voltammetric peak is observed, no selectivity is possible (Figure 2A). This situation occurs when S_r is between one and ~630. The peak current is proportional to the total concentration of the two redox couples, and there are no features in the voltammogram that allow quantification of either species. When S_r is greater than ~630, the *i-E* curve has features that can be definitively attributed to two distinct electron transfer reactions, e.g., the splitting into two anodic waves in Figure 2A (dashed curve).

Larger S_r values augment selectivity (Figure 2B). That is, as S_r increases beyond 1000, the resolution between the two anodic waves increases, and the ability to more effectively discriminate between the two couples improves. For very large values of S_r, the current that flows due to oxidation of $Fe(CN)_6{}^{4-}$ can only be detected at extreme anodic overpotentials (Figure 2B, dashed curve).

3.2.3. Selectivity Zone Diagram

By carrying out numerous simulations for this system, a "kinetic selectivity zone diagram" [29, 30] was constructed by determining the values of $k^0{}_1$ and $k^0{}_2$, and thus S_r, which produce *i-E* curves with common characteristics. An example of this concept is shown in Figure 3 for a sweep rate of 50 mV s^{-1}.

Zone Definition. To define each zone, a plethora of simulations were carried out in which both $k^0{}_1$ and $k^0{}_2$ were systematically varied. When only a single anodic peak was observed, the conditions were assigned to the "no selectivity" sector. The values of $k^0{}_1$ and

$k^0{}_2$ that gave a minimum S_r, and that produced a split in the anodic wave two detectable current minima were allocated to the "intermediate selectivity" zone. Finally, "total selectivity" was defined by baseline resolved anodic waves (see Appendix A).

The zone diagram that results from determining the boundaries of regions that meet the criteria outlined above is shown in Figure 3. To further cultivate understanding of the zone diagram, two other intriguing features should be noted: the "no selectivity observable" zone and the "inverse selectivity" region. Moreover, it should be recognized that the overall appearance of the zone diagram (i.e., the locations of the boundaries) depends on the voltammetric sweep rate.

No Selectivity Observable. The horizontal line that defines the lower boundary of the

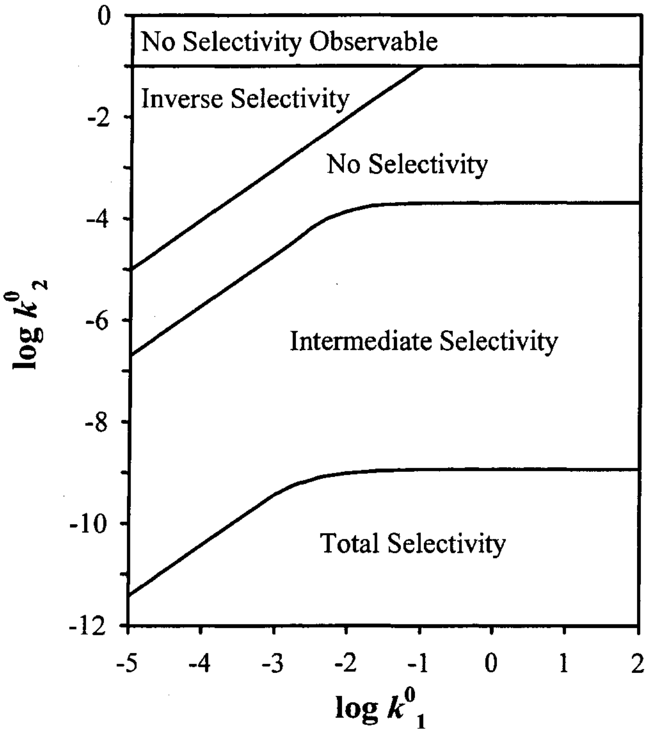

Figure 3. Selectivity kinetic zone diagram for cyclic voltammetry at a sweep rate of 50 mV s^{-1}.

"no selectivity observable" zone demarcates an electrochemically reversible value of k^0_2. At 50 mV s^{-1}, any value of k^0_2 larger than 0.1 cm s^{-1} will yield an anodic peak for E_2 step with a position independent of further increases in k^0_2. Thus, even an infinitely large value of S_r will not yield a measurable level of selectivity. Furthermore, the value of k^0_2 that defines the lower boundary of this region will increase with the voltammetric sweep rate. This result indicates that scan rate can be used in some instances to generate or augment selectivity. We will return to this interesting point shortly.

Inverse Selectivity. Inverse selectivity represents S_r values less than one (i.e., the E_2 reaction is more facile than the E_1 reaction). This region is of no value to the amplification process since k^0_1 must be greater than k^0_2. In a system being evaluated for use in a redox recycling scheme, only the couple with the slower heterogeneous electrolysis rate can potentially serve as the sacrificial species.

Zone Boundary Shapes. The boundaries between the three major selectivity zones roll-off as the value of k^0_1 transitions from irreversible ($< 10^{-3}$ cm s^{-1}) to larger values. Ultimately, for a reversible value of k^0_1 (i.e., larger than 0.1 cm s^{-1} for 50 mV s^{-1}), the slopes of the lines that define the borders are zero. An improvement of resolution at these values of k^0_1 will only be realized by decreases in k^0_2, even when S_r is very large. On the other hand, when k^0_1 is irreversible (i.e., the left side of the zone diagram) the demarcations have slopes of unity. Along this region, the resolution does not depend on the absolute values of k^0_1 and k^0_2, but only on S_r.

The transition between the two limiting situations reflects the E_1 step approaching reversibility via an increase in k^0_1. The shape of this boundary region can be attributed to the dependence of the anodic peak potential ($E_{p,a}$) on k^0_1. That is, $E_{p,a}$ for an irreversible one-electron reaction shifts +120 mV per decade decline in k^0_i [32]. Thus, when both k^0_1 and k^0_2

are less than 10^{-3} cm s^{-1}, both anodic waves shift +120 mV per decade drop in k^0_i, and the value of S_r can be maintained constant with no effect on resolution. However, when k^0_1 is 1 x 10^{-3} cm s^{-1}, the anodic wave for E_1 is only 20 mV positive of the equilibrium peak potential, with a change of two more decades required to reach the limiting potential (giving an average shift of only +10 mV per decade decrease in k^0_1 in this region). In this regime, an increase of S_r with a constant value of k^0_2 provides a marginal improvement in resolution between the two waves.

The reliance of the selection zone boundary shapes on electrochemical reversibility also implies that the sweep rate (ν) can be increased to compensate for mediocre selection in certain instances. The well-known relationship between ν and the values of the peak potentials [29] can be used to understand conditions where this strategy can be exploited. As ν grows, $E_{p,a}$ for an irreversible one electron oxidation shifts positively. On the other hand, a more facile reaction has an $E_{p,a}$ that is invariant until the sweep rate induces a kinetic limitation in the faster reaction.

Recall that when k^0_1 is reversible, the slope of the zone diagram boundary is zero. The effect of increasing ν is to shift this boundary to larger values of k^0_1 and k^0_2 because the rate of the E_1 reaction becomes kinetically limited. This situation then extends the length of the diagonal boundary. This extension of the selectivity zones will result in a relaxed demand on k^0_2 for realizing a given resolution when k^0_1 is large enough to remain reversible as ν increases. Thus, ν should be adjusted such that S_r dictates selectivity and not the apparent reversibility.

The resolution between the two waves will be maximized when ν is increased until $E_{p,a}$ for E_1 begins a positive shift. When this happens, further increases in ν will shift both waves equally, and no further gain in resolution can be achieved. However, as long as E_1 appears reversible, $E_{p,a}$ for E_2 can be shifted positively by increasing v, improving resolution until E_1 is rendered irreversible. Thus, a minimum sweep rate can be defined based on the value of $k^0{}_1$ that will maximize the apparent selectivity. This interesting point will be explored in more detail in Section 3.3.

3.2.4. Other Factors with an Impact on Selectivity

Assessments of S_r provide one perspective on selectivity. However, the relative concentrations and formal reduction potentials of the two redox couples also have critical contributions. Effective amplification requires a sacrificial reagent with a higher solution concentration than the analyte [7]. Moreover, a wide range of $E^{0\prime}$ values are possible for the analyte and sacrificial species. To illustrate the effect of concentration and of offsets in $E^{0\prime}$, *i*-*E* curves were simulated to provide insights into how these parameters effect resolution before the amplification reaction is considered.

The Concentration Ratio. The concentration ratio (C_r) is given by

$$C_r = \frac{C_2^b}{C_1^b} \qquad (4)$$

where $C^b{}_2$ is the bulk concentration of the sacrificial species and $C^b{}_1$ is that for the analyte. Figure 4 shows simulated *i-E* curves for various values of C_r in which S_r equals 10^7 (this approximates our experimental value). When C_r is less than one, selectivity is "enhanced" since less current is generated through E_2 at applied potentials where current is generated for the analyte via E_1. The opposite situation occurs when C_r is greater than one. Note, however, that the wave from E_2 does not overlap with the peak in the analyte wave until C_r is very large. Additional simulations showed that the background current encountered from electrolysis of $Fe(CN)_6^{4-}$ strongly interferes with the detection of the analyte when C_r approaches 10^3.

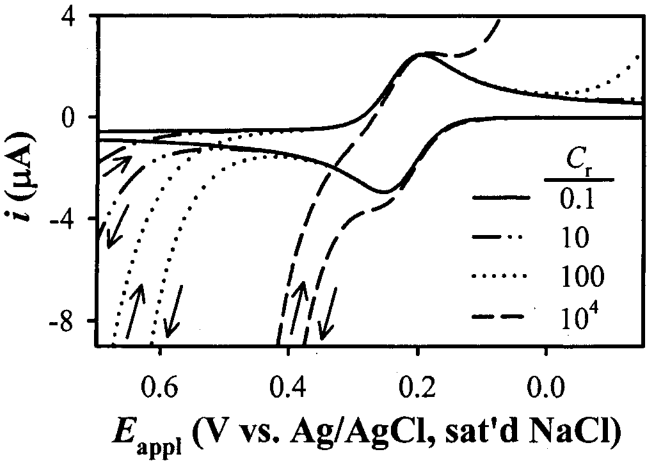

Figure 4. Simulated cyclic voltammetric curves illustrating the effect of C_r on the apparent selectivity. C^{b}_{2} was varied, while C^{b}_{1} was fixed (1 mM), S_r is 10^7 ($k^0_1 = 0.2$ cm s^{-1} and $k^0_2 = 2 \times 10^{-8}$ cm s^{-1}), and other settings are given in Table 1.

The concentration ratio is also an important consideration when designing amplification experiments. Very high C_r values will lead to a higher level of analyte recycling since there would be a large excess of electron donors. As noted earlier, however, the detection capabilities of the system are also intimately linked to the total background current. Thus, the optimal value of C_r cannot be determined by a simple comparison of the apparent selectivity. The effect of sacrificial reagent concentration will be considered in more detail in Section 3.3.

$E^{0\prime}$ Values: No Homogeneous Reaction. So far, we have only considered selectivity between two thermoneutral redox probes. However, there are limitations in the relative values of $E^{0\prime}$ for analyte and sacrificial species. Figure 5 shows simulated i-E curves where S_r is maintained at 10^7 and the values of $E^{0\prime}_1$ and $E^{0\prime}_2$ are varied (other settings are given in Table 1). When $E^{0\prime}_2$ is positive of $E^{0\prime}_1$, selectivity is enhanced (i.e., better peak resolution). On the other hand, when $E^{0\prime}_1$ is made more positive than $E^{0\prime}_2$, a diminution of selectivity is

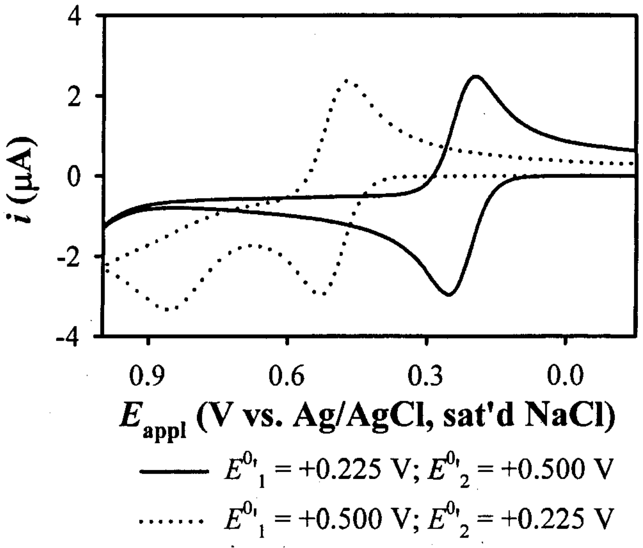

Figure 5. Simulated cyclic voltammetric curves illustrating the effect of offsets in $E^{0\prime}$ for two redox molecules on the voltammetric response are illustrated by simulations where the concentration of FcX and $Fe(CN)_6^{4-}$ were held at 1 mM, S_r is 10^7 (k^0_1 = 0.2 cm s^{-1} and $k^0_2 = 2 \times 10^{-8}$ cm s^{-1}), and the values of $E^{0\prime}$ are varied as indicted in the legend. All other settings are given in Table 1.

observed. However, we cannot conclude that $E^{0\prime}_1$ should be more negative than $E^{0\prime}_2$ without consideration of the impact of the thermodynamics and kinetics of the homogeneous recycling reaction.

$E^{0\prime}$ Values: Thermodynamics and Recycling. For the test system, the homogeneous reaction for redox recycling amplification

$$\mathrm{Fe(CN)_6^{4-}} + \mathrm{FcX^+} \underset{k_{-a}}{\overset{k_a}{\rightleftarrows}} \mathrm{Fe(CN)_6^{3-}} + \mathrm{FcX} \tag{5}$$

is a chemically reversible system, where k_a and k_{-a} are the homogeneous electron transfer rate constants for the forward and reverse reactions (M^{-1} s^{-1}). The equilibrium constant (K_{eq}) for this reaction is related to the reaction rate constants by

$$K_{eq} = \frac{k_a}{k_{-a}} \tag{6}$$

The value of K_{eq} is determined from the respective values of $E^{0\prime}$ for the two couples [29]

$$\ln K_{eq} = \frac{nFE^{0\prime}_{rxn}}{RT} \tag{7}$$

where n is the redox stoichiometry, F is the faraday, R is the gas constant, T is the absolute temperature, and $E^{0\prime}_{rxn}$ is the reaction potential for Equation (5), given by [29]:

$$E^{0\prime}_{rxn} = E^{0\prime}_{FcX} - E^{0\prime}_{Fe(CN)_6^{4-}} \tag{8}$$

Thus, K_{eq} indicates the spontaneous direction of the reaction, and depends on $E^{0\prime}_{rxn}$.

The rate of the forward amplification reaction is governed by the second-order rate law

$$\frac{-d[FcX^+]}{dt} = k_a[Fe(CN)_6^{4-}][FcX^+] \tag{9}$$

where the bracketed terms represent concentrations of the indicated species [33].

In order to illustrate the effect of K_{eq} on amplification, simulated *i-E* curves for various values of K_{eq} (2×10^{-5}, 1, and 5×10^4) were carried out. These values correspond to the following offsets in $E^{0\prime}$ values: when both equal +0.225 V, K_{eq} reflects a thermoneutral reaction and has a value of unity; when $E^{0\prime}_1$ and $E^{0\prime}_2$ are +0.5 V and +0.225 V, respectively, K_{eq} is 2×10^{-5}; and when they are +0.225 V and +0.5 V, respectively, K_{eq} is 5×10^4. The value of S_r is set at 10^7 ($k^0_1 = 0.2$ cm s^{-1}, and $k^0_2 = 2 \times 10^{-8}$ cm s^{-1}), and k_a is 10^7 M^{-1} s^{-1} [7] (other settings are listed in Table 1). Figure 6 shows these curves. Importantly, the anodic peak current is maximized when K_{eq} equals unity.

Large Equilibrium Constant. Perhaps surprisingly, an analysis of Figure 6 reveals that large values of K_{eq} do not enhance the anodic peak current. Instead, the wave becomes split (dotted curve) [32]. The origin of this peak splitting lies in consumption of $Fe(CN)_6^{4-}$ at the electrode surface even when *very small* quantities of FcX^+ are generated, revealed by an assessment of the concentration profiles of FcX and $Fe(CN)_6^{4-}$. The first wave appears as a consequence of the depletion of $Fe(CN)_6^{4-}$ at the reaction plane via the homogeneous electron transfer reaction. However, a significant population of FcX remains in the diffusion layer that can be oxidized as the potential is swept more positive, causing the current to increase until a second maximum is reached. On the reverse scan, a single cathodic wave corresponding to reduction of FcX^+ is observed since k_{-a} is small.

A large value of K_{eq} can also lead to an increase in the background current. To activate amplification, the electrode potential must be sufficiently positive to form FcX^+. However,

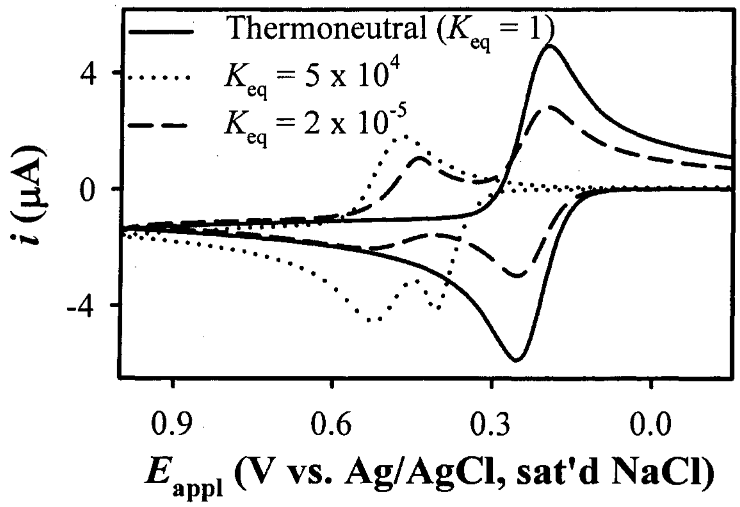

Figure 6. Simulated cyclic voltammetric curves illustrating thermodynamic effects on the *i-E* curves for amplified FcX. S_r is 10^7 (k^0_1 = 0.2 cm s^{-1}, and k^0_2 = 2 x 10^{-8} cm s^{-1}), k_a is 3 x 10^7 M^{-1} s^{-1}, the values of $E^{0\prime}$ are varied to give the value of K_{eq} indicated in the legend (see Table 1 for other settings).

large values of K_{eq} result when $E^{0\prime}{}_1$ is more positive than $E^{0\prime}{}_2$, a situation that increases the background current in the region that current for that analyte flows. This increase is partially counteracted by the large thermodynamic driving force for the amplification reaction, requiring relatively few FcX^+ molecules to generate a signal.

Additional simulations indicate that anodic peak splitting is only apparent when K_{eq} is larger than 62. When K_{eq} is between 1 and ~25, a single broad wave is observed. Intermediate values (26-61) result in a single anodic and cathodic wave, each having shoulders at potentials negative (anodic wave) and positive (cathodic wave) of the larger waves. These values of K_{eq} correspond to offsets in $E^{0\prime}$ (where $\Delta E^{0\prime} = E^{0\prime}{}_1 - E^{0\prime}{}_2$) of 0 to +82 mV, +82 mV to +105 mV, and values larger than +105 mV.

Small Equilibrium Constant. Although large equilibrium constants are not necessarily desirable for optimal implementation of redox recycling, small values are much more limiting. Figure 6 (dashed curve) shows the *i-E* curve when K_{eq} is equal to 2 x 10^{-5}. A single anodic peak is observed at +0.254 V, corresponding to E_1; there is no enhancement of the anodic peak through redox recycling (i.e., the wave is indistinguishable from that which results if $Fe(CN)_6^{4-}$ were absent). The concentration of $Fe(CN)_6^{4-}$ at the surface of the electrode remains near its bulk value. The small wave at more positive potentials reflects the consumption of $Fe(CN)_6^{4-}$ through the homogeneous reaction. However, the back-reaction occurs with such facility that the concentration of $Fe(CN)_6^{4-}$ at the electrode surface does not reach zero. The first cathodic peak obtained upon scan reversal corresponds to the reverse of Equation (5), where all $Fe(CN)_6^{3-}$ that was generated on the forward scan is quickly consumed. Finally, the second cathodic peak is due to reduction of FcX^+.

When K_{eq} is between 0.05 and 1, the voltammetric peaks are slightly broadened relative to a curve for K_{eq} equal to one. When K_{eq} is between 0.01 and 0.05, a shoulder will appear on both peaks, and when K_{eq} is less than 0.05, no enhancement of the current for FcX oxidation is observed (see Figure 6, dashed curve). The values of $\Delta E^{0\prime}$ corresponding to these K_{eq} values are 0 to -76 mV (K_{eq} is 1 to 0.05), and -76 mV to -117 mV (K_{eq} is 0.05 to 0.01). When $\Delta E^{0\prime}$ is less than -117 mV (K_{eq} is less than 0.05), two peaks can be distinguished, and a marked decrease in the magnitude for each is observed.

To summarize the finding so far, redox recycling will be most effective for thermoneutral (or nearly thermoneutral) redox couples. As long as the value of $\Delta E^{0\prime}$ is between -76 and +82 mV, significant current amplification can be achieved. Thus, ferrocene derivatives with $E^{0\prime}$ values between +0.149 and +0.307 V can be amplified using $Fe(CN)_6^{4-}$ ($E^{0\prime}$ = +0.225) at a dodecanethiolate modified gold electrode. However, keep in mind that this system is characterized by k_a and S_r values of ~10^7 M^{-1} s^{-1} and ~10^7, respectively.

When $E^{0\prime}{}_1$ is more positive than $E^{0\prime}{}_2$, the electrode potential must be scanned excessively positive with respect to $E^{0\prime}{}_2$ to oxidize FcX and activate redox recycling. This can lead to large background currents that interfere with current for FcX oxidation. Although less background current results when $E^{0\prime}{}_1$ is more negative than $E^{0\prime}{}_2$, almost no amplification is observed due to the inexorably low value of k_a. In either case, the improvement in detection limit that can be realized will be less than optimal.

3.3. Descriptive Model for Redox Recycling Signal Enhancement

The earlier simulations delineate the required properties for a selective system. However, the successful utilization of redox recycling to lower the detectable level of FcX also requires an improvement in the signal to background ratio (*S*/*B*). To more fully reveal the relationship between selectivity and achievable improvements in the detection limit, we have developed a model based on classical electrochemical constructs that describes the dependence of *S*/*B* on several of the experimental variables central to a redox recycling system.

3.3.1. The Model

Signal. Reversible electron transfer reactions produce the familiar *i*-*E* curve shape that has a faradaic wave superimposed on double layer charging current, where the Randles-Sevcik equation gives the background corrected peak current [29]. We previously showed that an amplified voltammetric peak current ($i_{\mathrm{p,amp}}$) can be calculated from a slightly modified form of the Randles-Sevcik equation

$$i_{\mathrm{p,amp}} = 2.69\times10^{5} n^{\frac{3}{2}} A D^{\frac{1}{2}} C_{\mathrm{T}} \nu^{\frac{1}{2}} \qquad (10)$$

in which n is the electron stoichiometry (and $n = n_1 = n_2$), A is the electrode area, D is the diffusion coefficient (and $D = D_1 = D_2$), C_{T} is the total concentration of FcX and $\mathrm{Fe(CN)_6^{4-}}$, and ν is the sweep rate [7]. Equation (10) gives the maximum analytical current ($i_{\max}$) for an amplification experiment, which, as expected, arises from the exhaustive depletion of both FcX and $\mathrm{Fe(CN)_6^{4-}}$ at the electrode surface.

Background. The background response in an amplification experiment is composed of the current required to charge the double layer (i_{dl}) and the faradaic current from the irreversible heterogeneous oxidation of $\mathrm{Fe(CN)_6^{4-}}$ (i_{ir}). The former is given by

$$i_{\mathrm{dl}} = \nu C_{\mathrm{dl}} A \qquad (11)$$

where ν is the voltammetric sweep rate and C_{dl} is the double layer capacitance [29]. The latter, in contrast, is described by the Butler-Volmer equation

$$i_{\mathrm{ir}} = nFAk_2^0 C_2^{\mathrm{b}} e^{\alpha f (E_{\mathrm{appl}} - E_2^{0\prime})} \qquad (12)$$

where F is the faraday, α is the transfer coefficient, E_{appl} is the applied potential, f is (F/RT), T the absolute temperature, and the other variables were defined previously. The total background current (i_{bg}) in an amplification experiment is therefore the sum of Equations (11) and (12), which yields

$$i_{\mathrm{bg}} = nFAk_2^0 C_2^{\mathrm{b}} e^{\alpha f(E_{\mathrm{appl}} - E_2^{0\prime})} + \nu C_{\mathrm{dl}} A \tag{13}$$

Signal to Background Ratio. The signal to background ratio (S/B) can be written based on Equations (10) and (13) as the ratio of $i_{\mathrm{p,amp}}$ to i_{bg}

$$\frac{S}{B} = \frac{2.69 \times 10^5 n^{\frac{3}{2}} A D^{\frac{1}{2}} C_{\mathrm{T}} \nu^{\frac{1}{2}}}{nFAk_2^0 C_2^{\mathrm{b}} e^{\alpha f(E_{\mathrm{appl}} - E_2^{0\prime})} + \nu C_{\mathrm{dl}} A} \tag{14}$$

By making the following substitutions: $n = 1$ eq mol^{-1}, $D = 5 \times 10^{-6}$ cm^2 s^{-1}, $F = 96485.69$ C eq^{-1}, $\alpha = 0.5$, and $f = 38.92$ V^{-1}, Equation (14) simplifies to

$$\frac{S}{B} = \frac{602 C_{\mathrm{T}} \nu^{\frac{1}{2}}}{k_2^0 C_2^{\mathrm{b}} e^{19.5(E_{\mathrm{appl}} - E_2^{0\prime})} + \nu C_{\mathrm{dl}}} \tag{15}$$

Equation (15) serves as a direct evaluation of S/B as a function of several key experimental variables: C_{T}, k^0_2, C^{b}_2, E_{appl}, and ν. However, note that the model is only valid when E_{appl} is at least 30 mV more positive than $E^{0\prime}_1$, since the appearance of a voltammetric peak current requires this condition. In a redox recycling system composed of FDM as the analyte and $\mathrm{Fe(CN)_6^{4-}}$ as the sacrificial species, the anodic peak is located ~+0.3 V.

Note that the homogeneous recycling reaction results in a decrease in the concentration of $\mathrm{Fe(CN)_6^{4-}}$, which would affect the value of the calculated background current. However, detection of an amplified analyte requires a stable background to be obtained using the concentration of $Fe(CN)_6^{4-}$ intended for use in amplification experiments with no analyte present. Thus, the signal current must arise from an overall increase above the background level, and the depletion effect does not enter into the calculation of meaningful *S*/*B* values. This holds for both voltammetric and amperometric detection modes in which redox recycling has been applied.

To probe the relative importance of the variables that effect *S*/*B*, a series of plots was constructed which are shown in Figure 7. Table 2 summarizes the variables used to construct each plot. Importantly, two different values for the applied potential (E_{appl}) were used to calculate the faradaic component of the background current in this model. First, +0.3 V was chosen based on experimentally observed values for the amplified anodic peak potential using FDM as an analyte. Second, +0.5 V was chosen to illustrate the effect of parameters

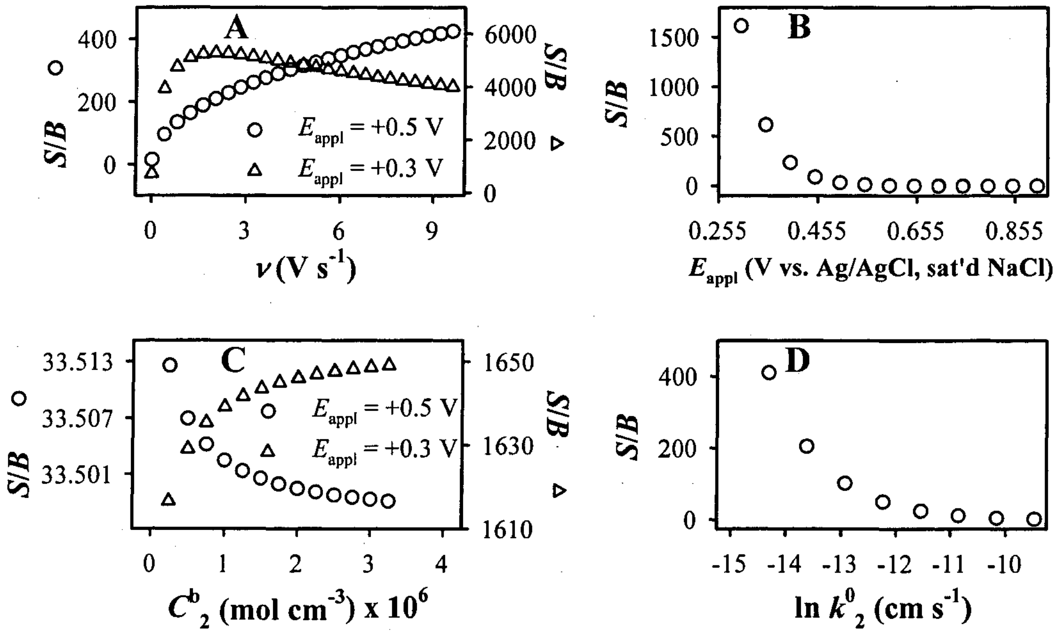

Figure 7. Illustration of the signal to background (*S*/*B*) ratio as a function of: (A) ν (sweep rate) for two values of E_{appl}; (B) E_{appl} (applied potential); (C) C^b_2 (concentration of sacrificial species) for two values of E_{appl}; and (D) k^0_2. See Table 2 for other settings.

that cause a shift of the amplified anodic peak to higher overpotential (e.g., decreases in k^0_1 from electrode modification procedures or increases in sweep rate). The important insights that can be drawn from this model are discussed below.

3.3.2. Variation of the Sweep Rate

Figure 7A shows the effect of sweep rate on S/B for two different values of E_{appl}. Interestingly, a large and continuous increase in S/B with ν is observed when E_{appl} is +0.5 V. This increase in S/B as a function of ν is a consequence of the enhanced selectivity obtained, as discussed in the analysis of the zone diagram (Figure 3) in Section 3.2.3. However, note that the values of k^0_1 and k_a must be large enough to support the increases in ν without resulting in a positive shift of the anodic peak. Moreover, the increase in S/B obtained as ν increases does not result in values that approach the S/B values obtained at even moderate sweep rates when E_{appl} is less positive (see below).

Figure 7A also illustrates that when E_{appl} is +0.3 V, a sharp initial increase, followed by a gradual fall-off is observed for S/B as ν increases. Note that overall, the values of S/B are much larger than obtained when E_{appl} is +0.5 V, but that increasing ν does not lead to continuous gains in S/B. To understand the shape of this curve, we must consider that the diffusion-limited signal peak current grows in proportion to the square root of scan rate.

Table 2. Parameters input into Equation (15) for Figure 7.

Variable	Value	Variable	Value
C^b_1	500 nM	k^0_1	0.45 cm s^{-1}
C^b_2 [a]	0.5 mM	k^0_2 [b]	2 x 10^{-7} cm s^{-1}
C_T	0.5005 mM	S_r	2.8 x 10^5
ν [c]	50 mV s^{-1}	A	0.02 cm^2
C_{dl}	1 μF cm^2 [d]	E_{appl} [e]	+0.300 V
$E^{0\prime}_1$	+0.225 V	$E^{0\prime}_2$	+0.225 V

[a] Varied in Figure 7C; [b] varied in Figure 7D; [c] varied in Figure 7A; [d] see reference [17]; [e] varied in Figure 7B, two separate values considered for 7A and 7C.

However, the background contains a term that grows directly with sweep rate (double-layer charging), and a constant term that depends on E_{appl}. The term that controls the denominator of Equation (15) will determine the behavior of *S*/*B* as ν increases. Thus, when the applied potential is such that double-layer charging is controlling, a continuous decrease in *S*/*B* with ν is expected (as is observed for normal cyclic voltammetry). On the other hand, when the faradaic current controls the background (as expected at more positive values of E_{appl}), larger sweep rates will augment *S*/*B* (although lower overall values of *S*/*B* are obtained). When ν is large enough that the double-layer charging component becomes comparable to the faradaic current term, a mixed case is observed, where an initial increase is followed by a drop off (as in Figure 7A, triangles).

3.3.3. Variation of the Detection Potential

As we have already seen, the value of *S*/*B* is strongly dependent on E_{appl}. The model can be applied to provide insights into optimal detection potentials in voltammetry or amperometry. However, since the derivation included a signal composed of an amplified voltammetric peak, the detection potential must be, at minimum, one that results in diffusion-limited electron transfer. The anodic voltammetric peak for a reversible heterogeneous oxidation reaction is 30 mV more positive than $E^{0\prime}$ [34]. Thus, for the redox reaction considered here (where $E^{0\prime}$ is +0.225 V), we will only consider potentials more positive than +0.255 V.

Figure 7B presents a plot of *S*/*B* versus E_{appl}. Importantly, *S*/*B* is maximized when E_{appl} is as close to the reversible value of the peak potential as possible. This result is due to the constant signal generated for all values of E_{appl} (the numerator of Equation (15) is independent of E_{appl}). However, more positive E_{appl} values result in larger background current values, resulting in a marked decrease in *S*/*B*. Thus, any factor that requires the use of more positive detection potentials (or that shifts the amplified anodic peak to a more positive overpotential) will degrade the detection capabilities.

3.3.4. Variation of the Sacrificial Reagent Concentration

Figure 7C illustrates the effect of the sacrificial reagent concentration on *S*/*B* (where C^b_1 is maintained at 500 nM) at two values of E_{appl}. Two opposing trends are noted: a continuous increase in *S*/*B* with C^b_2 for E_{appl} +0.3 V (triangles), and a constant decrease for E_{appl} +0.5 V (circles). Again, this result indicates that the electrode potential can significantly impact the efficacy of electrochemical amplification in improving detection limits. Moreover, these trends illustrate that a balance exists between the increased turnover provided by larger C^b_2 values and the concurrent background current increase. Importantly, this compromise results in only marginal gains in *S*/*B* when C^b_2 is larger than ~3 mM, and can even decrease performance if E_{appl} is excessively positive.

Special attention should be given to the difference between the *S*/*B* value and the magnitude of the current. That is, smaller currents may give larger *S*/*B* values. Although high concentrations of $\mathrm{Fe(CN)_6}^{4-}$ will result in large analytical currents, the ability to detect a small amount of FcX can be seriously degraded due to the increase in background encountered, resulting in a relatively small value for *S*/*B*. Taken together, the results in Figure 7C illustrate that although a higher turnover of FcX results when increasing C^b_2, the background current will also rise to a level determined in part by E_{appl}. The net result of this balance points to optimal detection potentials close to the reversible potential for the analyte, and sacrificial reagent concentrations in the millimolar range for the test system.

3.3.5. Selectivity and Improvement of the Detection Limit

Figure 7D shows a plot of *S/B* versus ln(k^0_2). As expected, a sharp increase in *S/B* is obtained when ln(k^0_2) is less than -12, noting that ln(k^0_2) for $Fe(CN)_6^{4-}$ at dodecanethiolate/Au is about -14. This trend shows that as long as the overall catalytic electrode mechanism is facile (a condition implicit in the derivation of the model), it is advantageous to decrease the value of k^0_2 as much as possible. Therefore, the electron transfer selectivity ratio (S_r) is the best indicator of the inherent improvement in detection limit that can be obtained using redox recycling. The experimentally adjustable variables can be optimized by applying the guidelines provided by the model. For a given electrode, S_r dictates the ultimate value for *S/B* that can be obtained after optimizing v, C^b_2, and E_{appl}.

3.4 Possible Strategies for Refining System Performance

From analysis of Figure 7D, it can be inferred that a better barrier to electron transfer could lead to smaller k^0_2 values, and therefore improve *S/B*. However, the effect of increased barrier efficiency on k^0_1 should also be considered. In an attempt to improve the detection limit, the barrier efficiency was increased by using longer immersion times of the Au electrode in 1 mM dodecanethiol (similar results are obtained for longer chain lengths). However, although the value of k^0_2 decreases, Figure 8 shows that k^0_1 is also diminished as a result of this procedure. A proportional change in the absolute values of k^0_1 and k^0_2 does not improve the value of *S/B* expected, since S_r is identical.

The dependence of amplified voltammograms on decreasing values of k^0_1 was previously demonstrated [7]. These results indicate that the anodic peak shifts to more positive values as k^0_1 falls. Thus, the value of *S/B* would decrease (see Figure 7B) unless the value of k^0_2 could be made to decrease as much or more than k^0_1 (see Figure 7D). Importantly, the barrier efficiency is not what gives improved detection limits through amplification. Instead, the more effective coatings should maximize the value of S_r.

4. Conclusions

Electrochemical amplification schemes that utilize redox recycling at selective interfaces can result in notable improvements in the detection limit. In this report, the interplay between selectivity, amplification, and signal to background improvements was investigated. The kinetic requirements for successful creation of a selective interface that can be used in redox recycling were demonstrated. This analysis showed that the sacrificial species must undergo heterogeneous electrolysis at least 1000 times slower than the analyte. Moreover, an ideal

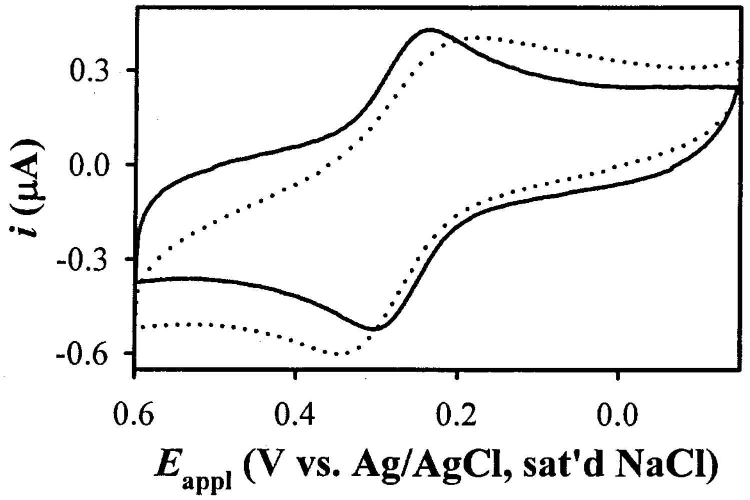

Figure 8. Experimental cyclic voltammetric curves for 0.18 mM FDM in 0.125 M KCl at dodecanethiolate/Au electrodes prepared using a 20 min (solid curve) and 24 h (dotted curve) immersion time. The increased peak separation indicates that the electron transfer rate for FDM is attenuated. The sweep rate was 50 mV s^{-1}, the electrode area was 0.02 cm^2, and the supporting electrolyte was 0.125 M KCl.

amplification system consists of the appropriate oxidation states of two thermoneutral redox couples (i.e., $\Delta E^{0\prime}$ values between -76 and +82 mV) that also undergo rapid homogeneous electron transfer (i.e., characterized by a homogeneous electron transfer rate constant of $>10^6$ $M^{-1}\ s^{-1}$).

These studies also revealed an intimate relationship between selectivity and the ability to improve detection limits. This reliance stems from a balance between signal amplification and background increases. Under certain circumstances, the voltammetric scan rate, electrode potential, and sacrificial reagent concentration can be adjusted to increase the sensitivity. The insights provided by our analysis also extend to detection modes other than voltammetry (i.e., amperometry).

Although the impetus for this work was the amplification system based on Scheme 1 [6], the insights provided here are general, and can be extended to other systems and applied to the evaluation of potential redox recycling systems. Thus, new and potentially superior amplification systems may be found by assessing the parameters that most strongly affect the selectivity. The insights provided by this work enable the evaluation and rational manipulation of those parameters that are most important to a successful redox recycling system. Approaches to extend these concepts to the selective and amplified detection of, for example, neurotransmitters (and possibly other analytes), is underway.

The next step in a quest to provide a complete set of general design guidelines for these systems is an analysis of the physical selectivity mechanism. That is, a molecular level relation of how derivatized ferrocenes undergo rapid electrolysis at the same interface that suppresses oxidation of $Fe(CN)_6^{4-}$. These mechanistic insights may allow a determination of promising strategies for maximizing S_r. For example, interfacial architectures that repel

$Fe(CN)_6^{4-}$ (e.g., anion-functionalized thiolates on gold) may lead to increased S_r values, and enable better sensitivity. This work is underway, and will be presented in a future report.

5. Acknowledgements

This work was supported, in part, by Eastman Chemical. A. J. B. gratefully acknowledges a Proctor and Gamble Fellowship. Insightful conversations with Grant Edwards, Jeremy Driskell, and Erik J. Cox are also acknowledged. The Ames Laboratory is operated for the US Department of Energy by Iowa State University under Contract no. W-7405-eng-82.

Appendix A. Baseline Resolution in Cyclic Voltammetry

In chromatography, resolution is defined as the distance between adjacent peak centers divided by the average width of the peaks, where a value of 1.5 represents baseline resolution [35]. In cyclic voltammetry, the width of a reversible peak is ~400 mV, while that for an irreversible peak is ~500 mV. These widths were determined using the distance between the inflection point potential at the beginning base of the anodic wave and the post-peak potential that gives a current that is ~50% of the peak value (this value approximates the level obtained in the absence of interfering species). Thus, baseline resolution between an irreversible and a reversible voltammetric peak requires their peak potentials to be separated by ≥675 mV, while two irreversible peaks must be separated by ≥750 mV.

6. References

[1] G. Milczarek and A. Ciszewski, Electroanalysis 16 (2004) 1977.

[2] S. Flink, F. C. J. M. van Veggel, and D. N. Reinhoudt, Sensors Update 8 (2001) 3.

[3] N. K. Chaki and K. Vijayamohanan, Biosens. Bioelectron. 17 (2002) 1.

[4] N. R. Stradiotto, H. Yamanaka, and M. V. B. Zanoni, J. Braz. Chem. Soc. 14 (2003) 159.

[5] P. T. Radford and S. E. Creager, Anal. Chim. Acta 449 (2001) 199.

[6] P. T. Radford, M. French, and S. E. Creager, Anal. Chem. 71 (1999) 5101.

[7] A. J. Bergren and M. D. Porter, J. Electroanal. Chem. 585 (2005) 172.

[8] C.-J. Zhong and M. D. Porter, Anal. Chem. 67 (1995) 709A.

[9] A. Arduini, D. Demuru, A. Pochini, and A. Secchi, Chem. Commun. (2005) 645.

[10] M. R. de Jong, J. Huskens, and D. N. Reinhoudt, Chem. Eur. J. 7 (2001) 4164.

[11] M. T. Rojas and A. E. Kaifer, J. Am. Chem. Soc. 117 (1995) 5883.

[12] M. T. Rojas, R. Königer, J. F. Stoddart, and A. E. Kaifer, J. Am. Chem. Soc. 117 (1995) 336.

[13] H. O. Finklea, "Electrochemistry of Organized Monolayers of Thiols and Related Molecules on Electrodes" in Electroanalytical Chemistry: A Series of Advances, A. J. Bard and I. Rubinstein, eds., Marcel Dekker, Inc., New York, 1996.

[14] H. O. Finklea, "Electroanalytical Methods: Self-Assembled Monolayers on Electrodes" in Encyclopedia of Analytical Chemistry, R. A. Meyers, ed. Vol. 11, John Wiley & Sons, Ltd, Chichester, 2000, p. 10090.

[15] C. Miller, P. Cuendet, and M. Gratzel, J. Phys. Chem. 95 (1991) 877.

[16] C. Miller and M. Gratzel, J. Phys. Chem. 95 (1991) 5225.

[17] M. D. Porter, T. B. Bright, D. L. Allara, and C. E. D. Chidsey, J. Am. Chem. Soc. 109 (1987) 3559.

[18] A. M. Becka and C. J. Miller, J. Phys. Chem. 97 (1993) 6233.

[19] A. M. Becka and C. J. Miller, J. Phys. Chem. 96 (1992) 2657.

[20] S. E. Creager and P. T. Radford, J. Electroanal. Chem. 500 (2001) 21.

[21] M. Shporer, G. Ron, A. Loewenstein, and G. Navon, Inorg. Chem. 4 (1965) 361.

[22] M. Shporer, G. Ron, A. Loewenstein, and G. Navon, Inorg. Chem. 4 (1965) 358.

[23] R. A. Marcus, Electrochim. Acta 13 (1968) 995.

[24] P. N. Bartlett, P. Tebbutt, and R. G. Whitaker, Prog. Reaction Kinetics 16 (1991) 55.

[25] D. Zheng, N. Wang, F.-Q. Wang, D. Dong, Y.-G. Li, X.-Q. Yang, L.-H. Guo, and J. Cheng, Anal. Chim. Acta 508 (2004) 225.

[26] L. Coche-Guerente, V. Desprez, J.-P. Diard, and P. Labbe, J. Electroanal. Chem. 470 (1999) 53.

[27] L. Coche-Guerente, V. Desprez, P. Labbe, and J.-P. Diard, J. Electroanal. Chem. 470 (1999) 61.

[28] M. Rudolph, D. P. Reddy, and S. W. Feldberg, Anal. Chem. 66 (1994) 590A.

[29] A. J. Bard and L. R. Faulkner, Electrochemical Methods: Fundamentals and Applications, John Wiley & Sons, Inc., New York, 2001.

[30] J. M. Saveant and E. Vianello, Electrochim. Acta 8 (1963) 905.

[31] J. Vessman, R. I. Stefan, J. F. van Staden, K. Danzer, W. Lindner, D. T. Burns, A. Fajgelj, and H. Muller, Pure Appl. Chem. 73 (2001) 1381.

[32] D. M. Dimarco, P. A. Forshey, and T. Kuwana, Chemically Modified Surfaces in Catalysis and Electrocatalysis, 192, (1982), 71.

[33] J. H. Espenson, Chemical Kinetics and Reaction Mechanisms, McGraw Hill, New York, 1994.

[34] R. S. Nicholson, Anal. Chem. 37 (1965) 1351.

[35] B. L. Karger, L. R. Snyder, and C. Horvath, An Introduction to Separation Science, John Wiley & Sons, Inc., New York, 1973.

CHAPTER 4. SELECTIVITY MECHANISMS AT SELF-ASSEMBLED MONOLAYERS ON GOLD: IMPLICATIONS IN REDOX RECYCLING AMPLIFICATION SYSTEMS

A paper to be submitted for publication

Adam Johan Bergren and Marc D. Porter

Abstract

Redox recycling systems enable improvement of electrochemical detection capabilities. Enhanced sensitivity is achieved through a catalytic electron transfer reaction that employs a sacrificial redox species which recycles the analyte back to its original oxidation state. The success of these schemes is intimately linked to heterogeneous electron transfer selectivity because the sacrificial additive can increase the background current. Earlier work has shown that electrodes with suitable selectivity can be constructed using alkanethiolate monomolecular films on gold, with various ferrocenes (FcX) serving as a model analyte and ferrocyanide ($Fe(CN)_6^{4-}$) acting as the recycling agent. The work herein investigates the origins of the selectivity for this system. This paper therefore investigates different pathways (electron transfer kinetics, size-exclusion, and partitioning) that can lead to suppression of the heterogeneous electrolysis of $Fe(CN)_6^{4-}$, while maintaining that for FcX at a rapid level. Comparisons of experimental data to expectations derived from model assessments of each pathway are used to evaluate the relative importance of each possibility. The properties of several FcX molecules and $Fe(CN)_6^{4-}$ are also examined to provide further insight into the processes that are important in creating a potent redox recycling system. A model for kinetic selection is described that illustrates the importance of inherent electron transfer coupling.

However, the results indicate that partitioning acts to augment kinetic selection for the $FcX/Fe(CN)_6^{4-}$ system, leading to the high selectivity observed experimentally. These results provide guidelines for refining selectivity by a redesign of the interface, which was tested using functionalized thiolate monolayers. Collectively, these experiments result in an improvement of the cyclic voltammetric detection limit from 7 μM at an uncoated electrode to ~50 nM at a carboxylic acid-terminated monolayer.

1. Introduction

Redox recycling can be used to improve the performance of current transducers [1-8]. These strategies enhance sensitivity by inversion of classical electroanalytical mediation. Scheme 1 contrasts mediation and redox recycling. As shown in Scheme 1A, classical mediators enable detection of a redox couple that undergoes slow heterogeneous electrolysis by the assistance of an additive (i.e., M) that shuttles electrons between the analyte and

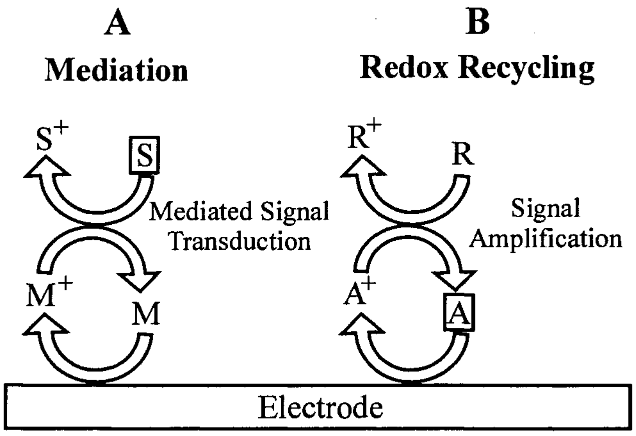

Scheme 1. Idealized models for (A) mediation and (B) redox recycling. In (A), the added mediator, M, acts to transduce a signal from the substrate, S, which is also the analyte. In (B), the signal for the analyte, A, is amplified using a regenerating reagent, R. The analyte is indicated by a box.

electrode such that a signal for S is generated at lower overpotentials [9]. Scheme 1B illustrates redox recycling, where the traditional mediator is now the analyte (A) and the additive is the regenerating agent (R). Although the mechanisms for mediation and redox recycling are effectively equivalent, the inversion of the target species leads to different implementation guidelines for maximizing performance in redox recycling [1, 2].

The major differences in the optimal operational characteristics of mediation and redox recycling stem from the importance of background currents. A mediator should undergo facile heterogeneous and homogeneous electron transfer to generate a signal for the analyte. Moreover, the concentration of S should be much larger than M such that the observed response is controlled by the analyte. In a voltammetric experiment, mediated current can be detected when it is significantly greater than the double layer charging current.

In redox recycling, the regenerating additive should exhibit a rapid rate in the homogeneous reaction that recycles the analyte, but would ideally be devoid of the ability to undergo heterogeneous electron transfer. Importantly, effective amplification requires the concentration of R to be much larger than that for A. The background current in an amplified voltammogram, therefore, can contain a significant contribution from the faradaic current that flows because of direct heterogeneous electrolysis of R which is superimposed on the capacitive current. It is this background current that must be held to an ever lower level in order to improve the detection limit [2].

In order to circumvent the contribution to the background current from the sacrificial agent, an electrode that is strongly preferential toward the electrolysis of the analyte must be employed. It is not surprising then, that the successful application of inverse mediation for redox recycling is linked to the maturation of chemically modified electrodes [3, 4, 10]. We recently demonstrated the existence of an intimate relationship between electrode selectivity

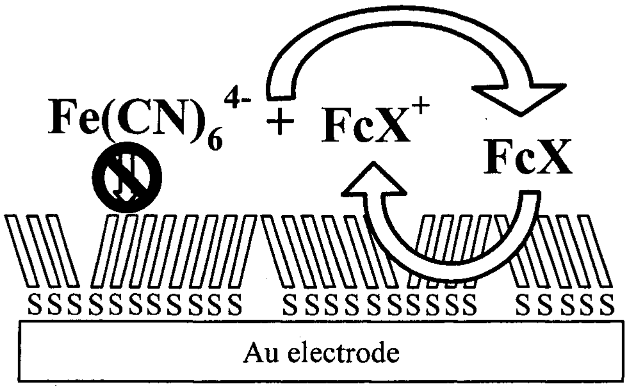

Scheme 2. Schematic representation of the amplification mechanism: electrolysis from $Fe(CN)_6^{4-}$ is suppressed, while FcX undergoes rapid oxidation. The oxidized form of the mediator (FcX^+) is reduced by $Fe(CN)_6^{4-}$ back to FcX (figure adapted from Reference [4]).

and improvements in the detection limit in that the low level electrolysis of the sacrificial species can degrade the enhancement enabled by redox recycling [2].

Scheme 2 presents the redox recycling mechanism that was first introduced by Creager and co-workers [3, 4]. As shown, a self-assembled monolayer, constructed by the chemisorption of dodecanethiol on a gold electrode, provides selection of the analyte over the sacrificial species. In other words, the adlayer allows the rapid oxidation of a ferrocene derivative (FcX) that serves as a model analyte, while suppressing the heterogeneous electrolysis of $Fe(CN)_6^{4-}$, which functions as the sacrificial redox reagent. Electrogenerated ferrocenium then undergoes a homogeneous electron transfer with $Fe(CN)_6^{4-}$ to regenerate the neutral form of the analyte, which can again be oxidized at the electrode. The repetition of this cycle, therefore, defines the enhancement of the anodic current for FcX. This scheme has been successfully demonstrated in amperometric [3, 4] and voltammetric [1, 2] detection platforms in which hydroxymethylferrocene (HMF) and 1,1′-ferrocenedimethanol (FDM) were used as analytes, with $Fe(CN)_6^{4-}$ functioning as the regenerating agent. These reports showed clear improvements in detection limits. For example, the limit of detection for FDM was lowered from 7 μM to 500 nM using cyclic voltammetry [1]. The results also showed that this level of performance was defined by the background current that flows from the electrolysis of $Fe(CN)_6^{4-}$.

The connection between selectivity and improvements in detection limit for this redox recycling scheme has led to guidelines that can be used to evaluate and refine performance [1, 2]. At present, however, these guidelines do not encompass rationalizations based on molecular level details that dictate selectivity. Insights to this end are required to further cultivate performance through the rational design of the interfacial architecture.

The main goals of our earlier work were to delineate the interplay between the rates of heterogeneous and homogeneous electron transfer with respect to selectivity, amplification, and improvements in detection limits [1, 2]. In this paper, mechanisms that may lead to the experimentally observed selectivity are examined. These mechanisms, which in part parallel the electron transfer pathways probed in earlier studies at monolayer modified electrodes [3, 4, 10-31], include kinetic, size-exclusion, and partitioning selectivity. The potential contribution of each possibility for the $FcX/Fe(CN)_6^{4-}$ system is evaluated by analysis of experimental data and comparisons to modeling predictions.

This work also investigates strategies to further improve the detection limit by increasing selectivity through interfacial design refinements that reflected the findings from the physical selectivity mechanism. These experiments were carried out using functionalized (i.e., anionic) alkanethiolate monolayers on gold (i.e., a carboxylic acid terminated adlayer and pH adjustments of the electrolyte). With this alternate design, a limit of detection of ~50 nM is realized with cyclic voltammetry in alkaline solution (pH 11). This level of performance represents a 10-fold improvement over that using a dodecanethiolate coating, and is ~140 times better than that obtained at uncoated gold electrode. These improvements illustrate the ability of the adlayer to repel the highly charged sacrificial reagent while the response of FDM is unaffected (i.e., it is able to partition); the rate of electrolysis for FDM or of the homogeneous recycling reaction is also promoted by the presence of hydroxide anion.

2. Experimental

2.1. Reagents and Chemicals

Distilled water was further purified by deionization with a Millipore Milli-Q water system. Ethanol was purchased from Aaper. Thiols, ferrocenes (see Table 1 for names, structures, and abbreviations), methanol and octanol/water partition coefficient reference compounds (benzene, benzyl alcohol, acetophenone, chlorobenzene, ethylbenzene, propylbenzene, and butylbenzene) were obtained from Aldrich or Eastman Chemical. Sodium chloride, potassium chloride, sodium fluoride, potassium ferricyanide, and isopropanol were supplied by Fisher. Potassium ferrocyanide was acquired from Sigma. All chemicals were used as received.

Table 1. Definitions of ferrocene derivatives 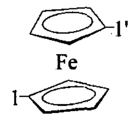 used in this study.

Name	**Abbreviation**	**1**	**1'**
1,1'-Ferrocenedicarboxylic acid	FDA	COOH	COOH
Ferrocenecarboxylic acid	FCA	H	COOH
Ferrocenecarboxaldehyde	FC	H	COH
Acetylferrocene	AF	H	$COCH_3$
Hydroxymethylferrocene	HMF	H	CH_2OH
α-Methylferrocenemethanol	α-MFM	H	CH_3-CHOH
Ferrocene	Fc	H	H
1,1'-Ferrocenedimethanol	FDM	CH_2OH	CH_2OH

2.2. Electrode Preparation

Gold disk electrodes (geometric area: 0.02 cm^2) were purchased from Bioanalytical Systems, Inc. (BAS). These electrodes were polished by hand using a figure-eight pattern on three successively finer grades (1.0, 0.3, and 0.05 μm) of slurried Buehler Micropolish II alumina dispensed on separate Buehler Microcloth pads on a green glass plate. The electrodes were rinsed with deionized water between each grade. Residual alumina was removed by sonication in isopropanol for ~10 min and then deionized water for ~10 min. Electrodes were modified by immersion in 1.0 mM thiol solutions in ethanol for a well-defined time (20 min or 24 h), followed by copious rinsing with ethanol and drying in a directed stream of nitrogen.

2.3. Electrochemistry

Electrochemical measurements were carried out using either an EG&G Princeton Applied Research 263A or CH Instruments 600A potentiostat, a conventional three-electrode cell, a silver/silver chloride, saturated sodium chloride (Ag/AgCl, sat'd NaCl) reference electrode, and a flame-cleaned, coiled platinum wire auxiliary electrode. Solutions were degassed with high-purity nitrogen for at least 10 min prior to electrochemical measurements, and a blanket of nitrogen was kept over the solution throughout the experiments.

2.3.1. Cyclic Voltammetry

Current-potential (*i-E*) curves were used to assess heterogeneous electron transfer rate constants (k^0). Nicholson's method was employed when the cyclic voltammetric peak separation was between 70 and 212 mV [32]; the Butler-Volmer relation was utilized for fully irreversible *i-E* curves:

$$k^0 = \frac{i^0}{nFAC^{\mathrm{b}}} \tag{1}$$

where i^0 is the Faradaic current at the formal reduction potential ($E^{0\prime}$), n is the electron stoichiometry, F is the faraday, A is the electrode area, and C^{b} is the bulk concentration of the redox species [33].

2.4. Chromatography

Octanol/water partition coefficients (K_{ow}) for each of the ferrocenes were estimated via reversed-phase high performance liquid chromatography (RP-HPLC) [34-39]. A Hewlett-Packard Series 1050 HPLC system was employed with an Econosphere C18 column (150 mm length, 3.2 mm inside diameter, 5 μm particle size) as the stationary phase and 70:30 methanol:water as the mobile phase (the pH of the aqueous component was 7). The flow rate was 1.0 mL min^{-1}, the injector loop volume was 5 μL, and UV/vis detection at 211 nm was used to monitor retention. The concentration of the standards and the various ferrocenes were ~1 mM.

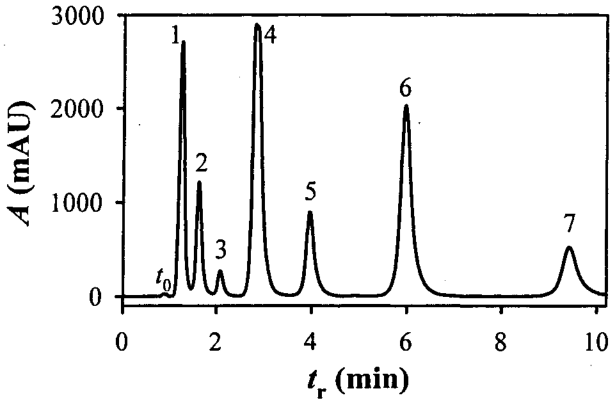

Figure 1. Chromatogram for the seven reference compounds used to determine the values of log(K_{ow}) for the ferrocene derivatives (see Table 1). The order of elution is (1) benzyl alcohol; (2) acetophenone; (3) benzene; (4) chlorobenzene; (5) ethylbenzene; (6) propylbenzene; and (7) butylbenzene.

2.4.1 Partition Coefficient Measurements

In order to determine K_{ow} for the ferrocenes (Table 1), the capacity factor (k') was determined from the retention times of seven reference compounds with known log(K_{ow}) values: benzyl alcohol (1.1), acetophenone (1.7), benzene (2.1), chlorobenzene (2.8), ethylbenzene (3.2), *n*-propylbenzene (4.0), and *n*-butylbenzene (4.6). The values of log(K_{ow}) were taken from literature [40], except for *n*-propylbenzene, which was taken from a separate source [34]. Figure 1 shows a chromatogram of the seven reference compounds; the order of elution is given in the Figure caption.

A calibration plot of log(K_{ow}) vs. log(k') using the reference compounds was constructed, and the equation for the best fit line was determined, as shown in Figure 2. The value of log(K_{ow}) for the ferrocenes was found using the chromatographically determined value of log(k') and the calibration equation. Figure 3 shows the chromatograms collected under the same conditions used to measure the retention of the reference compounds. Three replicate injections of each reference compound and ferrocene derivative gave retention times with a relative standard deviation less than 4%. However, we note that in general, HPLC-based determinations of log(K_{ow}) are accurate to within 0.5 units and are valid for a log(K_{ow}) range

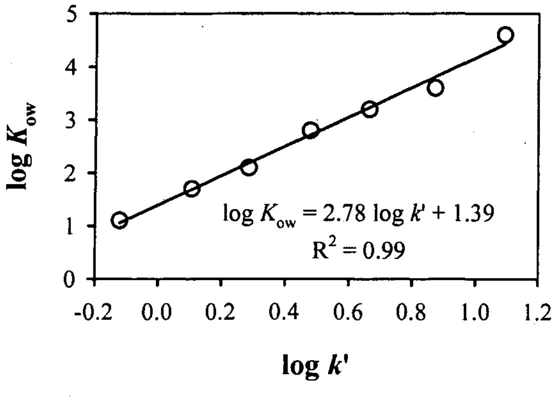

Figure 2. Calibration plot constructed from the data in Figure 1 for the reference compounds used to determine K_{ow} for the ferrocenes.

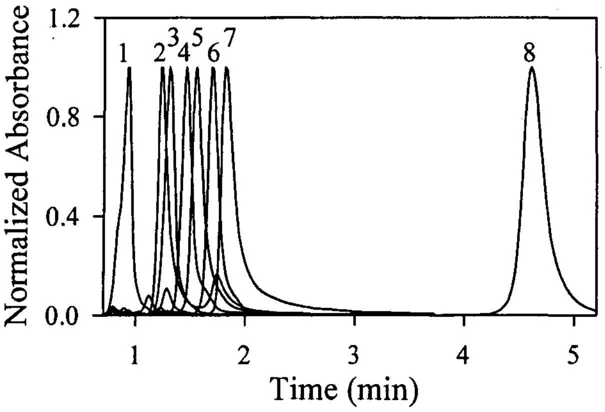

Figure 3. Normalized chromatograms for 8 different ferrocene derivatives. The order of elution is (1) FDA; (2) FDM; (3) FCA; (4) HMF; (5) FC; (6) AF; (7) α-MFM; and (8) Fc (see Table 1 for abbreviation definitions, and Table 2 for calculated $\log(K_{\mathrm{ow}})$ values).

of 1 to 5 [40]. See Table 2 for a list of $\log(K_{\mathrm{ow}})$ values.

Molecular modeling software (ChemDraw Ultra 8.0, Cambridge Soft) was used to assess $\log(K_{\mathrm{ow}})$ for $\mathrm{Fe(CN)_6}^{4-}$ using the chemical properties calculator. Broto's method was employed for this calculation [41].

3. Results and Discussion

3.1. System Description

There are two heterogeneous electron transfer reactions possible in Scheme 2, denoted E_1 and E_2.

$$(\mathrm{E_1}) \qquad \mathrm{FcX} \rightarrow \mathrm{FcX}^{+} + e^{-} \qquad (k^0{}_1) \qquad (2)$$

$$(\mathrm{E_2}) \qquad \mathrm{Fe(CN)_6}^{4-} \rightarrow \mathrm{Fe(CN)_6}^{3-} + e^{-} \qquad (k^0{}_2) \qquad (3)$$

where $k^0{}_1$ is the heterogeneous electron transfer rate constant for the analyte, FcX, and $k^0{}_2$ is that for the sacrificial species, $Fe(CN)_6^{4-}$. The selectivity of an electrode with respect to its ability to discriminate between the two species can be assessed using the heterogeneous electron transfer selectivity ratio (S_r) [2]:

$$S_r = \frac{k_1^0}{k_2^0} \tag{4}$$

S_r indicates the extent to which the electrode selects the analyte over the sacrificial species, which is also a potential interferant; larger values indicate better performance [2].

The amplification reaction, C′, is described by

$$\text{(C}'\text{)} \qquad \mathrm{FcX^+ + Fe(CN)_6^{4-} \rightarrow Fe(CN)_6^{3-} + FcX} \qquad (k_a) \tag{5}$$

where k_a is the homogeneous electron transfer rate constant. The value of k_a must be large ($>10^5$ M^{-1} s^{-1}) in order to realize effective amplification through the E_1C'-E_2 mechanism [1] (i.e., k_a represents the coupling strength between Reactions 2 and 5).

3.2. Experimental Selectivity Results

A series of cyclic voltammetric (CV) current-potential (*i-E*) curves are shown in Figure 4. These curves represent the responses of several ferrocene derivatives (see Table 1) and $Fe(CN)_6^{4-}$ at uncoated Au (dashed curves) and dodecanethiolate-modified Au (solid curves) electrodes. Analysis of these data provides several mechanistic insights.

First, the heterogeneous electron transfer kinetics of all tested ferrocenes are not detectably affected by the presence of the adlayer. The separations of the anodic and cathodic peak potentials (ΔE_p) are ~60 mV for voltammograms A-E. However, as recently reviewed [12], the reaction of $Fe(CN)_6^{4-}$ undergoes a dramatic transformation from a nearly diffusion-limited (ΔE_p ~90 mV) heterogeneous electron transfer at uncoated Au (F, dashed curve) to a

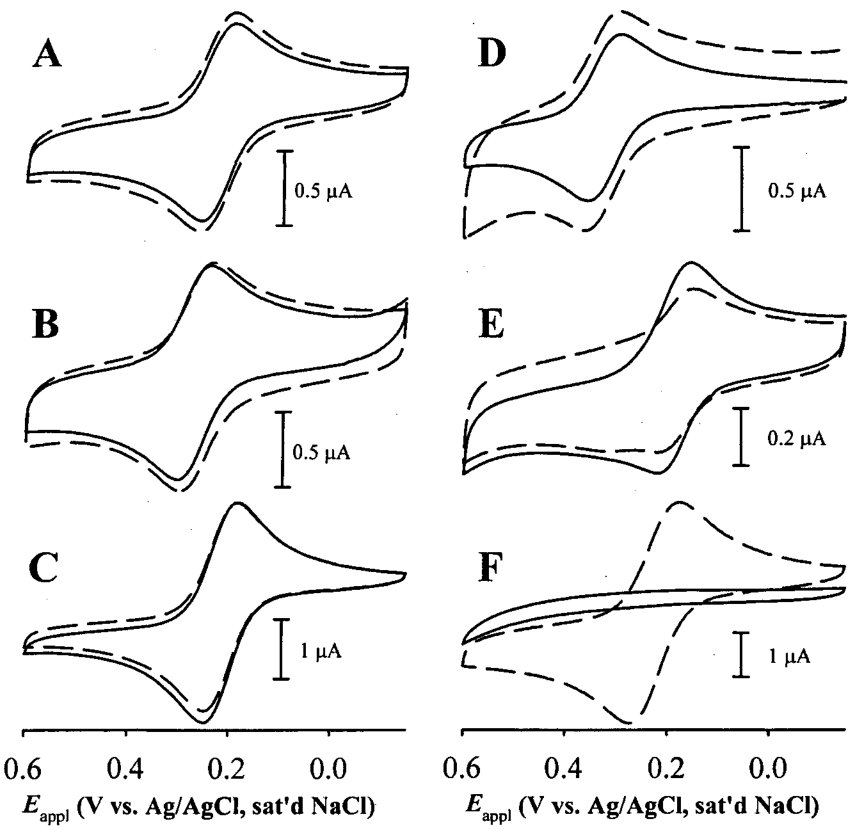

Figure 4. CVs of six different redox molecules at uncoated (dotted curves) and dodecanethiolate-coated (solid curves) gold electrodes: (A) 0.18 mM HMF; (B) 0.17 mM FDM; (C) saturated α-MFM; (D) saturated FCA; (E) saturated Fc; (F) 0.92 mM $Fe(CN)_6^{4-}$. Sweep rate: 50 mV s^{-1}, geometric electrode area: 0.02 cm^2, and supporting electrolyte: 0.125 M KCl.

strongly irreversible reaction at the modified interface (F, solid curve). These results demonstrate the selectivity of the dodecanethiolate monolayer, and provide a basis for current amplification using Scheme 2 [1-4].

A second observation in Figure 4 is the change in interfacial capacitance after coating, indicated by the decrease in current observed for coated (solid curves) relative to uncoated Au (dashed curves). Note that curves C-E were obtained using saturated ferrocene derivative solutions. Due to the low aqueous solubility of these compounds, the concentration of the saturated solutions is $\leq$0.1 mM. As a consequence, the region that is largely devoid of faradaic current shows the change in capacitance more clearly than the rest of the *i-E* curves (especially for C and E). Moreover, *i-E* curves collected when only electrolyte is present (not shown) showed a reduction in the capacitance of ~50%.

Third, there is not a strong dependence of the heterogeneous kinetics on the structure of the ferrocenes; all can therefore potentially serve as an analyte in Scheme 2. This observation is consistent with previous work [23].

Finally, the low-level electrolysis of $Fe(CN)_6^{4-}$ at the dodecanethiolate modified electrode defines the voltammetric background current for amplification. Any strategy that decreases $k^0{}_2$, while maintaining large values for $k^0{}_1$ and k_a would result in better sensitivity. However, lower values of $k^0{}_1$ are counter to amplification because the more positive overpotential required to oxidize FcX [1] would lead to a smaller signal to background ratio [2]. Thus, the development of an optimal amplification scheme reflects an intriguing interplay between several components of the system.

3.3. Possible Selectivity Mechanisms

How then, to account for the selectivity of the dodecanethiolate modified gold electrode for FcX over $Fe(CN)_6^{4-}$? Before turning to an analysis of our data, we briefly review the relevant literature, which will then be coupled with our findings to describe possible selectivity models.

Heterogeneous electron transfer at alkanethiolate modified electrodes may occur through several pathways [27]. First, electrons can tunnel through the adlayer [25]. Second, pinholes in the adlayer can lower the barrier height for electron transfer [12]. Third, the electroactive species can adsorb onto or permeate into the monolayer [11]. All three mechanisms may contribute to varying degrees to the observed current. Selectivity at a modified electrode would arise when there is a disparity in the relative contribution of one or more pathways to the redox transformation of different couples. Overall, three different selectivity mechanisms can be defined: pure kinetic, size-exclusion, and adsorption/partitioning.

The first mechanism does not require any offset in the closest approach of the redox moieties to the electrode, while the later two are pathways that yield a proximity advantage for the analyte. Tunneling can occur at different rates for two redox couples from a reaction plane defined by the full thickness of the adlayer for a pure kinetic mechanism. Size-exclusion and adsorption/partitioning, on the other hand, can reduce the separation between the reaction plane and electrode for one reactant and subsequently enhance its rate of electron transfer. These pathways, however, place the analyte in a different environment (e.g., local dielectric constant), which may alter the mechanism for electron transfer. Also note that the three selectivity pathways are not mutually exclusive. For example, a barrier that contains a finite density of defects can accommodate all three basic mechanisms. That is, tunneling across a well-ordered domain could occur concurrently with electron transfer at defects. The structural details of the defects and the properties of the redox probes will determine the selectivity of the system.

The electron transfer behavior of several redox molecules at self-assembled monolayers have been reported by various laboratories [11-18, 23]. These studies show several striking similarities: neutral, hydrophobic molecules have a much greater tendency to exhibit large electron transfer rates when compared with charged molecules. For example, in the Crooks [18] and Creager [23] laboratories, higher currents were observed for hydrophobic redox probes that are physically larger than corresponding hydrophilic molecules, even though both types of couples have similar rate constants at uncoated electrodes.

In a model proposed by Crooks and co-workers [18], defect structures were important in determining the selectivity of the electrode, but the solvation shell of the redox molecule can be stripped before it permeates the defect (i.e., the free volume of the defect is too small to accommodate solvated molecules). We have applied their analysis to the FcX/$Fe(CN)_6^{4-}$ system. Although our results are in general agreement with this mechanism, there are several distinctions. First, the permeation model was found for nanoporous monolayers prepared using mixed monolayers to induce defect formation (we use single-component adlayers). Moreover, the responses of ferrocene derivatives were not tested. Finally, we also extend a thermodynamic analysis of solvation based on the values of octanol/water partition coefficients for the FcX/$Fe(CN)_6^{4-}$ system. The insight provided by this analysis enables the relation of property descriptors to molecular-level selectivity. Before this analysis can be carried out, however, the other possible mechanisms are evaluated for the present case.

3.3.1. Kinetic Selectivity

Kinetic selectivity results when the inherent facility of heterogeneous electron transfer is different for two redox couples. Thus, kinetic selection allows distinction between two couples that approach the electrode to the same reaction plane. In this situation, the strength of electronic coupling dictates selectivity [42]. From this perspective, outer sphere reactions will be kinetically selected over inner sphere reactions [33].

Kinetic selection can be present at a wide range of electrochemical interfaces, but may only be observed under a certain set of experimental conditions. For example, CV may show reversible diagnostics for two different redox couples even though there are significant differences in the values of k^0. Kinetic selection may not be exposed until reaching a scan rate large enough to detect the existence of the slower couple. Thus, S_r is large when k^0_1 is 100 and k^0_2 is 0.0001 ($S_r = 10^6$); however, a voltammogram collected using a sweep rate of

0.050 V s^{-1} will show inferior resolution to that taken with a 1.0 V s^{-1} sweep rate. This effect is due to the shift of the anodic wave to a larger overpotential that occurs for the secondary species when the larger sweep rate is used (see reference [2] for a detailed explanation). In some cases, modification of the electrode can reveal the disparity in the two reactions by decreasing the rates for both by a comparable relative amount, which then accentuates the more irreversible character of the slower couple.

Model for Kinetic Selection. To illustrate kinetic selectivity that is enabled by an electrode coating, a simple one-dimensional model can be used. In this case, the modifying layer acts as a dielectric medium for tunneling with a barrier thickness of *d*. The value of k^0_{app} is given by

$$k^0_{\text{app}} = k^0_0 e^{-\beta d} \tag{6}$$

where k^0_0 is the value of the heterogeneous electron transfer rate constant at an unmodified (i.e., reference) interface and β is the tunneling constant [33].

To qualitatively relate the model to that for a selective alkanethiolate monolayer, an underivatized gold electrode is assigned a value for *d* of zero, whereas the barrier thickness for a dodecanethiolate adlayer is ~12 Å [27]. A value of 1.0 $Å^{-1}$ is used for β, as per recent literature [12]. The values of k^0_1 and k^0_2 at the coated electrode were chosen to approximate the values obtained experimentally, assuming only kinetic selection. The simulated values at the uncoated electrode were then obtained through Equation (6).

Figure 5 shows simulated *i-E* curves for two heterogeneous electron transfer reactions at an uncoated and coated electrode in which S_r is 10^4. The responses of the uncoated electrode (solid curves) were obtained with k^0_1 and k^0_2 set at 1000 and 0.1 cm s^{-1}, respectively. The *i-E* curves for the modified electrode (dashed curves) were calculated by using 0.006 and 6×10^{-7} cm s^{-1} for k^0_1 and k^0_2, respectively. Figure 5A shows a comparison of the *i-E* curves for the

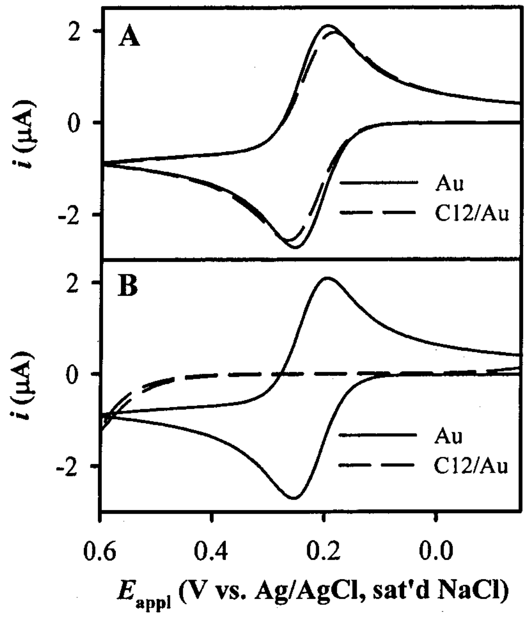

Figure 5. Simulated cyclic voltammetric *i-E* curves of kinetic selectivity for a model analyte (A), and a model sacrificial species (B). The solid curves represent the response at an uncoated Au electrode, while the dashed lines show the attenuated response at a modified electrode (12 Å thick dielectric layer). The values of $k^0{}_1$ and $k^0{}_2$ are 1000 and 0.1 for the model analyte, and 0.006 and 6 x 10^{-7} for the model sacrificial species. Electrode area: 0.02 cm^2; sweep rate: 50 mV s^{-1}.

analyte, whereas that in Figure 5B is for sacrificial species. Importantly, the uncoated electrode exhibits reversible voltammograms for both redox species and no selectivity is possible. However, the modified electrode can distinguish between the two molecules, as revealed by the nearly reversible response for the analyte and the strongly irreversible *i-E* curve for the sacrificial species.

The model outlined above provides important insight into the characteristics of a kinetic selectivity pathway. Experimental measurements of heterogeneous electron transfer kinetics can yield data that appears to indicate kinetic selectivity, even if other mechanisms contribute. Thus, a comparison of the behavior before and after electrode modification should be carried out. Moreover, a theoretical assessment is needed in order to determine the degree of kinetic selectivity expected for the FcX/$Fe(CN)_6^{4-}$ system. For example, the data in Figure 4 yield S_r values of >17 and >10^4, at uncoated and dodecanethiolate coated Au electrodes, respectively. This disproportionate change argues that other pathways are probably important. However, kinetic selection must be one contributing factor for this system.

Theoretical Assessment of Kinetic Selection. If the values of the homogeneous self-exchange rate constants (k_{se}) are known for two redox couples, Marcus theory can be used to predict the selectivity between them [43]. The relationship between k_{se} and k^0 is

$$\frac{k^0}{A_h} = \sqrt{\frac{k_{se}}{A_{se}}} \tag{7}$$

where A_h is the heterogeneous pre-exponential factor (usually 10^4-10^5 cm s^{-1}), k_{se} is the self-exchange rate constant for the reaction between two forms of the same couple (M^{-1} s^{-1}), and A_{se} is the self-exchange pre-exponential factor (usually 10^{11}-10^{12} M^{-1} s^{-1}) [43].

The k_{se} values for $Fc^{0/+}$, $HMF^{0/+}$, and $Fe(CN)_6^{4-/3-}$ in aqueous solutions are listed in Table 2 [44-47]. The ratio of k_{se} for $HMF^{0/+}$ to that for $Fe(CN)_6^{4-/3-}$ is ~150 ($Fc^{0/+}$ to $Fe(CN)_6^{4-/3-}$ is 130). Assuming the same values for A_h and A_{se} for all couples, the expected S_r value is ~12 for both sets of examples. This result implies that there is a fundament kinetic advantage for FcX by an order of magnitude over $Fe(CN)_6^{4-}$. However, an analysis of Figure 4 shows that the observed S_r value is much larger than predicted (experimental values for S_r are >10^4). Moreover, there is a disproportionate change in the heterogeneous kinetics of the two redox couples upon modifying the electrode (i.e., k^0_2 decreases significantly more than k^0_1). These results indicate that while kinetic selection can play a role, there must be other pathways of greater significance to this observation.

Table 2. Summary of molecular properties.

Molecule [a]	$E^{0\prime}$ [b]	k_{se} (M^{-1} s^{-1})	k_a (M^{-1} s^{-1})	D (cm^2 s^{-1}) [c]	r_h (Å)	log (K_{ow})
Fc	+ 0.185	$1.2\ (\pm 0.7) \times 10^{7}$ [d]	N/A	N/A	N/A	3.5
α-MFM	+ 0.215	N/A	N/A	N/A	N/A	2.3
HMF	+ 0.225	1.4×10^{7} [e]	$4\ (\pm 1) \times 10^{7}$ [f]	$4.9\ (\pm 0.7) \times 10^{-6}$ 7×10^{-6} 0.1 M NaCl [g]	4.5	2.0
FDM	+ 0.265	N/A	$3\ (\pm 1) \times 10^{7}$ [f]	$5.9\ (\pm 0.7) \times 10^{-6}$ 6.4×10^{-6} 0.1 M $LiClO_4$ [h]	3.7	1.0
FCA	+ 0.325 [i]	N/A	N/A	N/A	N/A	1.5
FC	N/A	N/A	N/A	N/A	N/A	2.0
AF	N/A	N/A	N/A	N/A	N/A	2.1
FDA	N/A	N/A	N/A	N/A	N/A	0.14
$Fe(CN)_6^{4-}$	+ 0.225	$9.2\ (\pm 1.3) \times 10^{4}$ [j]	-	$5.9\ (\pm 0.4) \times 10^{-6}$ $6.5\ (\pm 0.5) \times 10^{-6}$ [l]	3.7	-1.3 [k]

[a]See Table 1 for chemical structures, names, and abbreviations; [b]versus Ag/AgCl, saturated NaCl (+0.191 V vs. NHE and -0.051 vs. SCE); [c]measured in 0.125 M KCl; [d]the average value and error from three reported rate constants: [45-47]; [e][46]; [f][1]; [g][21]; [h][50]; [i]the pH of the electrolyte is ~7; [j][44]; [k]estimated using Broto's method [41]; [l][33, 48, 49].

3.3.2. Size Exclusion

Differences in the molecular size and/or shape of two redox moieties can enhance or diminish selectivity with respect to defect structures in the adlayer (Scheme 3A). In this instance, only augmentation of kinetic selectivity will be considered (i.e., size exclusion that favors the more kinetically facile couple). In contrast to partitioning (see below), size-

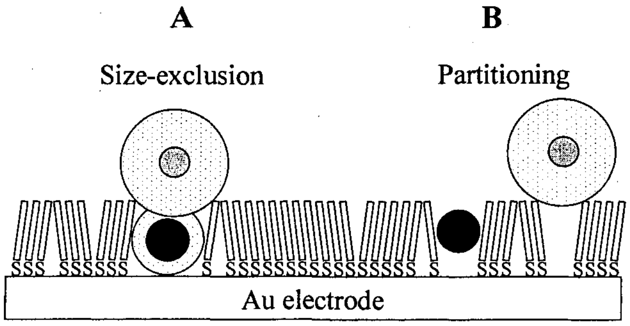

Scheme 3. Two different mechanisms that can enhance or diminish kinetic selectivity: (A) size exclusion; and (B) partitioning.

exclusion is defined by the selection of hydrated molecules. De-solvation is treated as a separate mechanism because of possible implications to design guidelines.

The hydrodynamic radius (r_h) is a measure of the apparent size of a spherical particle undergoing Brownian motion in a viscous medium. The Einstein-Stokes equation relates r_h to the diffusion coefficient (D)

$$D = \frac{RT}{N_A 6\pi\eta r_h} \tag{8}$$

where η is the dynamic viscosity of the surrounding medium (the value for water is 10^{-3} N s m^{-2}) and the remaining terms follow standard definitions. By measurements of D in the desired medium, the possible contribution of size-exclusion can be examined.

The diffusion coefficients of HMF, FDM, and $Fe(CN)_6^{4-}$ were measured using cyclic voltammetry and chronoamperometry at unmodified gold electrodes in 0.125 M KCl. Table 2 lists results, along with the calculated values of r_h. Recent measurements of D for various ferrocene derivatives and ferrocyanide in aqueous electrolyte are in very close agreement with our results [21, 33, 48-50]. These data show that the solvated radii for FDM and $Fe(CN)_6^{4-}$ are similar. Moreover, that for HMF is larger than that for $Fe(CN)_6^{4-}$. These results indicate that size-exclusion cannot lead to the observed selectivity. Further details of these experiments and their relevance to the assessment of the selectivity mechanism are provided in the supplemental supporting information.

In completing this section, X-ray crystallographic data places the molecular radius of ferrocene at 1.4 Å [51], and that for ferrocyanide at 3.1 Å [52]. Because FDM or HMF must shed most of the solvation sphere in order to undergo size-exclusion (i.e., its radius must become effectively smaller than 3.1 Å), the observed selectivity must have a significant contribution from partitioning.

3.3.3. Partitioning

Although the process of elimination implicates partitioning as the key contributor to selectivity (Scheme 3B), there are several intriguing subtleties to the process to consider (e.g., Scheme 4). Permeation of the redox species between alkyl chains could be a selective event for hydrophobic reactants. However, the spacing between adjacent alkyl chains in a well-packed adlayer will not readily accommodate particles of molecular size [53], pointing to the need for the larger free-volume of a defect [18]. Moreover, Creager and co-workers showed that the electron transfer rates for covalently tethered ferrocenes buried in an adlayer are much slower than those for the same moiety positioned at the chain terminus due to the limited availability of counter-ions upon oxidation [29]. Other pathways include selective de-solvation, such that one couple gains an advantage corresponding to the solvation radius of the excluded probe (no permeation), and a combination of de-solvation and size-exclusion. Scheme 4 outlines these selection modes.

Solvation and the Hydrophobic Effect. Partitioning can be broken down

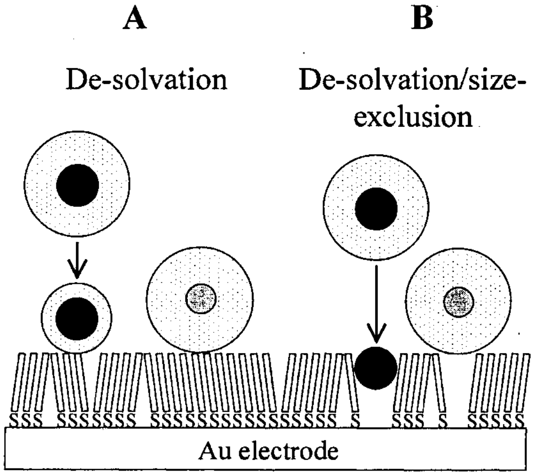

Scheme 4. Illustration of two different modes of partitioning selectivity augmentation: de-solvation (A) and de-solvation/size-exclusion (B).

thermodynamically via the solvation free energy ($\Delta G^0{}_s$)

$$\Delta G_s^0 = \Delta H_s^0 - T\Delta S_s^0 \tag{9}$$

where $\Delta H^0{}_s$ is the solvation enthalpy, $\Delta S^0{}_s$ is the solvation entropy, and T is the absolute temperature. $\Delta H^0{}_s$ is determined by the type and strength of interactions between solvent and solute molecules, whereas $\Delta S^0{}_s$ is affected by the energy cost involved in creating a "cavity" for the solute in the solvent. Thus, $\Delta H^0{}_s$ must be large and negative to drive solvation. As a consequence, hydrophilic molecules have a large and negative solvation free energy in aqueous solutions that is controlled by $\Delta H^0{}_s$. On the other hand, $\Delta S^0{}_s$ can be more important in determining the aqueous solvation characteristics for hydrophobic molecules [54-56].

A parallel analysis can be carried out for a molecule located in the interfacial environment provided by the adlayer. The enthalpy of interaction between the solute molecule and the adlayer ($\Delta H^0{}_i$) can be either negative or positive depending on the nature of the components. The solvation entropy will always increase upon the adsorption of a molecule; the ordered solvent molecules at the interface and which surround the cavity containing the solute will be released to bulk and take more random orientations.

The thermodynamic analysis outlined above indicates that a partitioning event is favored under certain conditions; these are summarized by the processes that dominate solvation and drive adsorption. Thus, for a molecule with a large and negative aqueous solvation free energy, a partitioning event can only occur if $\Delta H^0{}_i$ is large and negative. We have found that FDM and HMF adsorb onto alkanethiolate modified electrodes [57], serving as an indication that $\Delta H^0{}_i$ for these molecules is large and negative.

The octanol/water partition coefficient (K_{ow}) for five ferrocene derivatives and $Fe(CN)_6{}^{4-}$ have been determined using RP-HPLC, and are listed in Table 2. The values of $\log(K_{ow})$ found for Fc, HMF, and FDM are 3.46, 1.96, and 1.07, respectively.

$$K_{ow} = \frac{C_o}{C_w} \qquad (10)$$

where C_o is the concentration of analyte in the octanol phase and C_w is the concentration of analyte in the water phase. Thus, all five FcX molecules have a positive affinity for octanol. However, the value of $\log(K_{ow})$ for $Fe(CN)_6^{4-}$, assessed using molecular modeling software (since it is not retained on the reversed-phase column), is -1.32. Thus, it has a negative affinity for the octanol phase. Although only a qualitative indicator, these results underline the importance of the interaction between the hydrophobic adlayer and FcX molecules, and the affinity of the highly charged $Fe(CN)_6^{4-}$ anion for the aqueous electrolyte phase.

Finally, we note that the kinetics of partitioning must also be considered; application of the octanol/water model indicates that ~5% of the $Fe(CN)_6^{4-}$ in solution would partition into the adlayer. However, if the $Fe(CN)_6^{4-}$ anion is physically too large, partitioning would occur at a negligibly low rate; the thermodynamic analysis does not account for the rate of partitioning. Thus, such partitioning events for FcX moieties must occur rapidly.

The value of the octanol/water partition coefficient is measure of the solvation free energy for these two solvents. As such, it represents a good approximation of the environment at the modified electrode/electrolyte interface. Although not a rigorous comparison, the values of the solvation free energy for the octanol/water system can add insight to the selective electrode.

$$\Delta G^0_{s,ow} = -RT \ln K_{ow} \qquad (11)$$

where $\Delta G^0_{s,ow}$ is the solvation free energy for the octanol/water system, R is the gas constant, and T is the absolute temperature. Thus, a negative value of K_{ow} indicates favorable solvation in the aqueous phase with respect to the octanol. By analogy, a large negative value for

$\Delta G^0_{s,ow}$ would argue against partitioning into the adlayer to result in a large rate constant, while a large positive value indicates a species that can partition.

The rate constant for the heterogeneous electrolysis of ferrocene is large in many non-aqueous solvents [58]. This suggests that partitioning of FcX into the low dielectric medium of an adlayer defect should not inhibit the reaction rate, providing further evidence for the preferential partitioning of FcX molecules.

3.3.4. The Selectivity Mechanism

A model that is consistent with the results of previous studies and the data presented herein is shown in Scheme 4B. The specific interaction between the adlayer and the analyte molecules (FcX) leads to the shedding of the solvation shell. On the other hand, the highly charged $Fe(CN)_6^{4-}$ ion is confined to the aqueous phase. A balance between the number, shape, and size of defect sites in the adlayer leads to a molecular barrier that excludes redox probes that have large solvation free-energies. Thus, in a quest to render the electrode more selective, thereby improving its detection capabilities, the important aspects to maintain are the kinetic and hydrophobic characteristics of the analyte, the free-volume of the adlayer, and the high affinity of the sacrificial species for the electrolyte phase (with a corresponding lack of affinity for the adlayer).

The importance of appropriate defect structures in the adlayer is highlighted by the high sensitivity of selectivity to the preparation conditions of the monolayer. A screening process is normally used to ensure proper reaction characteristics for FcX and $Fe(CN)_6^{4-}$ independently before amplification experiments are performed [1, 2]. During the course of our experiments, we have observed varying selectivity for the ferrocene derivatives over ferrocyanide. Presumably, this effect is due to slightly different sizes and densities of defects in the adlayer.

3.4. System Refinements

The selectivity mechanism can serve as a guide to lower the detection limits by manipulation of the components of the system. This section describes an investigation in which the electrolyte pH was varied in conjunction with three different electrode architectures: uncoated gold, dodecanethiolate-coated gold, and gold modified with a 16-mercaptohexadecanoic acid (16-MHA) based monolayer.

The acid-terminated monolayer was employed with the hope that the negative charge obtained upon increasing pH would act to repel $Fe(CN)_6^{4-}$ through electrostatic effects, while maintaining adequate adlayer hydrophobicity and free volume (to accommodate FcX) due to the increased number of methylene units and the repulsion between the ionic terminal groups, respectively. The pK_a of acid-terminated monolayers is in the range ~7-10 [59]. Thus, a systematic study was carried out in which the ionic strength of the electrolyte was maintained constant at 0.125 M KCl, with pH adjusted to 3, 7, and 11 using KOH or HCl. Figure 6 shows the resulting cyclic voltammetric *i-E* curves that show both the interfacial architecture and pH have a considerable effect on the response; a significant advantage may be obtained both by raising the pH of the electrolyte and by using the 16-MHA-based monolayer.

3.4.1. The Effect of pH

The heterogeneous electron transfer kinetics of $Fe(CN)_6^{4-}$ becomes more sluggish as the pH increases (solid curves). However, the electrolysis rate for FDM does not change appreciably, and the homogeneous amplification reaction is not detectably inhibited by the changes in pH (both k^0_1 and k_a may actually increase with pH; see below). These data indicate that S_r increases with solution pH; a corresponding performance improvement can therefore be realized as long as the double layer charging current does not increase enough to offset the decrease in faradaic background current; see Section 3.4.3.

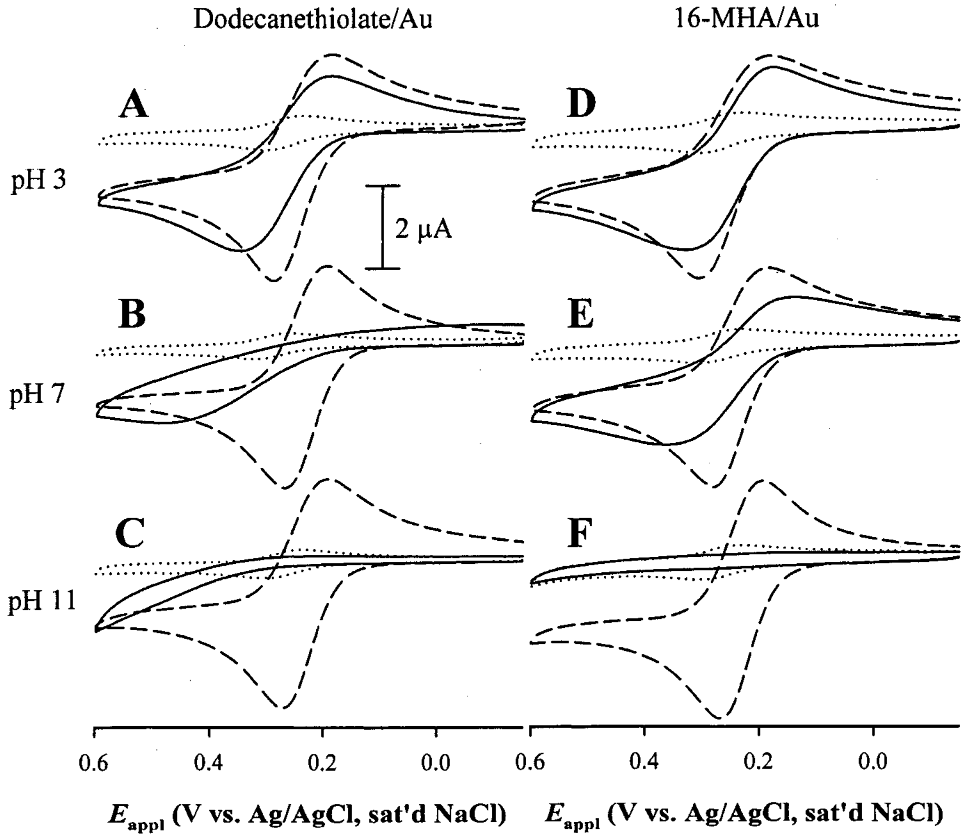

Figure 6. Cyclic voltammetric *i-E* curves that illustrate the effect of an ionic functionality and the pH of the solution on selectivity and amplification. The solid curves are 1.0 mM $Fe(CN)_6^{4-}$, the dotted curves are 0.1 mM FDM, and the dashed curves are 0.083 mM FDM with 0.83 mM $Fe(CN)_6^{4-}$. The effect of pH is illustrated for a dodecanethiolate monolayer modified electrode (first column, curves A-C), and a 16-MHA-based electrode (second column, curves D-F). Sweep rate: 50 mV s^{-1}, geometric electrode area: 0.02 cm^2, and supporting electrolyte: 0.125 M KCl.

A small, but observable decrease in ΔE_p is noted for the amplified voltammograms as the pH increases. For example, at the acid terminated interface, the values for ΔE_p are 125, 97, and 75 mV for pH 3, 7, and 11, respectively. Cyclic voltammetric simulations showed that this could stem from small increases in k^0_1 and/or k_a [1].

A recent study showed that the rate of catalysis of ascorbate by a ferrocene terminated monolayer increased when the electrolyte contained anions with larger hydration energy [60]. This effect is attributed to a reduction in ion-pair formation involving the Fc^+ ion. It is established that such ion pairing inhibits the self-exchange rate of $Fc^{0/+}$ [61, 62]. The stronger ion-pairing between Fc^+ and highly polarizable anions leads to an increase in the ion association activation energy (i.e., the energy required to reorganize the ionic atmosphere around reactants in solution) and therefore increases the effective separation distance. The less effective sharing of the ionic atmosphere between reactants leads to smaller self-exchange rates, which may also translate to heterogeneous reaction rates (see Equation 7). Thus, the increased population of OH^- at elevated pH (OH^- makes up ~1% of the anions at pH 11) favors larger values of k^0_1, k_a, or both; this could account for the changes in ΔE_p.

3.4.2. The Effect of Adlayer Identity

The value of S_r also increases when switching from a methyl-terminated adlayer to the acid-terminated monolayer at pH 11 (note that S_r is better at the dodecanethiolate coated electrode at lower pH). This effect is attributed to the negative charge at the surface resulting from the combination of acidic terminal group and electrolyte pH. Presumably, this negative charge acts to repel the $Fe(CN)_6^{4-}$ ion, while leaving neutral FDM virtually unaffected.

3.4.3. Overall Effects on the Detection Limit

Figure 7 shows *i-E* curves that illustrate the double-layer charging and faradic background currents obtained for the two modified electrodes at pH 11. The scans in electrolyte only (solid curves) in (A) (dodecanethiolate/Au) and (B) (16-MHA/Au) are similar: only a negligible change in double layer charging current is observed in the potential region where FDM detection occurs (i.e., more positive than +0.3 V). Although there is a

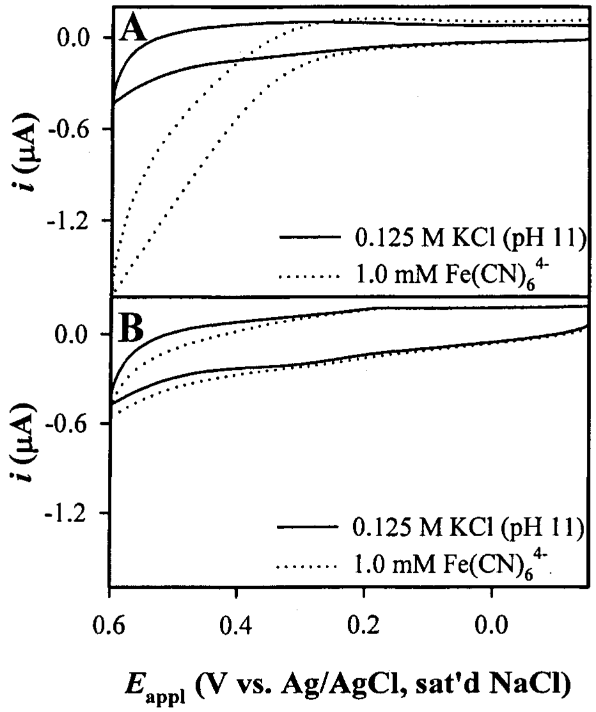

Figure 7. Cyclic voltammetric *i-E* curves showing the decrease in the electrolysis of $Fe(CN)_6^{4-}$ at an acid-terminated monolayer at high pH (11). Background electrolyte only (solid curves) and 1.0 mM $Fe(CN)_6^{4-}$ (dotted curves) at (A) dodecanethiolate/Au; and (B) 16-MHA-derivatized Au. Sweep rate: 50 mV s^{-1}, geometric electrode area: 0.02 cm^2, and supporting electrolyte: 0.125 M KCl.

significant difference in charging current when E_{appl} is less than +0.3 V (i.e., less charging current is observed for the methyl terminated adlayer in this region), the peak potential for FDM is ~+0.3 V such that amplification can only result in the more positive region.

When $Fe(CN)_6^{4-}$ is added, there is an increase in current at the methyl terminated adlayer that is not observed for the acid terminated monolayer (dotted curves). The pH of the solution is 11, and therefore the surface of the 16-MHA/Au electrode presents carboxylate groups which are able to repel the $Fe(CN)_6^{4-}$ ions [59]. Importantly, the current for $Fe(CN)_6^{4-}$ is reduced even at quite large overpotential (i.e., +0.5 to +0.6 V), enabling the use of more positive detection potentials. This result also implies that the concentration of $Fe(CN)_6^{4-}$ could be increased, leading to higher amplification factors while maintaining low faradaic background current.

Since the double layer charging current is not different in the positive potential region, the improvement in the detection limit that results from using the acid terminated monolayer and a solution pH of 11 with redox recycling is potentially related to the decrease in the background when $Fe(CN)_6^{4-}$ is present (relative to that observed using the dodecanethiolate modified electrode). We previously showed that amplification factors of ~100 resulted in an improvement of the detection limit of from 7 μM to ~500 nM [1]. The disproportionate relationship was due to the increase in background obtained at the dodecanethiolate modified electrode when $Fe(CN)_6^{4-}$ was added to the electrolyte. However, with the 16-MHA based electrode, the amplification factor may give a nearly direct indication of the improvement in the detection limit since only very small current is observed that is attributable to the oxidation of $Fe(CN)_6^{4-}$ [1]. Thus, the amplified detection limit is improved to ~50 nM, or ~140 times better than that without redox recycling.

3.4.4. Other Factors

We also note that when using an acid-functionalized monolayer, we observed an increased tendency for FDM to adsorb onto the electrode. In fact, after exposure to FDM, electrodes must be rinsed with both water and ethanol. Subsequent testing in a $Fe(CN)_6^{4-}$ solution was used to ensure the lack of an increased background due to irreversibly bound FDM (we add that electrodes rinsed with only water after FDM exposure showed an increase in the voltammetric background when tested in $Fe(CN)_6^{4-}$ solutions). The *i-E* curves in Figure 6 were collected using a single 16-MHA based electrode. The response for pH 11 (Figure

6(F)) was collected after exposure to FDM in the other solutions (pH 3 and 7), showing that the background will not increase due to adsorption of FDM if care is taken to rinse the electrode. We presume that the increased interaction of FDM with the acid-terminated monolayer is due to hydrogen bonding [15].

The fact that the ionization of the monolayer acts to increase S_r provides additional insights into the physical origins of selectivity. That is, the electrolysis rate for FDM still appears to be unaffected by the presence of the adlayer, while the reaction of $Fe(CN)_6^{4-}$ becomes even more suppressed. Taken together, our results show that a delicate balance between several important variables is required to maintain effective redox recycling. However, the guidelines established by the physical selectivity mechanism outlined in this work shows that the logical design of these systems for improved performance is possible.

4. Conclusions

This work investigated selectivity mechanisms at alkanethiolate modified electrodes. The results presented herein indicate that multiple pathways are possible. For the $FcX/Fe(CN)_6^{4-}$ redox recycling system, there are several important characteristics: the facile heterogeneous electron transfer kinetics of ferrocenes and their hydrophobic properties; the hydrophobic nature of the adlayer and the free volume of defect sites; and the high charge on the sacrificial species combined with aqueous electrolyte solutions. These factors combine to result in a selective partitioning event for FcX, leading to very high selectivity over $Fe(CN)_6^{4-}$. We add that the degree of selectivity observed is very sensitive to monolayer preparation conditions, indicating the importance of defect structures [18].

Finally, this work also showed that the insights provided by the selectivity mechanism can be used to improve the amplified detection limit to ~50 nM (~140 times better performance than without redox recycling) by decreasing the magnitude of the faradaic background current when $Fe(CN)_6^{4-}$ is present in the solution.

5. Acknowledgements

This work was supported, in part, by Eastman Chemical. A. J. B. gratefully acknowledges a Proctor and Gamble Fellowship. The Ames Laboratory is operated for the US Department of Energy by Iowa State University under Contract no. W-7405-eng-82.

6. References

[1] A. J. Bergren and M. D. Porter, J. Electroanal. Chem. 585 (2005) 172.

[2] A. J. Bergren and M. D. Porter, J. Electroanal. Chem. Submitted (2005).

[3] P. T. Radford and S. E. Creager, Anal. Chim. Acta 449 (2001) 199.

[4] P. T. Radford, M. French, and S. E. Creager, Anal. Chem. 71 (1999) 5101.

[5] L. Coche-Guerente, V. Desprez, J.-P. Diard, and P. Labbe, J. Electroanal. Chem. 470 (1999) 53.

[6] L. Coche-Guerente, V. Desprez, P. Labbe, and J.-P. Diard, J. Electroanal. Chem. 470 (1999) 61.

[7] D. Zheng, N. Wang, F.-Q. Wang, D. Dong, Y.-G. Li, X.-Q. Yang, L.-H. Guo, and J. Cheng, Anal. Chim. Acta 508 (2004) 225.

[8] H.-G. Hong and M. D. Porter, J. Electroanal. Chem. 578 (2005) 113.

[9] P. N. Bartlett, P. Tebbutt, and R. G. Whitaker, Prog. Reaction Kinetics 16 (1991) 55.

[10] M. French and S. E. Creager, Langmuir 14 (1998) 2129.

[11] Q. Cheng and A. Brajter-Toth, Anal. Chem. 67 (1995) 2767.

[12] H. O. Finklea, "Electrochemistry of Organized Monolayers of Thiols and Related Molecules on Electrodes" in Electroanalytical Chemistry: A Series of Advances, A. J. Bard and I. Rubinstein, eds., Marcel Dekker, Inc., New York, 1996.

[13] K. Takehara, H. Takemura, M. Aihara, and M. Yoshimura, J. Electroanal. Chem. 404 (1996) 179.

[14] F. Malem and D. Mandler, Anal. Chem. 65 (1993) 37.

[15] A. Dalmia, C. C. Liu, and R. F. Savinell, J. Electroanal. Chem. 430 (1997) 205.

[16] J. Zhao, L. Luo, X. Yang, E. Wang, and S. Dong, Electroanalysis 11 (1999) 1108.

[17] Y. Y. Jun and K. S. Beng, Electrochem. Commun. 6 (2004) 87.

[18] O. Chailapakul and R. M. Crooks, Langmuir 11 (1995) 1329.

[19] A. M. Becka and C. J. Miller, J. Phys. Chem. 96 (1992) 2657.

[20] A. M. Becka and C. J. Miller, J. Phys. Chem. 97 (1993) 6233.

[21] C. Cannes, F. Kanoufi, and A. J. Bard, J. Electroanal. Chem. 547 (2003) 83.

[22] H. O. Finklea, "Electroanalytical Methods: Self-Assembled Monolayers on Electrodes" in Encyclopedia of Analytical Chemistry, R. A. Meyers, ed. Vol. 11, John Wiley & Sons, Ltd, Chichester, 2000, p. 10090.

[23] K. A. Groat and S. E. Creager, Langmuir 9 (1993) 3668.

[24] W. Miao, Z. Ding, and A. J. Bard, J. Phys. Chem. B 106 (2002) 1392.

[25] C. Miller, P. Cuendet, and M. Gratzel, J. Phys. Chem. 95 (1991) 877.

[26] C. Miller and M. Gratzel, J. Phys. Chem. 95 (1991) 5225.

[27] M. D. Porter, T. B. Bright, D. L. Allara, and C. E. D. Chidsey, J. Am. Chem. Soc. 109 (1987) 3559.

[28] J. F. Smalley, H. O. Finklea, C. E. D. Chidsey, M. R. Linford, S. E. Creager, J. P. Ferraris, K. Chalfant, T. Zawodzinsk, S. W. Feldberg, and M. D. Newton, J. Am. Chem. Soc. 125 (2003) 2004.

[29] J. J. Sumner and S. E. Creager, J. Phys. Chem. B 105 (2001) 8739.

[30] A. Ulman, Chem. Rev. 96 (1996) 1533.

[31] A. Ulman, An Introduction to Ultrathin Organic Films From Langmuir-Blodgett to Self-Assembly, Academic Press, San Diego, CA, 1991.

[32] R. S. Nicholson, Anal. Chem. 37 (1965) 1351.

[33] A. J. Bard and L. R. Faulkner, Electrochemical Methods: Fundamentals and Applications, John Wiley & Sons, Inc., New York, 2001.

[34] T. Braumann, J. Chromatogr. 373 (1986) 191.

[35] J. G. Dorsey and M. G. Khaledi, J. Chromatogr. A 656 (1993) 485.

[36] M.-M. Hsieh and J. G. Dorsey, Anal. Chem. 67 (1995) 48.

[37] S. Griffin, S. G. Wyllie, and J. Markham, J. Chromatogr. A 864 (1999) 221.

[38] A. Paschke, M. Manz, and G. Schuurmann, Chemosphere 45 (2001) 721.

[39] A. C. D. Kock and D. A. Lord, Chemosphere 16 (1987) 133.

[40] U. S. E.P.A., *OPPTS 830.7570 Partition Coefficient (n-Octanol/Water), Estimation By Liquid Chromatography,* Environmental Test Methods and Guidelines, U. S. Government Printing Office, Washington D. C., 1996.

[41] P. Broto, G. Moreau, and C. Vandycke, Eur. J. Med. Chem. 19 (1984) 71.

[42] M. D. Newton, Chem. Rev. 91 (1991) 767.

[43] R. A. Marcus, Electrochim. Acta 13 (1968) 995.

[44] M. Shporer, G. Ron, A. Loewenstein, and G. Navon, Inorg. Chem. 4 (1965) 361.

[45] S. F. Nelsen, R. F. Ismagilov, K. E. Gentile, M. A. Nagy, H. Q. Tran, Q. Qu, D. T. Halfen, A. L. Odegard, and J. R. Pladziewicz, J. Am. Chem. Soc. 120 (1998) 8230.

[46] G. E. McManis, R. M. Nielson, A. Gochev, and M. J. Weaver, J. Am. Chem. Soc. 111 (1989) 5533.

[47] R. M. Nielson and J. T. Hupp, Inorg. Chem. 35 (1996) 1402.

[48] Y. Bai, P. Sun, M. Zhang, Z. Gao, Z. Yang, and Y. Shao, Electrochim. Acta 48 (2003) 3447.

[49] L. Bortels, B. V. d. Bossche, J. Deconinck, S. Vandeputte, and A. Hubin, J. Electroanal. Chem. 429 (1997) 139.

[50] W. Zhang, I. Gaberman, and M. Ciszkowska, Electroanalysis 15 (2003) 409.

[51] A. Togni and T. Hayashi, "Ferrocenes", VCH Publishers, New York, 1995.

[52] G. Frenking and C. Loschen, Inorganic Chem. 43 (2004) 778.

[53] C. A. Widrig, C. A. Alves, and M. D. Porter, J. Am. Chem. Soc. 113 (1991) 2805.

[54] K. Lum, D. Chandler, and J. D. Weeks, J. Phys. Chem. B 103 (1999) 4570.

[55] N. T. Southall, K. A. Dill, and A. D. J. Haymet, J. Phys. Chem. B 106 (2002) 521.

[56] B. Windom, P. Bhimalapuram, and K. Koga, Phys. Chem. Chem. Phys. 5 (2003) 3085.

[57] See Supplement Information.

[58] A. M. Bond, T. L. E. Henderson, D. R. Mann, W. Thormann, and C. G. Zoski, Anal. Chem. 60 (1988) 1878.

[59] C. D. Bain and G. M. Whitesides, Langmuir 5 (1989) 1370.

[60] G. Valincius, G. Niaura, B. Kazakeviciene, Z. Talaikyte, M. Kazemekaite, E. Butkus, and V. Razumas, Langmuir 20 (2004) 6631.

[61] E. S. Yang, M.-S. Chan, and A. C. Wahl, J. Phys. Chem. 84 (1980) 3094.

[62] A. M. Kuznetsov, D. K. Phelps, and M. J. Weaver, Int. J. Chem. Kinetics 22 (1990) 815.

7. Supplemental Supporting Information

7.1. Introduction

This document describes the experimental details and results of the adsorption analysis used in arguments presented in the main text of the paper.

7.2. Experimental

Adsorption was assessed using symmetrical double potential step chronocoulometry. The details of the mathematical treatment are discussed in Section 7.3.1. Experimentally, 0.18 mM FDM or HFM in 0.125 M supporting electrolyte (KCl) at uncoated and dodecanethiolate coated gold electrodes were used as test solutions. In all cases, *i-E* curves were used to screen the modified electrodes for reversible behavior (a requirement of the theoretical treatment [1]). The formal reduction potentials ($E^{0\prime}$) of HMF and FDM are +0.225 and +0.265 V, respectively. For both analytes, chronocoulometry data collection was initiated after holding the electrode potential at -0.15 V for 15 s to allow equilibration in the absence of electrolysis (i.e., decay of the double-layer charging current). The potential was then stepped to +0.6 V (> +0.3 V vs. $E^{0\prime}$ for both couples) for 10-15 s. Finally, the potential was stepped back to -0.15 V for 10-15 s.

7.3. Results and Discussion

Adsorption can be qualitatively established and, in some cases, quantitated using symmetrical double potential step chronocoulometry (SDPSC) [1-6]. SDPSC utilizes measurements of charge as a function of time for a sequence of two symmetric, appropriately gauged and abrupt potential steps. This technique was used to asses the interfacial excess of

FDM and HMF molecules at uncoated and dodecanethiolate modified gold electrodes. Experimentally, the forward step from an equilibrated potential (i.e., the double layer current has decayed to zero) where no electrolysis occurs to a value that results in diffusion-limited electron transfer is followed after a set time (τ) by a step back to the initial potential (usually for τ s).

7.3.1. Mathematical Description of Adsorption Diagnostics

The charge for a forward potential step (Q_F) has at least two contributions: the faradaic reaction of diffusing redox molecules and double layer reorganization. Adsorbed molecules may also contribute to Q_F. Thus, for times up to τ

$$\frac{Q_F}{A} = \frac{2nFD^{\frac{1}{2}}C_b t^{\frac{1}{2}}}{\pi^{\frac{1}{2}}} + Q_{dl} + Q_{ads} \qquad (1)$$

where the multivariate term on the right represents the charge for freely diffusing reactants, Q_{dl} is the charge consumed by the double layer, Q_{ads} is the charge due to adsorbed reactant, A is the electrode area, n is the electron stoichiometry, F is the faraday, D is the diffusion coefficient, C_b is the bulk concentration of the redox species, and t is the time after the potential step.

The charge-time relationship for the reverse step (Q_R) is

$$\frac{Q_R}{A} = \frac{2nFD^{\frac{1}{2}}C_b}{\pi^{\frac{1}{2}}}\theta + Q_{dl} \qquad (2)$$

where

$$\theta = \left(\tau^{\frac{1}{2}} + (t-\tau)^{\frac{1}{2}} - t^{\frac{1}{2}}\right) \qquad (3)$$

and the reaction product is not adsorbed.

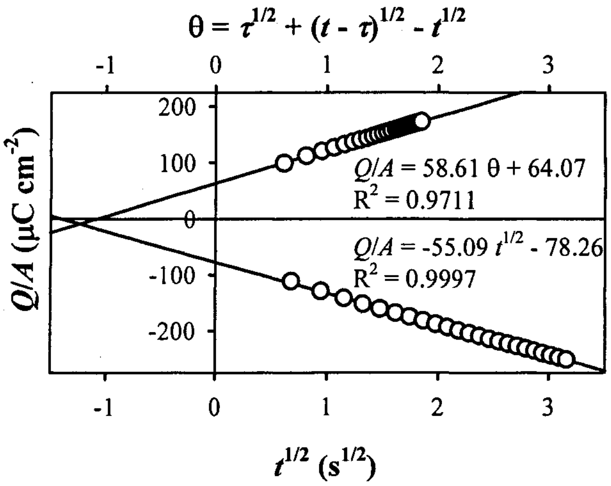

Figure S-1. Anson plot for 0.18 mM HMF in 0.125 M KCl at uncoated Au.

Adsorption diagnostics are easily visualized in a plot of Q_F vs. $t^{1/2}$ and $-Q_R$ vs. θ on the same graph (an Anson plot). If the two lines intersect on the x-axis, the redox-active molecule is not adsorbed, and the value of both intercepts gives Q_{dl}. If only the reactant (and not the product) is adsorbed, then the Q_F vs. $t^{1/2}$ intercept will be larger than the $-Q_R$ vs. θ intercept, with the difference allowing a direct measure of the surface coverage (Γ_O). Likewise, if only the electrode product adsorbs, the difference in intercepts is the surface coverage of the product. Finally, if both forms of the redox probe adsorb, the intercepts will either intersect (if the same level of both forms is adsorbed) or give underestimated coverage for the two respective cases.

7.3.2. Experimental Determination of FcX Adsorption

Figure S-1 shows an Anson plot for 0.18 mM HMF at uncoated Au in 0.125 M KCl. Note that the intersection lies in quadrant III. This is evidence that HMF adsorbs onto the electrode. Although HMF$^+$ may also be adsorbed, if this were the case, we can say with certainty that the surface coverage of HMF is higher than that for HMF$^+$. Bond et al. estimated that a monolayer of ferrocene occupies 4.6 x 10^{-10} mol cm^{-2} [7]. The difference between the intercepts in Figure S-1 correlates to ~30% of a monolayer. The Anson plot for 0.18 mM FDM was similar in both qualitative and quantitative terms (~30% of a monolayer).

Previous studies have found ferrocene adsorption onto metal and glassy carbon electrodes from aqueous solutions with NaF, $NaClO_4$, and Li_2SO_4 as the supporting electrolyte [7], finding 5 to 10% coverage at unmodified electrodes. Our own Anson adsorption analysis using uncoated Au was in general agreement with these findings. However, we employed a different supporting electrolyte (KCl) and derivatized ferrocenes (FDM and HMF) at higher concentrations, and consequently found higher levels of adsorption (~30% of a monolayer).

Figure S-2 shows an Anson plot for 0.17 mM HMF at dodecanethiolate modified gold. Note that the intercept for the Q_r vs. θ plot gives a value less than that for the uncoated electrode. This serves as an indicator that the double-layer capacitance of the coated electrode is lower than the uncoated electrode, as expected [8]. However, the difference between the two intercepts for the dodecanethiolate-coated Au electrode corresponds to a slightly lower excess (20% of a monolayer). Thus, it is safe to say that 20% more HMF adsorbs with respect to HMF$^+$ on the modified electrode. A similar analysis showed that both

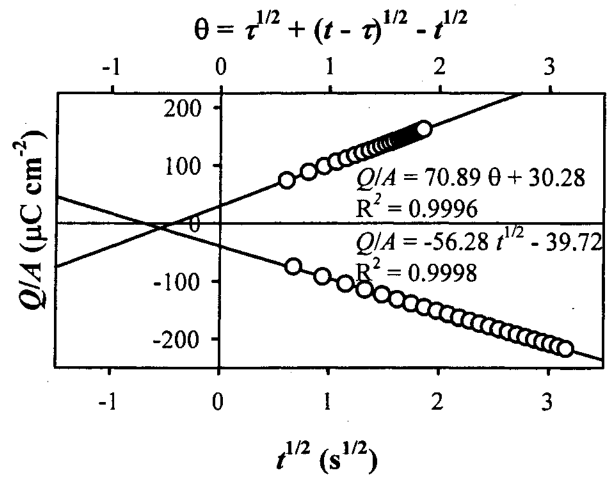

Figure S-2. Anson plot for 0.17 mM HMF in 0.125 M KCl at dodecanethiolate/Au.

FDM and HMF adsorb onto both Au and dodecanethiolate/Au at about the same apparent level. The slightly lower excess for the coated electrode could be an indicator that either more FcX^+ molecules are adsorbed at the thiolated electrode, or that the monolayer inhibits adsorption. Although not quantitative, this important result establishes that an attractive force exists between neutral ferrocenes and the adlayer (although an interaction may also exist for the monovalent ferrocenium cations).

The nature of the interaction of FcX at dodecanethiolate/Au was further tested. CVs of

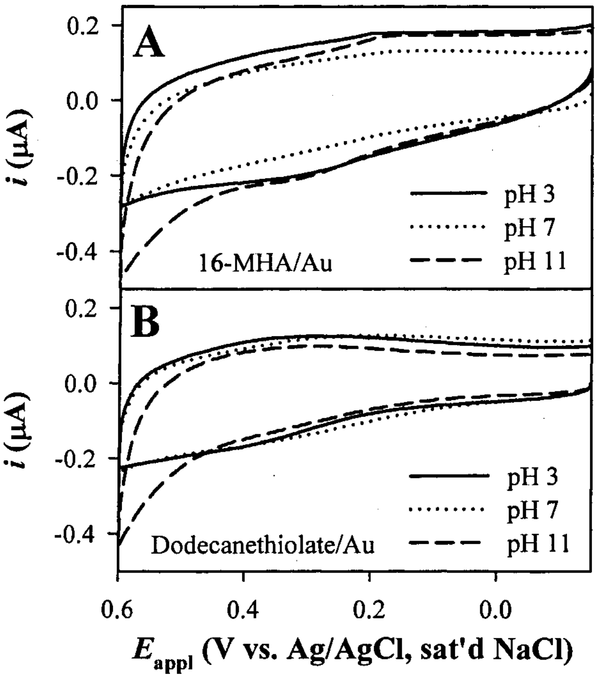

Figure S-3. CVs of background in 0.125 M KCl for the (A) 16-MHA-based monolayer modified electrode, and (B) the dodecanethiolate modified electrode. Comparison of these *i-E* curves illustrates that only a small increase in capacitance results, and therefore the detection limit is improved by the factor in which the current is decreased at this electrode when $Fe(CN)_6^{4-}$ is present. Sweep rate 50 mV s^{-1}, geometric electrode area 0.02 cm^2, and supporting electrolyte 0.125 M KCl.

electrodes in 0.125 M KCl immediately after modification and after exposure to solutions of 0.2 mM FDM or HMF in 0.125 M KCl for ~20 min (after rinsing with electrolyte), were identical. Moreover, CVs of 1 mM $Fe(CN)_6^{4-}$ before and after such exposure gave equivalent results. We conclude that any adsorbed ferrocene is lost upon rinsing. Taken together, our adsorption analysis shows that FDM and HMF weakly adsorb onto dodecanethiolate coated Au electrodes. Although completely reversible, this interaction indicates that hydrophobic ferrocene derivatives and a hydrophobic coating may be integral parts of redox recycling systems. For a treatise on the effects of irreversible adsorption, see Creager and Radford [9].

Although we found that HMF and FDM adsorb onto uncoated Au, chronoamperometric determinations of D in the presence of adsorbed analyte would lead to an overestimation of the value of D (i.e., if the contribution from adsorbed molecules was subtracted from the diffusional current, slightly smaller values of D would be obtained). This, in turn, would lead to larger values for r_h, further indicating that size-exclusion of hydrated molecules is not a feasible mechanism to account for the selectivity of this system.

7.3.3. Supplemental Voltammetry

Figure S-3 shows the background *i-E* curves for the two different electrodes utilized in interfacial design refinements as a function of pH, illustrating that only negligible changes are observed.

7.4. References

[1] F. C. Anson, Anal. Chem. 38 (1966) 54.

[2] F. C. Anson, Anal. Chem. 36 (1964) 932.

[3] F. C. Anson, J. H. Christie, and R. A. Osteryoung, J. Electroanal. Chem. 13 (1967) 343.

[4] F. C. Anson and D. A. Payne, J. Electroanal. Chem. 13 (1967) 35.

[5] J. H. Christie, R. A. Osteryoung, and F. C. Anson, J. Electroanal. Chem. 13 (1967) 236.

[6] B. Case and F. C. Anson, J. Phys. Chem. 71 (1967) 402.

[7] A. M. Bond, E. A. McLennan, R. S. Stojanovic, and F. G. Thomas, Anal. Chem. 59 (1987) 2853.

[8] M. D. Porter, T. B. Bright, D. L. Allara, and C. E. D. Chidsey, J. Am. Chem. Soc. 109 (1987) 3559.

[9] S. E. Creager and P. T. Radford, J. Electroanal. Chem. 500 (2001) 21.

CHAPTER 5. ODD-EVEN OSCILLATION IN THE HETEROGENEOUS ELECTRON TRANSFER RATE OF SOLUTION-BASED REDOX COUPLES AT SHORT-CHAIN ALKANETHIOLATE MONOLAYERS ON GOLD

A paper to be submitted to *The Journal of Physical Chemistry*[1]

Adam Johan Bergren, Grant A. Edwards, Erik J. Cox, and Marc D. Porter

Abstract

This paper examines odd-even oscillations in the interfacial properties of short-chain alkanethiolate monolayers on gold. Specifically, the first observation of an odd-even alternation of the apparent heterogeneous electron transfer rate constant (k^0_{app}) for solution-based redox couples is reported and discussed. In an attempt to account for this dependence, several structural properties were evaluated and relevant literature is reviewed. These investigations revealed that many physical and chemical parameters can exhibit trends that are dependent on the chain length and whether there are an odd or even number of methylene units in the alkyl chain (i.e., an odd-even effect). Possible origins of the rate effect are discussed in light of the structural characterizations and electron transfer mechanisms, highlighted by the potential drop profile of the electrical double layer, quantum interference, and adlayer thickness alternations. Moreover, in addition to an odd-even effect in k^0_{app} of solution-based redox couples, a previously unreported odd-even effect was discovered in thickness data for both model calculations and ellipsometric measurements. This data

---

[1] A preliminary report was submitted to *The Journal of the American Chemical Society*, as a short communication (rejected), and appears in the dissertation of Grant A. Edwards (Iowa State University, 2006).

provides an intriguing basis for extending electron transfer theories, and also provides several new insights into the relationship between the structure of these adlayers and their function.

1. Introduction

Self-assembled monolayers provide a versatile toolbox for applications in fundamental and applied electrochemistry [1-4]. As a result, the structure and interfacial properties of alkanethiol-derived ($CH_3(CH_2)_nSH$) adlayers on gold and other metals have been extensively investigated [5-20]. More recently, this system has been employed in the development of methodologies to improve the sensitivity of electrochemical detectors [21-24]. As part of our interests in this area, we have undertaken a systematic study of the relationship between the many experimental variables that may affect the formation and resulting structure of the adlayer, which, in turn, would have an impact on electrochemical performance. These studies led to several intriguing, and some unexpected, findings that prompted a critical evaluation of the structure and properties of these important surface modifiers. Herein, the results of varying the number of methylene units (n) in the alkyl chain are detailed, where an odd-even oscillation in the heterogeneous electron transfer rate constant (k^0_{app}) of solution-based redox couples serves as a focal point. Odd-even effects are also observed in other properties of these adlayers. Taken together with insights from relevant literature, likely mechanisms for the rate effect are proposed and evaluated.

A review of literature shows that the interfacial properties of alkanethiolates on gold are influenced by n in two ways. First, an increase in n gives rise to a thicker adlayer, which results in an increase in the barrier to heterogeneous electron transfer and the corresponding evolution of other properties (e.g., decreases in capacitance and increases in contact angle [7, 25, 26]). Second, subtle alternations in a number of interfacial properties that are intimately linked to whether *n* is odd- or even-numbered have also been reported [15-19, 27]. For example, vibrational spectroscopy establishes that the orientation of the terminal methyl group oscillates with respect *n* [18-20]. This structural oscillation has therefore often been identified as the underlying cause of odd-even effects in surface free-energy [19], friction [17, 28], and other parameters [29-31].

The alternation of the terminal group orientation for alkanethiolates on gold arises as a consequence of the Au-S-C bond angle (ca. 104° [14]), and the all-trans arrangement of the alkyl chains [7]. An idealized depiction of the average structure is given in Figure 1, which has the carbon-carbon backbone canted ~24° with respect to the surface normal [18]. As shown, the permanent dipole moment of the methyl group, which is closely aligned with the transition dipole of the symmetric methyl stretch, is canted ~53° for an adlayer in which *n* is even but only ~26° when *n* is odd [18, 19]. This variation yields an oscillation in interfacial surface free energy that can be manifested by differences, for example, in wettability [19] and friction [17].

While the body of literature related to odd-even effects for alkanethiolates on gold continues to grow, the observation of such a dependence for the heterogeneous electron transfer rate constant of solution-based redox couples has not previously appeared. This situation, especially at first glance, is particularly intriguing considering that odd-even

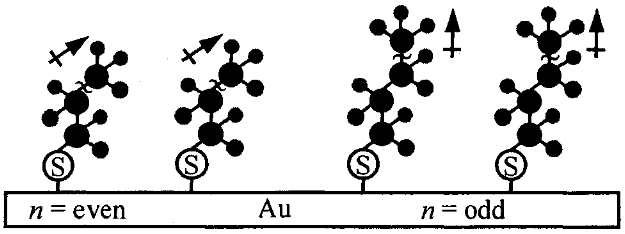

Figure 1. Idealized model illustrating the oscillation of the methyl group orientation for alkanethiolate monolayers on gold. The transition dipole of the symmetric methyl stretch is indicated by the arrow.

modulations of k^0_{app} have been observed for several closely related systems. For example, alternations of k^0_{app} for adlayers with ferrocene groups covalently tethered to the chain terminus of thiolate monolayers were found in two separate works [12, 16]. Moreover, an odd-even effect on intramolecular electron transfer rates in photoexcited complexes with bridges composed of three to seven methylene units has also been reported [32]. Finally, theoretical treatments predict an odd-even dependence in electronic coupling strengths across saturated bridges as a consequence of quantum interference [33, 34].

We suspect that odd-even oscillations in k^0_{app} for solution-based redox couples have not been reported due to the difficulty in reproducing identical conditions with respect to adlayer formation. The function of alkanethiolate monolayers on gold with respect to heterogeneous electron transfer is highly dependent on the details of many variables [35]. For example, changes in the roughness of the underlying gold surface can result in marked differences in the efficiency of a deposited adlayer in blocking the electrolysis of solution-based redox couples [36]. The odd-even oscillation of k^0_{app} with respect to n is subtle; we have observed only been able to observe this effect using specialized surface preparation methods, and for specific thiol concentrations and immersion times (see experimental section). For the experiments reported herein, these procedures were paramount to the ability to detect an odd-even effect in k^0_{app}.

In this paper, we present unequivocal evidence for the odd-even oscillation of k^0_{app} for solution-based redox couples at short-chain alkanethiolate monolayers on gold (n = 6-11). This effect was observed during the course of studies largely intended for other purposes (i.e., increasing the selectivity and reproducibility of modified electrodes). The nature of this unique trend prompted a critical evaluation of other interfacial properties in an attempt to reveal the origins of the rate alternation. These additional experiments, along with molecular modeling and a literature review, revealed many odd-even effects (some previously reported), including a thickness oscillation that correlates with the orientation (see Figure 1) and rate effects.

Taken together, these investigations bring to light many different possible origins of the oscillation of k^0_{app} with respect to n, acting alone or in concert. These include quantum interference, electrical double layer structure, and adlayer thickness alternations. These findings provide valuable insights into theoretical and experimental heterogeneous electron transfer and also serve to further characterize self-assembled monolayers. For example, this data may provide the first experimental confirmation of quantum interference using solution-based redox couples. Moreover, there are many opportunities for expanding theoretical models and experimental methods to refine an understanding of odd-even effects.

2. Experimental

2.1. Chemicals and Reagents

Distilled water was further purified by deionization with a Millipore Milli-Q water system. Sulfuric acid, sodium fluoride, and potassium ferricyanide were obtained from Fisher. Potassium ferrocyanide (trihydrate) was purchased from Sigma. Hydroxymethylferrocene (HMF) and all thiols were provided by Aldrich. Punctilious grade ethanol from Aaper was used to prepare thiol solutions. All chemicals were used as received. Thiol purity was assessed by gas chromatography/mass spectrometry (GC/MS) [37], and found to exceed 95% in all cases. Importantly, the observed impurities are not expected to appreciably affect the quality of resulting adlayers, and no odd-even oscillations in purity were observed.

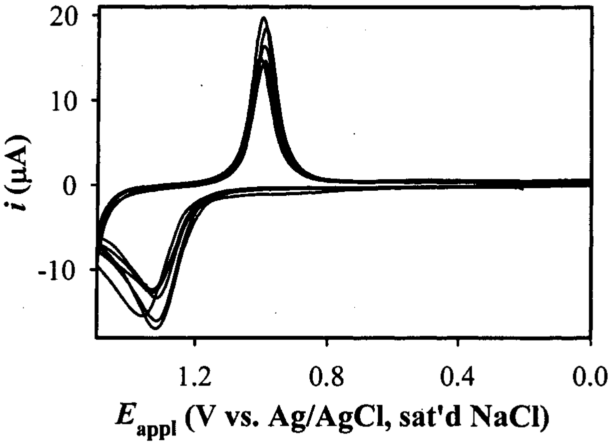

Figure 2. CV *i-E* curves for polished gold electrodes in 1.0 M H_2SO_4. Geometric electrode area: 0.020 cm^2, sweep rate: 50 mV s^{-1}. These curves illustrate the range of accepted electrodes.

2.2. Substrate Preparation

Electrochemistry. Polycrystalline gold disk electrodes from Bioanalytical Systems (geometric area: 0.020 cm^2) were used for electrochemistry. For surface preparation prior to modification, these electrodes were: 1) polished with successively finer grades (1.0, 0.3, 0.05 μm) of slurried alumina; 2) sonicated in isopropanol and water for ~10 min each; and 3) cycled once between 0.0 and +1.5 V (50 mV s^{-1}) in 1.0 M H_2SO_4.

The electrochemical treatment served as a final surface preparation procedure prior to adlayer deposition and as a quality control metric. That is, both the shape of the voltammogram [38] and the charge under the stripping wave [39] were monitored to ensure reproducible surface preparation. Figure 2 shows several overlaid cyclic voltammetric (CV) current-potential (*i-E*) curves. Importantly, we note that only electrodes that give a shape indicative of polycrystalline gold, and with a stripping charge of 1.44 ± 0.79 mC cm^{-2} were qualified for modification (other electrodes were re-polished). This value is 2.5 standard deviations for over 100 electrodes, and represents a balance between acceptable surface reproducibility and electrode preparation time. Electrodes meeting these quality criteria were rinsed with water and ethanol, and then immersed for 20.0 min in 1.0 mM ethanolic thiol solutions, rinsed with ethanol, and used for electrochemical experiments immediately. These steps, developed in an ongoing effort to understand the subtle influence of preparation conditions on electrode performance, were paramount in realizing the ability to detect an odd-even effect on k^0_{app}.

Structural Characterizations. For infrared reflection absorption spectroscopy (IRRAS), wetting, and ellipsometric measurements, gold substrates were prepared by resistive evaporation of ~15 nm Cr (evaporation rate: 0.1 nm s^{-1}) followed by 300 nm Au (rate: 0.2 nm s^{-1}) onto clean glass microscope slides (1 x 3 in. or 1 x 1 cm, Fisher) in an Edwards E306A coating system at a pressure of 7.5×10^{-7} torr.

For IRRAS and contact angle measurements, immediately upon removal from the evaporation chamber, the slides were placed into deionized water for storage (all uncoated gold samples were stored for less than 6 h prior to monolayer deposition). Prior to each IRRAS measurement, one slide was taken from the storage solution, rinsed with ethanol, and immersed in a 1.0 mM thiol solution in ethanol for 20.0 min, rinsed with ethanol, and dried in a directed stream of high-purity nitrogen.

For ellipsometric measurements, uncoated Au samples were removed from the sample chamber and stored in a sealed container (samples were stored for less than 2 h prior to measurement). Optical constants were measured for ten different spots on each uncoated sample (acquisition time ~15 min). After obtaining these parameters, the slide was immersed into a 1.0 mM thiol solution for 20.0 min, rinsed with ethanol, and the optical constants of the coated Au assessed for the same ten spots that were used prior to coating. This spot-correlation was critical to reduction of the error to acceptable levels [40], and was aided by a sample stage controlled using optical encoding (precision 1 μm). Reproducible sample placement with respect to the laser spot (diameter ~1 mm) was carried out using a jig mounted on the stage surface. This jig enabled the placement of the sample by confining the edges of the glass slide to a fixed location. Care was taken to orient the sample in the same direction before and after monolayer deposition.

2.3. Electrochemical Measurements

Electrochemical measurements were carried out using a CH Instruments model 660B potentiostat. Freshly prepared electrodes were used in a three-electrode cell, with a silver/silver chloride, saturated sodium chloride electrode (Ag/AgCl, sat'd NaCl) as a reference and a flame-cleaned, coiled platinum wire serving as the auxiliary electrode. Solutions of 10.0 mM ferrocyanide and 1.0 mM HMF were prepared using a stock solution of aqueous 0.125 M sodium fluoride as the supporting electrolyte. All solutions were purged with high purity nitrogen for ~10 min prior to electrochemical measurements, and a blanket of nitrogen was kept over the solution throughout all experiments. Freshly prepared electrodes were exposed to test solutions in the following order: 0.125 M NaF; 10.0 mM $Fe(CN)_6^{4-/3-}$ in 0.125 M NaF; and 1.0 mM HMF in 0.125 M NaF. The electrodes were rinsed copiously with water after each step.

For electrochemical impedance spectroscopy (EIS) experiments, equal concentrations (10.0 mM) of both $Fe(CN)_6^{4-}$ and $Fe(CN)_6^{3-}$ were used, and the bias potential was set at the formal reduction potential ($E^{0\prime}$, 0.225 mV). For HMF, the bias potential was held at $E^{0\prime}$ (+0.227 mV) for 10 s before, and throughout each measurement.

2.4. Infrared Spectroscopy

Infrared reflection spectra were acquired with a Nicolet 740 FT-IR spectrometer equipped with a liquid nitrogen-cooled MCT detector using *p*-polarized light incident at 80° [19]. The sample chamber was purged with nitrogen for 20 min prior to initiating data collection. Spectra were obtained by referencing 1024 sample scans to 1024 background scans at 2 cm^{-1} resolution. Background spectra were collected using a gold slide coated with per-deuterated octadecanethiolate [41]. Three sample spectra were obtained before collecting a new background after the acquisition of its IRRAS spectrum. The same samples were used for contact angle measurement immediately (~35 min acquisition time).

2.5. Contact Angle Measurements

Advancing (θ_a) and receding (θ_r) contact angles were measured using a Rame-Hart Model 100-00 115 goniometer with deionized water as the probe liquid. The measurements used ~5 μL water drops that were dispensed onto the substrate surface using a 10 μL Gilson Pipetman. The values of θ_a were determined after the pipette tip was slowly pulled away from the drop while increasing its volume, while that for θ_r was assessed after slowly pulling the pipette tip away from the drop while decreasing its volume.

2.6. Ellipsometric Film Thickness Measurements

Experimental film thickness measurements were made using an Optrel Multiskop GBR ellipsometer in null mode, with a single wavelength (632.8 nm) source at a 70° angle of incidence. For uncoated Au, the values of the real and imaginary refractive indexes were ca. 0.17 and -3.5, respectively. Determination of the adlayer thickness utilized a three-phase model, the refractive index of gold, and the Δ and Ψ values (with associated error) for each sample. The refractive index for the adlayers was set constant at 1.5 [2].

3. Results and Discussion

The results in this paper are presented in three separate, but related sections. All electrochemical rate data are presented in the first section, which is followed by a segment detailing structural characterizations of the adlayers. Finally, the third section analyzes possible origins of the odd-even effect in k^0_{app} based on our findings and relevant literature.

3.1. Electrochemistry

The first evidence of an odd-even effect was developed based on the values of k^0_{app} for two solution-based couples (hydroxymethylferrocene, HMF, and ferro/ferricyanide, $Fe(CN)_6^{4-/3-}$) as determined using both cyclic voltammetry (CV). These results were then expanded upon through a series of measurements via electrochemical impedance spectroscopy (EIS). Collectively, the odd-even effect was observed for several independent trials in which *n* varied from 6-11. An "independent trial" consists of the preparation of a series of modified electrodes and subsequent testing within a 24 h window. In all cases, odd-even oscillations were observed. Moreover, the agreement of the data is striking in that adlayers with an odd number of methylene units (i.e., an "odd-numbered" layer) always produce values of k^0_{app} lying at the minima of a saw-tooth trend. These observations are discussed in detail in this section.

Cyclic Voltammetry. Figure 3 shows a series of cyclic voltammetric current potential (*i*-*E*) curves for 10.0 mM $Fe(CN)_6^{4-/3-}$ in 0.125 M KCl at three electrodes where *n* is 9, 10, and 11. Importantly, the peak separations (ΔE_p), which are related to k^0_{app} [42, 43] (a larger ΔE_p

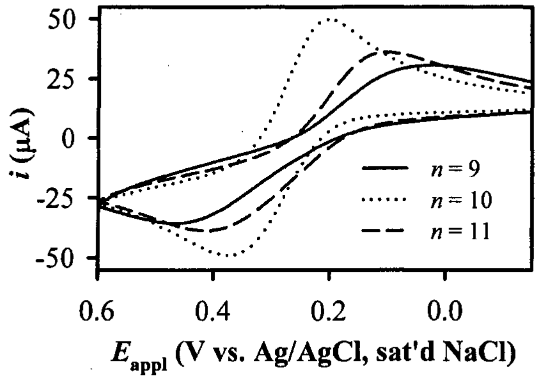

Figure 3. Current-potential curves for 10.0 mM $Fe(CN)_6^{4-/3-}$ in 0.125 M KCl at three different gold electrodes modified with alkanethiolate monolayers. An odd-even trend is observed that prompted a more thorough study. Geometric electrode area: 0.020 cm^2, sweep rate: 50 mV s^{-1}.

indicates a lower value of k^0_{app}), exhibit an odd-even dependence with respect to *n*. Thus, the electrodes modified with the odd-numbered adlayers exhibit more attenuated rates of heterogeneous electron transfer, as revealed by their larger ΔE_p values: ΔE_p for $n = 10$ is smaller that that for $n = 9$ and 11. This data, collected in a series of experiments designed to examine the effect of thiol chain length on selectivity [23, 24], served as an intriguing basis for further investigation of odd-even effects in heterogeneous electron transfer from solution-based redox couples. In subsequent testing of many independent trials (i.e., series of freshly prepared electrodes), the same trend was observed (see below).

Figure 4A shows *i-E* curves for a solution of 1.0 mM HMF in 0.125 M NaF at a series of short-chain alkanethiolate modified electrodes. First and foremost, the listed values of ΔE_p undergo a clear oscillation. As shown in Figure 4B, translation of the ΔE_p values to k^0_{app} using Nicholson's method (used when the peak separation was between 70 and 212 mV [43]) produces a general tendency toward lower values for k^0_{app}. However, this decrease in k^0_{app} is modulated by an odd-even dependency. Thus, k^0_{app} for $n = 8$ is actually greater than that for *n*

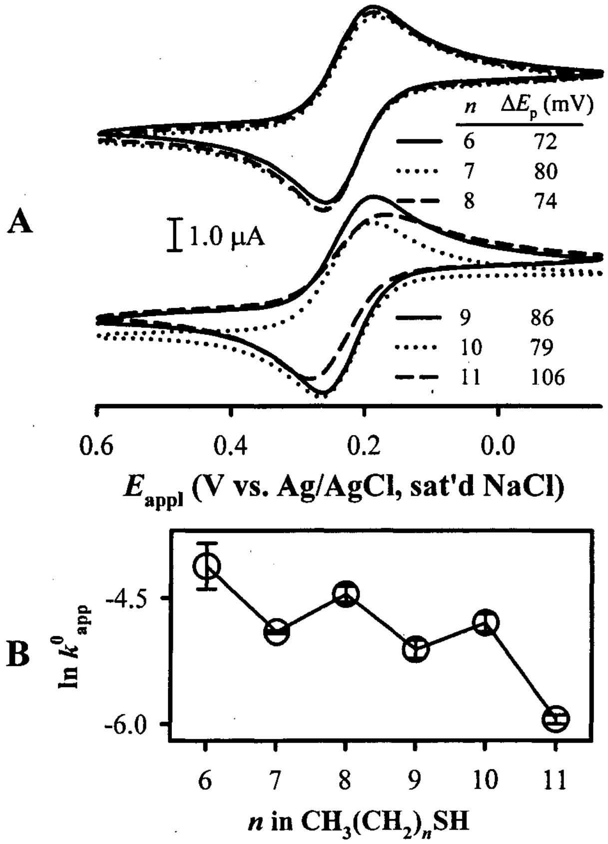

Figure 4. (A) Cyclic voltammograms of 1.0 mM HMF in 0.125 M NaF at alkanethiolate adlayers on gold. The alternation of k^0_{app} with n is clear in the translated rate constants, as shown in (B). Geometric electrode area: 0.020 cm^2, sweep rate: 50 mV s^{-1}.

= 7, but less than that for n = 6. A parallel statement applies to the trend for n = 9 through 11, (i.e., k^0_{app} for n = 10 is larger than n = 9 and n = 11), noting that k^0_{app} for n = 9 is smaller than that for n = 8.

Electrochemical Impedance Spectroscopy. In addition to cyclic voltammetry, electrochemical impedance spectroscopy (EIS) was used to assess k^0_{app}. Figure 5 (open circles) shows a series of experimental Nyquist plots for 10 mM $\mathrm{Fe(CN)_6}^{4-/3-}$ in 0.125 M NaF at alkanethiolate monolayer modified electrodes (n = 6-11). These data show two important characteristics. First, the semi-circular trend in the data indicates a strong kinetic limitation in

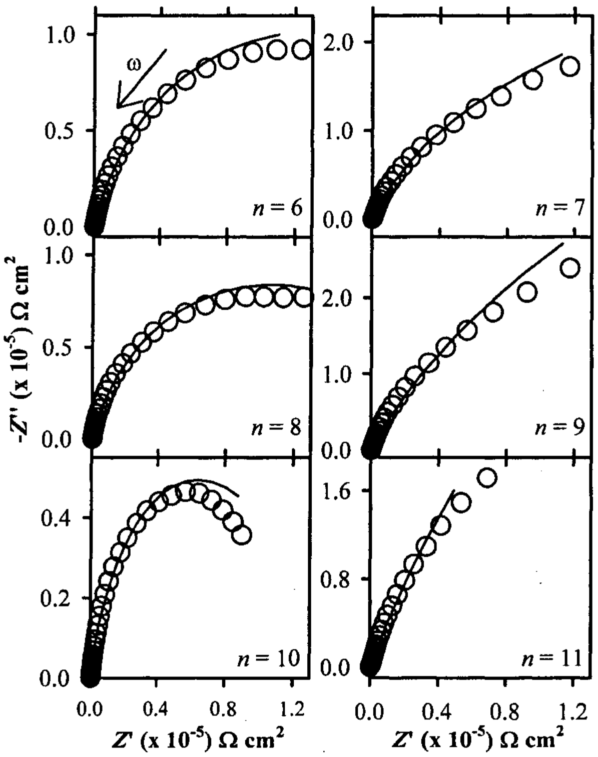

Figure 5. Nyquist plots for a series of alkanethiolate modified Au electrodes with 10.0 mM $Fe(CN)_6^{4-/3-}$ in 0.125 M NaF. The open circles are experimental data points and the solid lines are equivalent circuit fits (see text). AC voltage amplitude: 7 mV (constant DC bias at $E^{0\prime}$), frequency range: 1-10^5 Hz, geometric electrode area: 0.020 cm^2.

the heterogeneous electron transfer reaction, as expected for a highly charged redox couple at electrodes modified with a hydrophobic adlayer. Moreover, there is an oscillation in the radii of the semi-circles, a parameter that is related to k^0_{app} (i.e., a larger radius translates to a smaller value of k^0_{app}). Thus, a qualitative odd-even effect is again exhibited in the rate data via these Nyquist plots.

The EIS data was fit to a modified Randles circuit, as described elsewhere [42, 44]. Briefly, the circuit consists of a solution resistance in series with a branch having a charge transfer resistance (R_{ct}) in parallel with a constant phase element with an exponent of 0.85

[35]. The constant phase element is used to account for heterogeneous capacitive behavior due to, e.g., surface roughness [44]. A Warburg impedance element was added in series with R_{ct} (when necessary). The fits are shown by the solid lines in Figure 5. The data was fit by minimizing the error function (the least squares of the offset between the fit and data) using CHI Electrochemical Workstation 5.07 software. The value of R_{ct}, being obtained from fitting the EIS data is translated to k^0_{app} through the relation

$$k^0_{\mathrm{app}} = \frac{RT}{n_{\mathrm{e}}^{2}F^{2}AC_{\mathrm{b}}R_{ct}} \tag{1}$$

where R is the gas constant, T is the absolute temperature, n_{e} is the redox stoichiometry, F is the faraday, A is the electrode area (0.020 cm^2), and C_{b} is the redox molecule concentration [42]. Although the error in the determination of R_{ct} is affected by the quality of the fit, the fit is acceptable since a simple equivalent circuit was used that is easily interpreted. Moreover, the values of k^0_{app} for this series of electrodes were also determined using cyclic voltammetry to ensure accuracy.

The results of the EIS data analysis for the data in Figure 5 are shown in Figure 6A (circles). Figure 6A (triangles) shows the results from analysis of *i-E* curves for this same series of electrodes. Values of k^0_{app} were obtained from (irreversible) voltammograms using the Butler-Volmer relation

$$k^0_{\mathrm{app}} = \frac{i^0}{n_{\mathrm{e}}FAC_{\mathrm{b}}} \tag{2}$$

where, i^0 is the faradaic current at the formal reduction potential, and the other terms were defined previously [42]. The two sets of data in Figure 6A (EIS and CV rate determinations) show good agreement, noting that the analysis of *i-E* curves produces systematically larger values of k^0_{app} than those determined using EIS. It is likely that the values determined from

CV are overestimated as a consequence of the uncertainty involved in correcting for the double layer charging current (a capacitance of ~2.6 μF cm^{-2} would account for the offset, which is within the uncertainty determined in CV experiments with only electrolyte present).

Summary of Rate Data. Figure 6 shows plots of k^0_{app} vs. n for several trials. These data

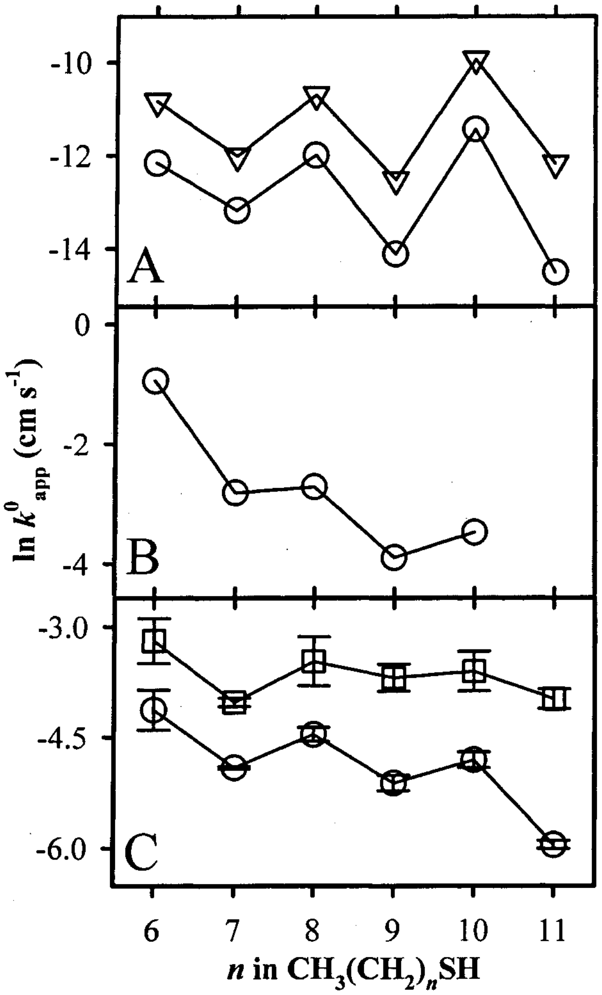

Figure 6. The natural log of k^0_{app} as a function of n for a series of alkanethiolate modified Au electrodes measured with CV and EIS. (A) $Fe(CN)_6^{4-/3-}$ determined using EIS (circles) and CV (triangles); (B) HMF determined with EIS; and (C) HMF determined with CV for two independent trials.

demonstrate an odd-even effect in k^0_{app} for solution-based redox couples at short-chain alkanethiolate monolayers. There are several details exhibited in these plots that require consideration. First, the shape of the plot shows a weak dependence on the identity of the redox couple, implying a difference in the details of the electron transfer mechanism. This result is probably accounted for by the difference in solvation free energy between the highly charged $Fe(CN)_6^{4-/3-}$ couple and hydrophobic $HMF^{0/+}$. Second, the observed trends are nearly independent of the method used to determine the k^0_{app}. This important result is a strong indication that the odd-even effect in k^0_{app} is not an experimental artifact. Finally, the same trend is evident for both redox couples; in all cases the tendency is for the electrodes modified with the odd-numbered adlayers to manifest values of k^0_{app} at the bottom of a saw-tooth trend. This result indicates that the pathway leading to these oscillations must be general.

The remainder of this paper is composed of structural characterizations of the adlayer systems, followed by a discussion of possible origins of the odd-even effect on k^0_{app}.

3.2. Structural Assessments

Many of the previously reported odd-even oscillations in the interfacial properties of alkanethiolate monolayers on gold have been attributed to structural effects (i.e., the oscillation of the terminal methyl group orientation). Thus, several techniques were used to measure experimental parameters related to these effects for this series of adlayers. These data are presented in this section, and is followed by an analysis of multiple mechanisms that can account for the odd-even oscillation of k^0_{app}.

IRRAS Structure/ Orientation Evaluation. The average arrangement of the alkyl chains was assessed using infrared reflection absorption spectroscopy (IRRAS). This

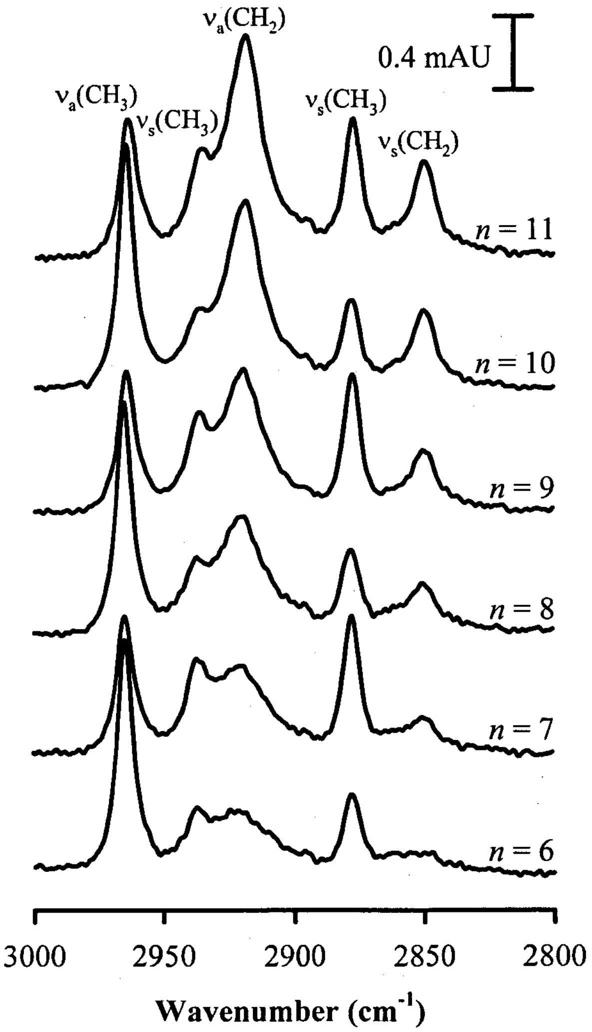

Figure 7. Infrared reflection spectra for alkanethiolate monolayers on gold.

technique yields insights regarding chain configuration [45-58] and its orientation with respect to the gold surface [19, 59]. Alignment can be assessed by considering the infrared surface selection rules [60, 61]. Simplistically, the absorbance of a vibrational mode at a highly reflective metal is strongest when the transition dipole is normal to the surface [18]. In previous reports, odd-even effects in IRRAS spectra were observed and discussed [18, 19]. These works serve as a basis for comparison of our results, noting that they are mutually supportive.

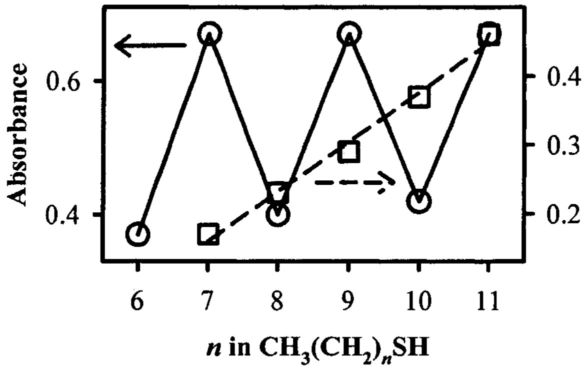

Figure 8. Absorbance (mAU) for $\nu_s(CH_3)$ (—), and $\nu_s(CH_2)$ (---) from the infrared reflection spectra in Figure 7.

Figure 7 shows a series of infrared reflection spectra for adlayers where *n* is 6-11. These data establish that the different adlayers are structurally similar, grow in thickness as *n* increases, and exhibit an odd-even oscillation of the methyl group orientation. First, the increase in film thickness is confirmed by the increase in the strength for the polymethylene chain modes; this is shown in Figure 8 (dashed line, right ordinate) for the symmetric methylene stretch, $\nu_s(CH_2)$, at 2850 cm^{-1}. Second, the linearity of the plot indicates that there is no detectable difference in the average orientation of the polymethylene chains throughout this span of chain lengths. Third, the strength of the methyl stretches undergoes a saw-tooth variation; this is demonstrated in Figure 8 (solid line, left ordinate) for the low-energy Fermi-resonance-split mode of the symmetric methyl stretch, $\nu_s(CH_3)$, at 2878 cm^{-1}.

Wettability. Evidence for an odd-even effect in wettability is illustrated in Figure 9, which plots the advancing (θ_a) and receding (θ_r) contact angles for water as the probe liquid for the same samples used in the IRRAS experiments. While near the precision of the measurements, it is nevertheless evident that θ_a is higher when *n* is odd. In other words, the odd-numbered adlayers are more hydrophobic than the even-numbered adlayers. This type of dependence was observed in an earlier report from our laboratory for alkanethiolates at

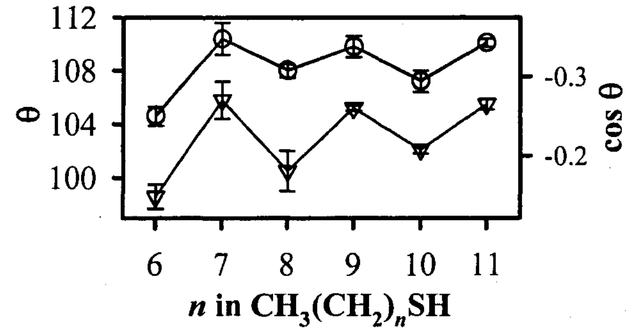

Figure 9. Contact angle data for alkanethiolate monolayers on gold: θ_a (circles) and θ_r (triangles) for water in air.

silver, and was attributed largely to a screening of the dispersion forces from the underlying structure by the odd-even oscillations of the permanent dipole moment of the methyl group [19]. Similar odd-even effects have been observed in wetting measurements of related self-assembled monolayer systems [11, 14]. For example, the oscillation of the wettability of methoxy-terminated adlayers was attributed to surface dipole effects [11].

Thickness. To obtain preliminary expectations for the adlayer thickness, molecular models were constructed. Surprisingly, determinations of thickness using geometric models constructed with molecular modeling software showed an odd-even oscillation as *n* increases. Figure 10 (triangles) shows data calculated for a series of model alkanethiol molecules using ChemDraw 3-D (Cambridge software). These data were obtained by considering the adlayer thickness as the distance between the center of the sulfur atom (i.e., the surface) and a point in the direction of the surface normal (for an all-trans alkyl chain arranged with a 30° tilt and a 50° twist about the C-C backbone) that also lies in a plane that is parallel to the surface and passes through the center of the most distal carbon atom.

The results of these calculations prompted a re-evaluation of the idealized models in Figure 1. Recalling that IRRAS data has placed the tilt and twist angles of the all-trans alkyl

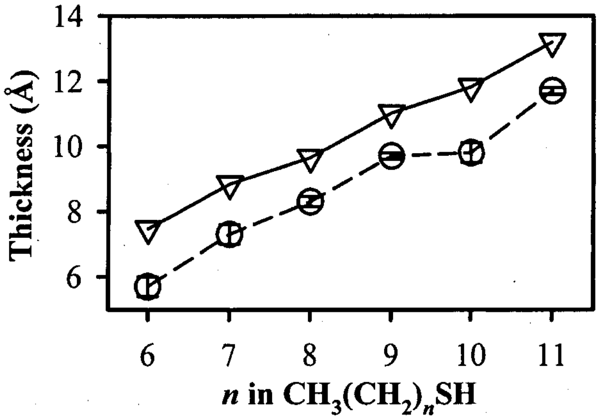

Figure 10. Model (triangles) and ellipsometric (circles) thicknesses as a function of *n* for alkanethiolates on gold.

chains at ca. 26° and ca. 55°, respectively [19], the alternation in thickness can be understood to arise from the effect of the terminal methyl group orientation. For example, an adlayer that begins with an odd number of methylene units will increase in thickness less upon a unit increase in *n* than an even-numbered adlayer. Having established a theoretical and logical basis for an odd-even effect in adlayer thickness, the next step was an experimental evaluation using ellipsometry.

Importantly, odd-even oscillations in thickness were observed for two sets of data. However, the first set of measurements produced an error that obscured the trend. Thus, a procedure was developed that gave an error low enough to enable a clear analysis of the alternation (see experimental section for details). Figure 10 (circles) shows experimental thickness data as a function of *n*, where an odd-even trend is discernable. Strikingly, the shape of the plots and for the model and experimental data is the same (i.e., the odd-numbered adlayers tend toward the top of the saw-tooth trend). Moreover, the magnitude of the alternation for the two sets of data is very similar. The offset between the two sets of data is probably due to the uncertainty in the length of the gold-sulfur bond in the modeling data, or the refractive index of the adlayer used in analysis of ellipsometric data. Remarkably, this thickness trend can provide a compelling basis for the origin of the odd-even effect in $k^0{}_{\text{app}}$ (see Section 3.3.3.).

The lack of an odd-even oscillation in the IRRAS data for the polymethylene chain modes (e.g., see Figure 8, dashed line) should not be assumed to be inconsistent with the observations of odd-even alternations in thickness. The linear increase in Figure 8 for $\nu_s(CH_2)$ indicates an increase in the number of absorbing units and therefore is a qualitative indicator of an increase in thickness. Any difference in the absolute thickness of the layers would be difficult or impossible to detect; the measurement is sensitive to the orientation and total number of units, and not to the adlayer thickness.

3.3. Possible Origins

The odd-even alternation in $k^0{}_{\text{app}}$ could arise as a consequence of several structural and mechanistic pathways. Characterizations of our adlayers show that the idealized model shown in Figure 1 is a good average representation. Analysis of these models reveals several different conceptual origins for the odd-even alternation in $k^0{}_{\text{app}}$. This section outlines and evaluates these possibilities.

As a starting point in developing rationalizations for the odd-even effect in $k^0{}_{\text{app}}$, it is useful to consider the dependency of the rate constant for a tunneling event across a dielectric barrier

$$k^0{}_{\text{app}} = k_0^0 e^{-\beta d} \tag{3}$$

where $k^0{}_0$ is the unimpeded heterogeneous electron transfer rate constant, β is the tunneling coefficient, and d is the separation distance between the redox couple and the electrode [42]. In such a mechanism, the exponential term ($-\beta d$) describes the convolution of the electron transfer mechanism and the effective barrier thickness. Thus, anything that causes this term to oscillate with respect to *n* can account for the rate data presented in Section 3.1. Three separate effects will be discussed: double layer effects (β and *d*), electron transfer mechanisms (β), and the effective adlayer thickness (*d*).

3.3.1. Double Layer Effects

The IRRAS and contact angle data establishes that the orientation of the permanent dipole moment of the terminal methyl group undergoes an odd-even oscillation as *n* increases. A simplified model was constructed to investigate the possible effects of the dipole directionality on the profile of the potential drop across the electrical double layer. As shown in Figure 11, the applied potential undergoes a linear change across the gold-sulfur bond that is assumed to remain constant as *n* increases (region 1) [5]. The alkyl chain results in a second linear change (region 2) between the applied and solution values; this dictates the

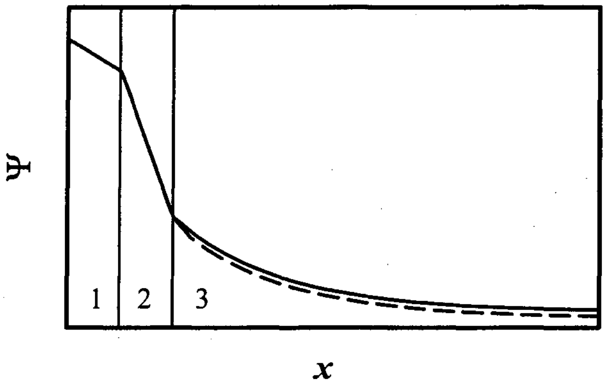

Figure 11. Model for the electrical double layer. The applied potential is dropped across the sulfur atom (region 1), then across the alkyl chain (region 2). At this point, the effect of the orientation of the terminal dipole impacts the remaining potential that must be dropped in the diffuse layer to solution value (region 3). Thus, an odd-numbered chain is represented by the dashed line, while an even-numbered adlayer is shown by the solid line.

value at the terminal plane of the adlayer. This first two components of the potential drop would result in a constantly decreasing value of k^0_{app} as n increases (i.e., note the general downward trends in Figure 6). Finally, the terminal methyl group occupies a region of potential drop before the diffuse layer, which must account any remaining differences between the applied and solution potentials (the interface between regions 2 and 3). This model shows that a modulation of the potential at the reaction plane of the redox couples by the alternating permanent dipole moment of the methyl group could lead to the odd-even effect in k^0_{app}.

In an attempt to refine the conceptual model and provide estimates of the perpendicular dipole magnitude at the adlayer surface, a set of model calculations were performed using molecular modeling software (Cambridge ChemDraw 3-D Ultra 8.0, MOPAC). While the bulk of these findings will be reported separately [62], we note here that an odd-even modulation of the dipole strength and, interestingly, the adlayer thickness (see above) were both evident.

This modeling data shows that for the double layer effect to accurately account for the rate data, the odd-numbered adlayers, with the methyl group oriented more toward the surface normal must induce a larger potential drop between the hydrocarbon chain region and the diffuse layer than the even-numbered chains. Also implicit in this model is the proper relationship between the relative values of the potential of zero charge, the directionality of the charge separation in the atomic components in the adlayer (e.g., the gold-sulfur bond is polarized with more negative charge residing on the sulfur atom [37]), and the formal reduction potential of the redox couples. Thus, such a double layer effect is an intriguing basis for odd-even oscillations in k^0_{app}. However, these requirements suggest that tests carried out using different redox couples, with formal reduction potentials in a different region with respect to the potential of zero charge, may not show an odd-even oscillation in k^0_{app}.

In addition to the orientation of the terminal methyl group affecting the potential drop profile in the electrical double layer, there are other possibilities to consider. For example, the interfacial composition of electrolyte components can have an impact on the measured values of k^0_{app} [63]. Experimental measurements of the double layer capacitance using CV with only electrolyte in solution and from equivalent circuit fits of the EIS data did not reveal any odd-even effects. However, these measurements exhibited a large error, and therefore the negative result does not imply the lack of such a trend.

3.3.2. Electron Transfer Mechanisms

Bridge mediated electron transfer has been the focus of many theoretical and experimental investigations [64-66]. Recent experimental measurements using molecular electronics devices provide additional insight [67-75]. There are several aspects of these topics that we will use in our analysis of the rate data, beginning with an analysis of the attenuation factor (i.e., β) from the data in Figure 6.

General Mechanisms. The value of the tunneling coefficient is dependent on the electron transfer mechanism. Thus, experimental measurements of this factor can be used to derive insights into the details of the electron transfer mechanism. For electron transfer across a saturated bridge, the structure of the chain can impact the facility with which the electron transfer event occurs.

For direct tunneling (non-resonant) across a saturated bridge (i.e., an alkanethiolate), values of β are typically ~1 Å^{-1} [2, 9, 25, 26, 65]. Several more recent reports show that slightly lower values (0.3-0.8 Å^{-1}) are also often encountered [67-75]. The complexity of this topic precludes a detailed analysis of β values reported in the literature. However, we will show that our data are generally consistent with all of these works, and that the odd-even effect in k^0_{app} could arise as a consequence of a fundamental difference in the electron transfer mechanism for the odd-numbered layers relative to the even-numbered adlayers.

Values for β were determined by substituting the values of k^0_{app} (from experimental data at the modified electrodes, see Figure 6), k^0_0 (from experimental data at uncoated Au, 0.01 cm s^{-1}, for $Fe(CN)_6^{4-}$, and estimated at 2 cm s^{-1} for HMF), and d from the modeled thickness measurements (see Figure 10). This analysis yields values for β of 0.4-1.0 $Å^{-1}$, which is consistent with the works of others [67-75]. We add that slightly larger values were obtained for $Fe(CN)_6^{4-}$ (0.8-1.0 $Å^{-1}$) than for HMF (0.4-0.6 $Å^{-1}$), which may reflect the ability of HMF to partition into the adlayer, reducing its effective thickness [76].

Most importantly, the average values of β for the odd-numbered adlayers are slightly larger than that for the even-numbered layers (e.g., for the data in Figure 6A for $Fe(CN)_6^{4-}$, circles, $\beta_{\mathrm{even}} = 0.8 \pm 0.2$ $Å^{-1}$ and $\beta_{\mathrm{odd}} = 0.9 \pm 0.1$ $Å^{-1}$). These results indicate that tunneling efficiency is lower for the odd-numbered adlayers. Moreover, the calculation of β was carried out using the modeled thickness, which includes an odd-even alternation arising as a consequence of this orientational effect. Therefore, the slightly lower value of β is indicative of a fundamental difference in the electron transfer mechanism.

The origins of the mechanistic difference between electron transfer events at the odd- and even-numbered adlayers could be caused by a number of possibilities. First, a slight structural variation that induces a difference in the coupling strength cannot be discounted. Recall that the alignment of the terminal methyl group is more toward the surface normal of the odd-numbered alkyl chains. There is evidence for differences in the types and efficiencies of electron transfer pathways when small structural disturbances (i.e., disorder) are introduced into thiolate monolayers [77, 78]. Thus, the small difference in β for the odd and even adlayers that we observe could be caused by the oscillation of the orientation of the terminal methyl group. However, there is another possibility that must be considered: quantum interference.

Quantum Interference. A relevant and compelling finding from theory developed by Marcus and Hsu [33, 34] is the odd-even oscillation in the coupling strength between a donor and acceptor separated by a saturated hydrocarbon. Importantly, the quantum interference effect was shown theoretically for two different configurations of a ferrocene tethered to an alkyl chain (i.e., an ester and direct attachment was considered) [33]. The direction of the oscillation depends on the linkage (i.e., the saw-tooth trend is different for the two systems tested) and the orientation of the redox group [33].

Quantum interference can be understood by considering the path of an electron between a donor and acceptor [79]. First, this pathway is broken into discrete segments composed of individual electronic orbitals, with each orbital forming one link in a chain. There will be several combined composite orbitals through which the electron can pass, as determined by the overlap integral of for adjacent links. Because electronic orbitals are signed quantities [66], when summing the contribution from multiple links in a chain, positive or negative electronic coupling can result. Thus, positive coupling is a consequence of a composite orbital having the same sign at both the donor and acceptor. Upon adding one additional unit in the bridge (i.e., a methylene unit), the coupling becomes negative due to the signs opposing at these locations.

Although a detailed understanding of the electronic states of the donor and electrode, the orientation of the redox couple during the electron transfer, and the total number of bridging units in our system (interfacial solvation may be important here, adding some number of links) is required to determine if quantum interference can account for the data in Section

3.1, it remains a strong possibility. This is highlighted by the observation of odd-even oscillations in experimental data for ferrocene groups tethered at the chain terminus [16, 27].

3.3.3. Effective Adlayer Thickness

As seen in Equation (3), k^0_{app} is a function of the thickness of the adlayer. However, the actual value of *d* may be modulated by a number of factors. For example, adlayer defects (pinholes and collapsed sites) can cause a drop in the apparent average thickness of the adlayer. Thus, we cannot eliminate an oscillation of the defect density in these adlayers as one explanation of the rate data. In this pathway, the packing density of the odd-numbered adlayers must be slightly higher than the even-numbered adlayers due. Although the physical reasons for such an alternation is unclear, the equivalent of this mechanism could arise from the terminal methyl group being oriented more normal to the surface, enabling a more crystalline packing arrangement when *n* is odd.

It is well known that there is an odd-even effect in the melting points and densities of alkanethiols [80, 81]. These oscillations are more pronounced for short chains (i.e., ≤ 10 carbons), and are currently attributed to molecular packing effects [82, 83]. Although the contact angle data would support a defect density-based mechanism, analysis of the IRRAS spectra in Figure 7 provides no evidence for such an oscillation of crystallinity, as evidenced by the constancy of the absorption band locations (the frequency of many bands in liquid alkanes is often shifted relative to solid phase alkanes [7, 50, 55, 57]). This result, combined with the values of β obtained from the rate data (see above), leads us to concluded that a defect density alternation, although a possibility, is an unlikely explanation of the rate data.

Although defects could decrease the thickness of the adlayers as assessed using heterogeneous electron transfer kinetics, experimental and modeling data has also revealed an alternation of the adlayer thickness. The agreement between the two sets of data shows that this effect almost certainly arises as a consequence of the terminal methyl group orientation alternation since the modeled thickness measurements used identical reference points for each chain. Moreover, although the thickness oscillation is small, it does occur in the right direction to account for the alternation of $k^0{}_{\mathrm{app}}$ (i.e., the odd-numbered adlayers are slightly thicker than expected, leading to a smaller value of $k^0{}_{\mathrm{app}}$). Thus, a contribution from the actual thickness of the adlayers to the odd-even effect in $k^0{}_{\mathrm{app}}$ can not be discounted.

4. Conclusions

We have shown that odd-even oscillations in the value of the apparent heterogeneous electron transfer rate constant of solution-based redox couples can be observed at short-chain alkanethiolate monolayers on gold. By correlation of structural models and experimental data, possible origins for this effect were discussed. Notably, there are several possible mechanisms that can account for this data. Moreover, experimental assessments of the structure and properties of these adlayers provide evidence that there are oscillations in the adlayer thickness and in the permanent dipole orientation of the terminal methyl group. These assessments led to several mechanistic pathways for an odd-even effect in $k^0{}_{\mathrm{app}}$ to be manifested, including, double layer effects, electron transfer mechanisms (i.e., structurally-induced differences in the coupling strength or quantum interference), adlayer thickness alternations, and defect density oscillations. It is also feasible that more than one of these mechanisms play roles in determining the overall system response.

5. Acknowledgments

This work was supported, in part, by Eastman Chemical and the Ames Laboratory-USDOE. Grant A. Edwards gratefully acknowledges a Conoco-Phillips graduate research fellowship. Adam Johan Bergren gratefully acknowledges a Proctor and Gamble fellowship. Special thanks to Professor Andrew C. Hillier for the use of the ellipsometer. The Ames Laboratory is operated by Iowa State University for the U.S. Department of Energy under Contract W-7405-ENG-82.

6. References

[1] A. Ulman, An Introduction to Ultrathin Organic Films: From Langmuir-Blodgett to Self-Assembly, Academic Press, San Diego, 1991.

[2] H. O. Finklea, "Electrochemistry of Organized Monolayers of Thiols and Related Molecules on Electrodes" in Electroanalytical Chemistry: A Series of Advances, A. J. Bard and I. Rubinstein, eds., Marcel Dekker, Inc., New York, 1996.

[3] C.-J. Zhong and M. D. Porter, Anal. Chem. 67 (1995) 709A.

[4] H. O. Finklea, "Electroanalytical Methods: Self-Assembled Monolayers on Electrodes" in Encyclopedia of Analytical Chemistry, R. A. Meyers, ed. Vol. 11, John Wiley & Sons, Ltd, Chichester, 2000, p. 10090.

[5] C. A. Widrig, C. Chung, and M. D. Porter, J. Electroanal. Chem. 310 (1991) 335.

[6] J. C. Love, L. A. Estroff, J. K. Kriebel, R. G. Nuzzo, and G. M. Whitesides, Chem. Rev. 105 (2005) 1103.

[7] M. D. Porter, T. B. Bright, D. L. Allara, and C. E. D. Chidsey, J. Am. Chem. Soc. 109 (1987) 3559.

[8] A. Ulman, Chem. Rev. 96 (1996) 1533.

[9] C. E. D. Chidsey and D. N. Loiacono, Langmuir 6 (1990) 682.

[10] H. I. Kim and J. E. Houston, J. Am. Chem. Soc. 122 (2000) 12045.

[11] I. Wenzl, C. M. Yam, D. Barriet, and T. R. Lee, Langmuir 19 (2003) 10217.

[12] J. J. Sumner and S. E. Creager, J. Am. Chem. Soc. 122 (2000) 11914.

[13] Y.-T. Long, H.-T. Rong, M. Buck, and M. Grunze, J. Electroanal. Chem. 524-525 (2002) 62.

[14] H.-T. Rong, S. Frey, Y.-J. Yang, M. Zharnikov, M. Buck, M. Wuhn, C. Woll, and G. Helmchen, Langmuir 17 (2001) 1582.

[15] B. S. Day and J. R. Morris, J. Phys. Chem. B 107 (2003) 7120.

[16] J. F. Smalley, S. W. Feldberg, C. E. D. Chidsey, M. R. Linford, M. D. Newton, and Y.-P. Liu, J. Phys. Chem. 99 (1995) 13141.

[17] S.-S. Wong, H. Takano, and M. D. Porter, Anal. Chem. 70 (1998) 5209.

[18] P. E. Laibinis, G. M. Whitesides, D. L. Allara, Y.-T. Tao, A. N. Parikh, and R. G. Nuzzo, J. Am. Chem. Soc. 113 (1991) 7152.

[19] M. M. Walczak, C. Chung, S. M. Stole, C. A. Widrig, and M. D. Porter, J. Am. Chem. Soc. 113 (1991) 2370.

[20] M. A. Bryant and J. E. Pemberton, J. Am. Chem. Soc. 113 (1991) 8284.

[21] P. T. Radford and S. E. Creager, Anal. Chim. Acta 449 (2001) 199.

[22] P. T. Radford, M. French, and S. E. Creager, Anal. Chem. 71 (1999) 5101.

[23] A. J. Bergren and M. D. Porter, J. Electroanal. Chem. 585 (2005) 172.

[24] A. J. Bergren and M. D. Porter, J. Electroanal. Chem. Submitted (2005).

[25] C. Miller, P. Cuendet, and M. Gratzel, J. Phys. Chem. 95 (1991) 877.

[26] A. M. Becka and C. J. Miller, J. Phys. Chem. 96 (1992) 2657.

[27] K. Weber, L. Hockett, and S. Creager, J. Phys. Chem. B 101 (1997) 8286.

[28] P. T. Mikulski, L. A. Herman, and J. A. Harrison, Langmuir 21 (2005) 12197.

[29] F. Auer, G. Nelles, and B. Sellergren, Chem. Eur. J. 10 (2004) 3232.

[30] A. S. Lagutchev, J. E. Patterson, W. Huang, and D. D. Dlott, J. Phys. Chem. B 109 (2005) 5033.

[31] P. Srivastava, W. G. Chapman, and P. E. Laibinis, Langmuir 21 (2005) 12171.

[32] R. H. Schmehl, C. K. Ryu, C. M. Elliott, C. L. E. Headford, and S. Ferrere, Electron Transfer Biol. Solid State 226 (1990) 211.

[33] C.-P. Hsu, J. Electroanal. Chem. 438 (1997) 27.

[34] C.-P. Hsu and R. A. Marcus, J. Chem. Phys. 106 (1997) 584.

[35] E. Boubour and R. B. Lennox, Langmuir 16 (2000) 4333.

[36] S. E. Creager, L. A. Hockett, and G. K. Rowe, Langmuir 8 (1992) 854.

[37] C.-J. Zhong, R. C. Brush, J. Andregg, and M. D. Porter, Langmuir 15 (1999) 518.

[38] D. Dickertmann, J. W. Schultze, and K. J. Vetter, J. Electroanal. Chem. 55 (1974) 429.

[39] R. Woods, Chemisorption at Electrodes: Hydrogen and Oxygen on Noble Metals and their Alloys, Marcel Dekker, Inc., New York, 1976.

[40] G. A. Edwards, A. J. Bergren, and M. D. Porter, In Preparation (2006).

[41] S. M. Stole and M. D. Porter, Appl. Specrosc. 44 (1990) 1418.

[42] A. J. Bard and L. R. Faulkner, Electrochemical Methods: Fundamentals and Applications, John Wiley & Sons, Inc., New York, 2001.

[43] R. S. Nicholson, Anal. Chem. 37 (1965) 1351.

[44] P. Diao, D. Jang, X. Cui, D. Gu, R. Tong, and B. Zhong, J. Electroanal. Chem. 464 (1999) 61.

[45] A. L. Aljibury, R. G. Snyder, H. L. Strauss, and K. Raghavachari, J. Chem. Phys. 84 (1986) 6872.

[46] H. L. Casal, H. H. Mantsch, D. G. Cameron, and R. G. Snyder, J. Chem. Phys. 77 (1982) 2825.

[47] R. A. MacPhail, R. G. Snyder, and H. L. Strauss, J. Chem. Phys. 77 (1982) 1118.

[48] M. Maroncelli, H. L. Strauss, and R. G. Snyder, J. Chem. Phys. 82 (1985) 2811.

[49] D. H. Reneker, J. Mazur, J. P. Colson, and R. G. Snyder, J. Appl. Phys. 51 (1980) 5080.

[50] R. G. Snyder, J. Molecular Spectrosc. 7 (1961) 116.

[51] R. G. Snyder, J. Chem. Phys. 42 (1965) 1744.

[52] R. G. Snyder, S. L. Hsu, and S. Krimm, Spectrochim. Acta A: Mol. Biomol. Spectrosc. 34A (1978) 395.

[53] R. G. Snyder and J. R. Scherer, J. Chem. Phys. 71 (1979) 3221.

[54] R. G. Snyder, J. Chem. Phys. 71 (1979) 3229.

[55] R. G. Snyder, H. L. Strauss, and C. A. Elliger, J. Phys. Chem. 86 (1982) 5145.

[56] R. G. Snyder, A. L. Aljibury, H. L. Strauss, H. L. Casal, K. M. Gough, and W. F. Murphy, J. Chem. Phys. 81 (1984) 5352.

[57] R. G. Snyder, M. Maroncelli, H. L. Strauss, and V. M. Hallmark, J. Phys. Chem. 90 (1986) 5623.

[58] R. G. Snyder, Macromolecules 23 (1990) 2081.

[59] D. L. Allara and R. G. Nuzzo, Langmuir 1 (1985) 52.

[60] M. Moskovits, J. Phys. Chem. 77 (1982) 4408.

[61] R. G. Greenler, J. Chem. Phys. 44 (1966) 310.

[62] G. A. Edwards, A. J. Bergren, E. J. Cox, and M. D. Porter, In Preparation (2006).

[63] J. J. Sumner and S. E. Creager, J. Phys. Chem. B 105 (2001) 8739.

[64] R. A. Marcus, Electrochim. Acta 13 (1968) 995.

[65] C. J. Miller, "Heterogeneous Electron Transfer Kinetics at Metallic Electrodes" in Physical Electrochemistry: Principles, Methods, and Applications, I. Rubinstein, ed., Marcel Dekker, Inc., New York, 1995.

[66] M. D. Newton, Chem. Rev. 91 (1991) 767.

[67] K. Slowinski, H. K. Y. Fong, and M. Majda, J. Am. Chem. Soc. 121 (1999) 7257.

[68] W. Wang, T. Lee, and M. A. Reed, Phys. Rev. B 68 (2003) 035416.

[69] Y. Selzer, A. Salomon, and D. Cahen, J. Phys. Chem. B 106 (2002) 10432.

[70] Y. Selzer, A. Salomon, and D. Cahen, J. Am. Chem. Soc. 124 (2002) 2886.

[71] Y.-J. Liu and H.-Z. Yu, ChemPhysChem 9 (2002) 799.

[72] A. Salomon, D. Cahen, S. Lindsay, J. Tomfohr, V. B. Engelkes, and C. D. Frisbie, Adv. Mater. 15 (2003) 1881.

[73] D. K. Aswal, S. Lenfant, D. Guerin, J. V. Yakhmi, and D. Vuillaume, Anal. Chim. Acta In Press (2005).

[74] X. D. Cui, A. Primak, X. Zarate, J. Tomfohr, O. F. Sankey, A. L. Moore, T. A. Moore, D. Gust, L. A. Nagahara, and S. M. Lindsay, J. Phys. Chem. B 106 (2002) 8609.

[75] X. D. Cui, X. Zarate, J. Tomfohr, O. F. Sankey, A. Primak, A. L. Moore, D. Gust, G. Harris, and S. M. Lindsay, Nanotechnology 13 (2002) 5.

[76] A. J. Bergren and M. D. Porter, In Preparation (2005).

[77] H. O. Finklea, L. Liu, M. S. Ravenscroft, and S. Punturi, J. Phys. Chem. 100 (1996) 18852.

[78] K. Slowinski, R. V. Chamberlain, C. J. Miller, and M. Majda, J. Am. Chem. Soc. 119 (1997) 11910.

[79] J. Cheng and C. J. Miller, J. Phys. Chem. B 101 (1997) 1058.

[80] H. C. Helgeson, C. E. Owens, A. M. Knox, and L. Richard, Geochim. Cosmochim. Acta 62 (1998) 985.

[81] D. E. Teets, J. Am. Chem. Soc. 56 (1934) 1143.

[82] R. Boese, H.-C. Weiss, and D. Blaser, Angew. Chem. Int. Ed. 38 (1999) 988.

[83] V. R. Thalladi, R. Boese, and H.-C. Weiss, J. Am. Chem. Soc. 122 (2000) 1186.

CHAPTER 6. CONCLUSIONS AND PROSPECTS

1. General Conclusions

Electron transfer reactions are important tools and processes in analytical and physical chemistry. Chemically modified electrodes enable many fundamentally important and novel processes to be investigated. For example, designed interfaces allow the exploitation of unique reactivity patterns to improve the performance of electrochemical sensors; these gains in sensitivity are not possible with conventional electrodes. This dissertation has detailed the application of alkanethiolate monolayer modified gold electrodes to redox recycling current amplification. A systematic and detailed account of the electron transfer mechanism for redox recycling has been described in terms of the required rates of the involved species and the processes that contribute to background currents. Moreover, the physical origin of the selectivity exhibited by these electrodes for derivatized ferrocenes over ferrocyanide was investigated. The resulting insights provide a means to establish guidelines for optimizing performance and will prove critical to the ability to evaluate potential analyte/sacrificial molecule pairs with respect to amplification efficiency and electrode selectivity.

This dissertation also presented evidence for the odd-even alternation of the heterogeneous electron transfer rate of solution-based redox couples with respect to the number of methylene units in the alkyl chain of an insulating barrier molecule (i.e., an alkanethiolate on gold). These studies established many different odd-even effects in the structure and properties of alkanethiolate monolayers on gold. Although some of these have appeared in previous literature [1-7], this work presents the first evidence of such an effect on heterogeneous electron transfer using solution-based redox couples and in thickness [8].

2. Prospects and Outlook

Redox recycling has extensive potential applications in electroanalytical sensor design. Moreover, this complex system integrates many fundamentally important processes that can serve to extend our knowledge of the relationship between interfacial designs and electron transfer routes. There are, however, several areas that need further work for redox recycling to be more universally applicable, and also many details of self-assembled monolayer preparation that remain to be well understood.

The studies of redox recycling in this dissertation comprise a method for detecting derivatized ferrocenes with enhanced sensitivity using voltammetry. Along with guided interfacial design refinements, the application of other electrochemical detection modes (e.g., pulsed waveforms with specialized sampling intervals) may lead to further enhancements in sensitivity. Although this system is well suited for fundamental studies of sensor design, in real-world analysis the detection of ferrocenes has only limited applicability. Thus, the development of ferrocene-containing labels would extend the range and scope of this powerful detection method. For example, the preparation of ferrocene-containing micro- and nanoparticles and the direct covalent bonding of ferrocenes to the target analyte have been pursued by many different research groups [9-13].

Self-assembled monolayers continue to be applied for many different purposes. However, there are several issues regarding the preparation of these adlayers that remain elusive. In particular, the reproducible preparation of monolayers usually requires each researcher to develop and refine procedures based on actual performance tests for the intended use. This limitation makes comparisons between laboratories, and even in the same group, difficult or impossible, especially where fine-structure or detailed performance diagnostics are concerned. For example, the nucleation and growth conditions depend on the delivery of thiol molecules to the gold surface; assembly-vessel geometry, thiol concentration, and immersion time therefore affect the impingement rate (and thus, the growth conditions) [14].

The characteristics of the underlying gold surface also have an impact on the performance of the adlayer. In fact, when using heterogeneous electron transfer as a metric for the insulating properties of the thiolate monolayer, a counter-intuitive relationship is found. That is, monolayers prepared on rough surfaces perform better as barriers to electron transfer than smooth surfaces [15]. The underlying cause of this phenomenon is probably due to the way in which the adlayer grows: incompatible domain registries result when growth initiates on the extended terraces provided by a smooth surface, leading to relatively large defect structures where the different nucleation realms meet. The smaller defects formed at a rough surface, while found in greater number, do not allow the redox couple to obtain as close a proximity to the electrode surface, resulting in larger current flow across the barrier formed at the smooth electrode.

These issues collectively point to several possible causes for the difficulties encountered in preparing monolayers with identical properties. Although a limitation when exacting measurements are required, this variability, if understood, could provide for greater versatility in the functions that can be achieved. Nevertheless, the underlying causes of the variations encountered when using monolayers that are prepared under ostensibly identical conditions need to be disentangled before a generalized guide can be developed. This work is ongoing in our own research group [16], and also in others [17].

3. References

[1] F. Auer, G. Nelles, and B. Sellergren, Chem. Eur. J. 10 (2004) 3232.

[2] B. S. Day and J. R. Morris, J. Phys. Chem. B 107 (2003) 7120.

[3] P. E. Laibinis, G. M. Whitesides, D. L. Allara, Y.-T. Tao, A. N. Parikh, and R. G. Nuzzo, J. Am. Chem. Soc. 113 (1991) 7152.

[4] Y.-T. Long, H.-T. Rong, M. Buck, and M. Grunze, J. Electroanal. Chem. 524-525 (2002) 62.

[5] J. F. Smalley, S. W. Feldberg, C. E. D. Chidsey, M. R. Linford, M. D. Newton, and Y.-P. Liu, J. Phys. Chem. 99 (1995) 13141.

[6] J. J. Sumner and S. E. Creager, J. Am. Chem. Soc. 122 (2000) 11914.

[7] M. M. Walczak, C. Chung, S. M. Stole, C. A. Widrig, and M. D. Porter, J. Am. Chem. Soc. 113 (1991) 2370.

[8] G. A. Edwards, A. J. Bergren, E. J. Cox, and M. D. Porter, (2006).

[9] J. Chen, C. Xu, and K. Aoki, J. Electroanal. Chem. 546 (2003) 79.

[10] H. Eckert and M. Koller, J. Liq. Chromatogr. 13 (1990) 3399.

[11] K. Shimada, E. Haniuda, T. Oe, and T. Nambara, J. Liq. Chromatogr. 10 (1987) 3161.

[12] K. Shimada, T. Oe, and T. Nambara, J. Chromatogr. 419 (1987) 17.

[13] K. Shimada, Y. Kawai, T. Oe, and T. Nambara, J. Liq. Chromatogr. 12 (1989) 359.

[14] G. A. Edwards, A. J. Bergren, E. J. Cox, and M. D. Porter, In Preparation (2006).

[15] J.-B. D. Green, C. A. McDermott, M. T. McDermott, C.-J. Zhong, A. J. Bergren, and M. D. Porter, Manuscript in Preparation (2006).

[16] A. J. Bergren, G. A. Edwards, and E. J. Cox, In Preparation (2006).

[17] F. Ma and R. B. Lennox, Langmuir 16 (2000) 6188.